# Lectures on computational fluid dynamics

Applications to human thermodynamics

Prof. Dr.-Ing. habil. Nikolai Kornev; Prof. Dr.-Ing. habil. Irina Cherunova
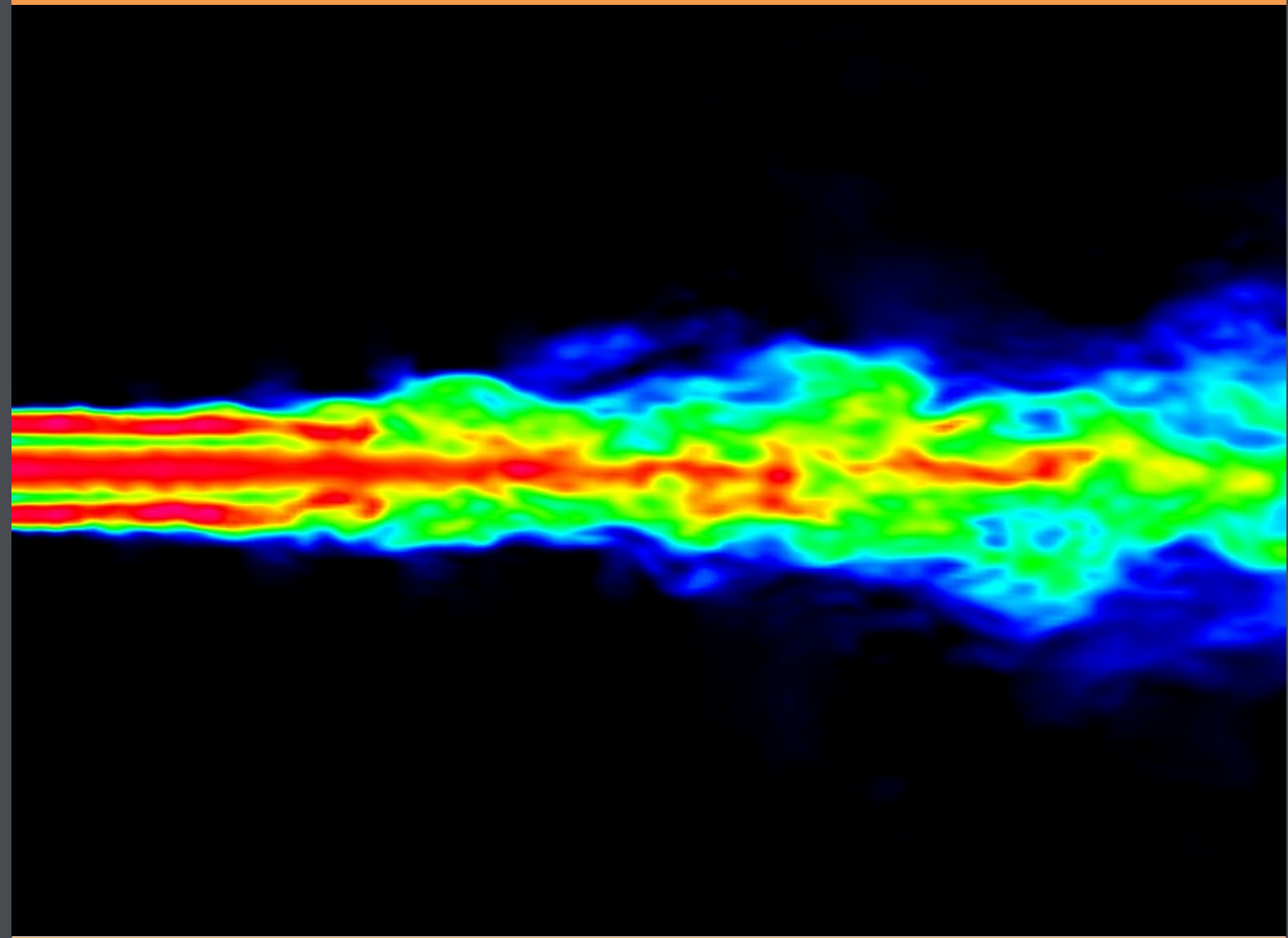
Prof. Dr.-Ing. habil. Nikolai Kornev & Prof. Dr.-Ing. habil. Irina Cherunova

Lectures on computational fluid dynamics

Applications to human thermodynamics

Contents

List of Tables

List of Figures

Preface

The present book is used for lecture courses Computational heat and mass transfer, Mathematical models of turbulence and Design of special cloth given by the authors at the University of Rostock, Germany and Don State Technical University, Russia. Each of lecture courses contains about 14 lectures. The lecture course Compuational heat and mass transfer was written proceeding from the idea to present the complex material as easy as possible. We considered derivation of numerical methods, particularly of the finite volume method, in details up to final expressions which can be programmed. Turbulence is a big and a very complicated topic which is difficult to cover within 14 lectures. We selected the material combining the main physical concepts of the turbulence with basic mathematical models necessary to solve practical engineering problems. The course Design of special cloth uses the material of two parts of this book partially. The material for the third part was gathered from research projects done by the authors of this book within some industrial projects and research works supported by different foundations. We express our gratitude to Andreas Gross, Gunnar Jacobi and Stefan Knochenhauer who carried out CFD calculations for the third part of this book.

Part I

Introduction into computational methods for solution of transport equations

Chapter 1

Main equations of the Computational Heat and Mass Transfer

1.1 Fluid mechanics equations

1.1.1 Continuity equation

We consider the case of uniform density distribution $\rho = const$. The continuity equation has the following physical meaning: The amount of liquid flowing into the volume U with the surface S is equal to the amount of liquid flowing out. Mathematically it can be expressed in form:

$$\int_S \vec{u}\vec{n}\, ds = 0 \qquad (1.1)$$

Expressing the scalar product $\vec{u}\vec{n}$ through components

$$\int_S \left(u_x \cos(nx) + u_y \cos(ny) + u_z \cos(nz) \right) ds = 0.$$

and using the Gauss theorem we get

$$\int_U \left(\frac{\partial u_x}{\partial x} + \frac{\partial u_y}{\partial y} + \frac{\partial u_z}{\partial z} \right) dU = 0$$

Since the integration volume U is arbitrary, the integral is zero only if

$$\frac{\partial u_x}{\partial x} + \frac{\partial u_y}{\partial y} + \frac{\partial u_z}{\partial z} = 0 \qquad (1.2)$$

In the tensor form the continuity equation reads:

$$\frac{\partial u_i}{\partial x_i} = 0 \qquad (1.3)$$

1.1.2 Classification of forces acting in a fluid

The inner forces acting in a fluid are subdivided into the body forces and surface forces (Fig. 1.1).
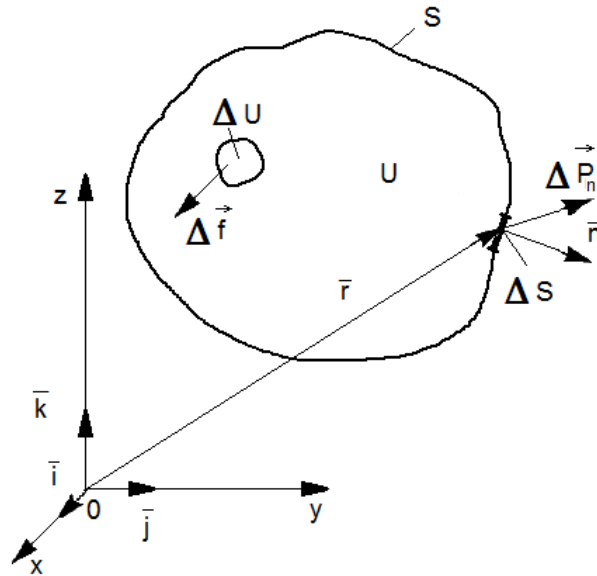
Figure 1.1: Body and surface forces acting on the liquid element.

1.1.2.1 Body forces

Let $\Delta\vec{f}$ be a total body force acting on the volume ΔU. Let us introduce the strength of the body force as limit of the ratio of the force to the volume:

$$\vec{F} = \lim_{\Delta U \to 0} \frac{\Delta\vec{f}}{\rho\Delta U} \tag{1.4}$$

which has the unit $\frac{kg\,m}{s^2} \frac{m^3}{kg} \frac{1}{m^3} = m\,s^{-2}$. Typical body forces are gravitational, electrostatic or electromagnetic forces. For instance, we have the following relations for the gravitational forces:

$$\Delta\vec{f} = \rho g \Delta U \vec{k} \tag{1.5}$$

where $\Delta\vec{f}$ is the gravitational force acting on a particle with volume ΔU. The strength of the gravitational force is equal to the gravitational acceleration:

$$\vec{F} = \lim_{\Delta U \to 0} (-\frac{\rho g \Delta U \vec{k}}{\rho \Delta U}) = -g\vec{k} \tag{1.6}$$

The body forces are acting at each point of fluid in the whole domain.

1.1.2.2 Surface forces

The surface forces are acting at each point at the boundary of the fluid element. Usually they are shear and normal stresses. The strength of surface forces is determined as

$$\vec{p}_n = \lim_{\Delta S \to 0} \frac{\Delta \vec{P}_n}{\Delta S} \tag{1.7}$$

with the unit $\frac{kg\,m}{s^2}\frac{1}{m^2} = \frac{kg}{m\,s^2}$. A substantial feature of the surface force is the dependence of $\vec{p}_n$ on the orientation of the surface ΔS.

The surface forces are very important because they act on the body from the side of liquid and determine the forces $\vec{R}$ arising on bodies moving in the fluid:

$$\vec{R} = \int_S \vec{p}_n dS$$

$$\vec{M} = \int_S (\vec{r} \times \vec{p}_n) dS \tag{1.8}$$

1.1.2.3 Properties of surface forces

Let us consider a liquid element in form of the tetrahedron (Fig. 1.2). Its motion is described by the 2nd law of Newton:

$$\rho \Delta U \frac{d\vec{u}}{dt} = \rho \Delta U \vec{F} + \vec{p}_n \Delta S - \vec{p}_x \Delta S_x - \vec{p}_y \Delta S_y - \vec{p}_z \Delta S_z \tag{1.9}$$
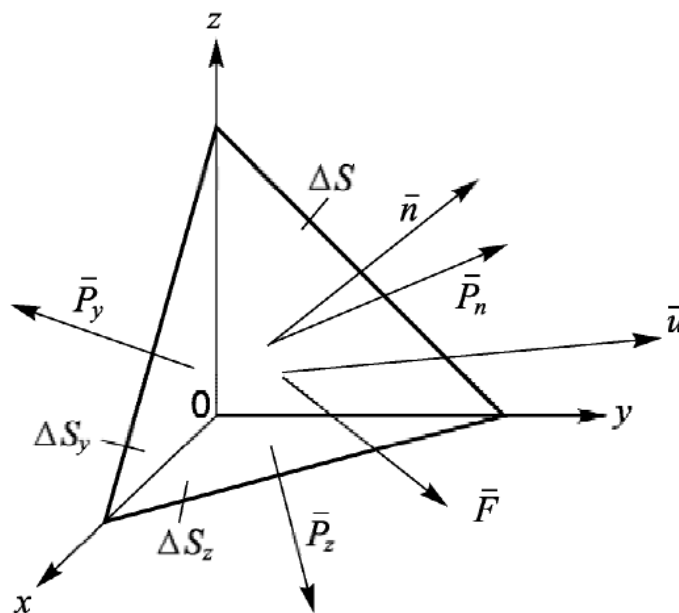
Figure 1.2: Forces acting on the liquid element.

Dividing r.h.s and l.h.s. by the surface of inclined face ΔS results in:

$$\rho \frac{\Delta U}{\Delta S} \left(\frac{d\vec{u}}{dt} - \vec{F} \right) = \vec{p}_n - \vec{p}_x \frac{\Delta S_x}{\Delta S} - \vec{p}_y \frac{\Delta S_y}{\Delta S} - \vec{p}_z \frac{\Delta S_z}{\Delta S} \qquad (1.10)$$

Let us find the limit of (1.10) at $\Delta S \to 0$:

$$\lim_{\Delta S \to 0} \frac{\Delta U}{\Delta S} = 0, \; \lim_{\Delta S \to 0} \frac{\Delta S_x}{\Delta S} = \cos(nx), \qquad (1.11)$$

$$\lim_{\Delta S \to 0} \frac{\Delta S_y}{\Delta S} = \cos(ny), \; \lim_{\Delta S \to 0} \frac{\Delta S_z}{\Delta S} = \cos(nz) \qquad (1.12)$$

Substitution of (1.11) and (1.12) into (1.10) results in the following relation between $\vec{p}_n$ and $\vec{p}_x$, $\vec{p}_y$, $\vec{p}_z$:

$$\vec{p}_n = \vec{p}_x \cos(nx) + \vec{p}_y \cos(ny) + \vec{p}_z \cos(nz) \qquad (1.13)$$

Let us write the surface forces through components:

$$\vec{p}_x = \vec{i}\, p_{xx} + \vec{j}\, \tau_{xy} + \vec{k}\, \tau_{xz}$$

$$\vec{p}_y = \vec{i}\, \tau_{yx} + \vec{j}\, p_{yy} + \vec{k}\, \tau_{yz}$$

$$\vec{p}_z = \vec{i}\, \tau_{zx} + \vec{j}\, \tau_{zy} + \vec{k}\, p_{zz}$$

Here τ_{ij} are shear stress (for instance $\tau_{12} = \tau_{xy}$), whereas p_{ii} are normal stress (for instance $p_{11} = p_{xx}$). From moment equations (see Fig. 1.3) one can obtain the symmetry condition for shear stresses: $\tau_{zy}a - \tau_{yz}a = 0 \Rightarrow \tau_{zy} = \tau_{yz}$ and generally:

$$\tau_{ij} = \tau_{ji} \tag{1.14}$$
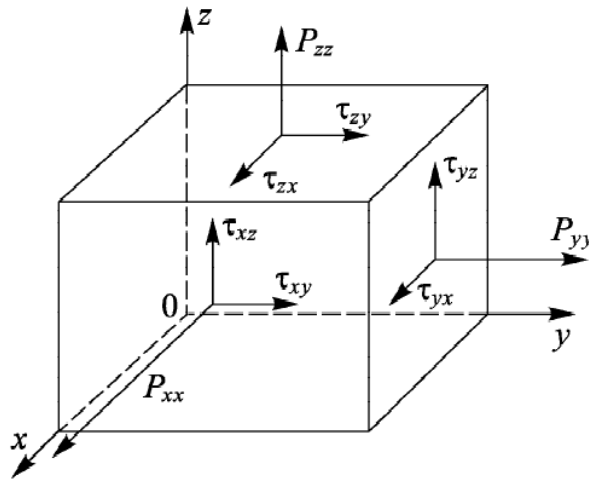
Figure 1.3: Stresses acting on the liquid cube with sizes a.

The stress matrix is symmetric and contains 6 unknown elements:

$$\begin{pmatrix} p_{xx} & \tau_{xy} & \tau_{xz} \\ \tau_{xy} & p_{yy} & \tau_{yz} \\ \tau_{xz} & \tau_{yz} & p_{zz} \end{pmatrix} \tag{1.15}$$

1.1.3   Navier Stokes Equations

Applying the Newton second law to the small fluid element dU with the surface dS and using the body and surface forces we get:

$$\int_U \frac{d\vec{u}}{dt} \rho \, dU = \int_U \vec{F} \rho \, dU + \int_S \vec{p}_n \, dS \tag{1.16}$$

The property of the surface force can be rewritten with the Gauss theorem in the following form:

$$\int_S \vec{p}_n \, dS = \int_S \left(\vec{p}_x \cos(nx) + \vec{p}_y \cos(ny) + \vec{p}_z \cos(nz) \right) dS$$

$$= \int_U \left(\frac{\partial \vec{p}_x}{\partial x} + \frac{\partial \vec{p}_y}{\partial y} + \frac{\partial \vec{p}_z}{\partial z} \right) dU$$

The second law (1.16) takes the form:

$$\int\limits_{U} \frac{d\vec{u}}{dt} \rho dU = \int\limits_{U} \vec{F} \rho dU + \int\limits_{U} \left(\frac{\partial \vec{p}_x}{\partial x} + \frac{\partial \vec{p}_y}{\partial y} + \frac{\partial \vec{p}_z}{\partial z} \right) dU$$

$$\int\limits_{U} \left[\frac{d\vec{u}}{dt} \rho - \rho\vec{F} - \left(\frac{\partial \vec{p}_x}{\partial x} + \frac{\partial \vec{p}_y}{\partial y} + \frac{\partial \vec{p}_z}{\partial z} \right) \right] dU = 0$$

Since the volume dU is arbitrary, the l.h.s. in the last formulae is zero only if:

$$\frac{d\vec{u}}{dt} = \vec{F} + \frac{1}{\rho} \left(\frac{\partial \vec{p}_x}{\partial x} + \frac{\partial \vec{p}_y}{\partial y} + \frac{\partial \vec{p}_z}{\partial z} \right) \tag{1.17}$$

The stresses in (1.17) are not known. They can be found from the generalized Newton hypothesis

$$\begin{pmatrix} p_{xx} & \tau_{xy} & \tau_{xz} \\ \tau_{xy} & p_{yy} & \tau_{yz} \\ \tau_{xz} & \tau_{yz} & p_{zz} \end{pmatrix} = - \begin{pmatrix} p & 0 & 0 \\ 0 & p & 0 \\ 0 & 0 & p \end{pmatrix} + 2\mu S_{ij} \tag{1.18}$$

where p is the pressure,

$$S_{11} = S_{xx} = \frac{\partial u_x}{\partial x}; \; S_{12} = S_{xy} = \frac{1}{2}\left(\frac{\partial u_x}{\partial y} + \frac{\partial u_y}{\partial x} \right); \; S_{13} = S_{xz} = \frac{1}{2}\left(\frac{\partial u_x}{\partial z} + \frac{\partial u_z}{\partial x} \right)$$

$$S_{21} = S_{12}, \quad S_{22} = S_{yy} = \frac{\partial u_y}{\partial y}, \quad S_{23} = S_{yz} = \frac{1}{2}\left(\frac{\partial u_y}{\partial z} + \frac{\partial u_z}{\partial y} \right)$$

$$S_{31} = S_{13}, \quad S_{32} = S_{23}, \quad S_{33} = S_{zz} = \frac{\partial u_z}{\partial z}$$

The liquids obeying (1.18) are referred to as the Newtonian liquids.

The normal stresses can be expressed through the pressure p:

$$p_{xx} = -p + 2\mu\frac{\partial u_x}{\partial x}, \quad p_{yy} = -p + 2\mu\frac{\partial u_y}{\partial y}, \quad p_{zz} = -p + 2\mu\frac{\partial u_z}{\partial z}$$

The sum of three normal stresses doesn't depend on the choice of the coordinate system and is equal to the pressure taken with sign minus:

$$\frac{p_{xx} + p_{yy} + p_{zz}}{3} = -p \tag{1.19}$$

The last expression is the definition of the pressure in the viscous flow: The pressure is the sum of three normal stresses taken with the sign minus. Substitution of the Newton hypothesis (1.18) into (1.17) gives (using the first equation as a sample):

$$
\rho \frac{du_x}{dt} = \rho F_x + \frac{\partial}{\partial x}\left(-p + 2\mu \frac{\partial u_x}{\partial x}\right) + \frac{\partial}{\partial y}\left(\mu\left(\frac{\partial u_y}{\partial x} + \frac{\partial u_x}{\partial y}\right)\right)
$$

$$
+ \frac{\partial}{\partial z}\left(\mu\left(\frac{\partial u_x}{\partial z} + \frac{\partial u_z}{\partial x}\right)\right) =
$$

$$
= \rho F_x - \frac{\partial p}{\partial x} + \mu\left(\frac{\partial^2 u_x}{\partial x^2} + \frac{\partial^2 u_x}{\partial y^2} + \frac{\partial^2 u_x}{\partial z^2}\right) +
$$

$$
+ \mu \frac{\partial}{\partial x}\left(\frac{\partial u_x}{\partial x} + \frac{\partial u_y}{\partial y} + \frac{\partial u_z}{\partial z}\right)
$$

The last term in the last formula is zero because of the continuity equation. Doing similar transformation with resting two equations in y and z directions, one can obtain the following equation, referred to as the Navier-Stokes equation:

$$
\frac{d\vec{u}}{dt} = \vec{F} - \frac{1}{\rho}\nabla p + \nu\Delta\vec{u} \tag{1.20}
$$

The full or material substantial derivative of the velocity vector $\frac{d\vec{u}}{dt}$ is the acceleration of the fluid particle. It consists of two parts: local acceleration and convective acceleration:

$$\frac{d\vec{u}}{dt} = \underbrace{\frac{\partial\vec{u}}{\partial t}}_{\text{local acceleration}} + \underbrace{u_x\frac{\partial\vec{u}}{\partial x} + u_y\frac{\partial\vec{u}}{\partial y} + u_z\frac{\partial\vec{u}}{\partial z}}_{\text{convective acceleration}}$$

The local acceleration is due to the change of the velocity in time. The convective acceleration is due to particle motion in a nonuniform velocity field. The Navier-Stokes Equation in tensor form is:

$$\frac{\partial u_i}{\partial t} + u_j\frac{\partial u_i}{\partial x_j} = F_i - \frac{1}{\rho}\frac{\partial p}{\partial x_i} + v\frac{\partial}{\partial x_j}\left(\frac{\partial}{\partial x_j}u_i\right) \qquad (1.21)$$

Using the continuity equation (1.3) the convective term can be written in the conservative form:

$$u_j\frac{\partial u_i}{\partial x_j} = \frac{\partial}{\partial x_j}\left(u_iu_j\right) \qquad (1.22)$$

Finally, the Navier Stokes in the tensor form is:

$$\frac{\partial u_i}{\partial t} + \frac{\partial}{\partial x_j}(u_iu_j) = F_i - \frac{1}{\rho}\frac{\partial p}{\partial x_i} + v\frac{\partial}{\partial x_j}\left(\frac{\partial}{\partial x_j}u_i\right) \qquad (1.23)$$

The Navier Stokes equation together with the continuity equation (1.3) is the closed system of partial differential equations. Four unknowns velocity components u_x, u_y, u_z and pressure p are found from four equations. The equation due to presence of the term $\frac{\partial}{\partial x_j}(u_iu_j)$ is nonlinear.

The boundary conditions are enforced for velocity components and pressure at the boundary of the computational domain. The no slip condition $u_x = u_y = u_z = 0$ is enforced at the solid body boundary. The boundary condition for the pressure at the body surface can directly be derived from the Navier Stokes equation. For instance, if $y = 0$ corresponds to the wall, the Navier Stokes Equation takes the form at the boundary:

$$\frac{\partial p}{\partial x} = \rho F_x + \mu\frac{\partial^2 u_x}{\partial y^2}$$

$$\frac{\partial p}{\partial y} = \rho F_y + \mu\frac{\partial^2 u_y}{\partial y^2}$$

$$\frac{\partial p}{\partial z} = \rho F_z + \mu\frac{\partial^2 u_z}{\partial y^2}$$

Very often the last term in the last formulae is neglected because second spatial derivatives of the velocity are not known at the wall boundary.

Till now, the existence of the solution of Navier Stokes has been not proven by mathematicians. Also, it is not clear whether the solution is smooth or allows singularity. The Clay Mathematics Institute has called the Navier–Stokes existence and smoothness problems one of the seven most important open problems in mathematics and has offered one million dollar prize for its solution.

1.2   Heat conduction equation

Let $\mathbf{q}(\mathbf{x}, t)$ be the heat flux vector, U is the volume of fluid or solid body, S is its surface and $\mathbf{n}$ is the unit normal vector to S. Flux of the inner energy into the volume U at any point $\mathbf{x} \in \mathbf{U}$ is

$$-\mathbf{q}(\mathbf{x}, t) \cdot \mathbf{n}(\mathbf{x}) \tag{1.24}$$

Integrating (1.24) over the surface S we obtain:

$$-\int_S \mathbf{q} \cdot \mathbf{n} dS \tag{1.25}$$

and using the Gauss theorem

$$\int_S \mathbf{q}(\mathbf{x}, t) \cdot \mathbf{n}(\mathbf{x}) dS = \int_U \nabla \cdot \mathbf{q}(\mathbf{x}, t) dU \tag{1.26}$$

From the other side the change of the inner energy in the volume U is equal to $\int_U \rho c_p \frac{\partial}{\partial t} T(\mathbf{x}, t) dU$, where T is the temperature, c_p is the specific heat capacity and ρ is the density. Equating this change to (1.26) we get:

$$\int_U \rho c_p \frac{\partial}{\partial t} T(\mathbf{x}, t) dU = -\int_U \nabla \cdot \mathbf{q}(\mathbf{x}, t) dU + \int_U f(\mathbf{x}, t) dU \tag{1.27}$$

Here f is the heat sources within the volume U.

Fourier has proposed the following relation between the local heat flux and temperature difference, known as the Fourier law:

$$\mathbf{q}(\mathbf{x}, t) = -\lambda \nabla T(\mathbf{x}, t) \tag{1.28}$$

where λ is the heat conduction coefficient.

Substitution of the Fourier law (1.28) into the inner energy balance equation (1.27) results in

$$\int_\omega \left(\rho c_p \frac{\partial}{\partial t} T(\mathbf{x}, t) - \nabla \cdot (\lambda \nabla T(\mathbf{x}, t)) \right) dU = \int_U f(\mathbf{x}, t) dU \tag{1.29}$$

Since the volume U is arbitrary, (1.29) is reduced to

$$\rho c_p \frac{\partial}{\partial t} T(\mathrm{x}, t) - \nabla \cdot (\lambda \nabla T(\mathrm{x}, t)) = f(\mathbf{x}, t) \qquad (1.30)$$

The equation (1.30) is the heat conduction equation. The heat conduction coefficient for anisotropic materials is the tensor

$$\lambda = \begin{pmatrix} \lambda_{11} & \lambda_{12} & \lambda_{13} \\ \lambda_{12} & \lambda_{22} & \lambda_{23} \\ \lambda_{13} & \lambda_{23} & \lambda_{33} \end{pmatrix} \qquad (1.31)$$

The following boundary conditions are applied for the heat conduction equation (1.30):

- Neumann condition:

$$\nabla T(\mathrm{x}, t) \cdot \mathbf{n}(\mathbf{x}) = F_1(\mathbf{x}, t), \quad \mathbf{x} \in S \qquad (1.32)$$

- Dirichlet condition:

$$T(\mathbf{x}, t) = F_2(\mathrm{x}, t), \quad \mathbf{x} \in S \qquad (1.33)$$

Chapter 2
Finite difference method

2.1   One dimensional case

Let us consider the finite difference method for the one dimensional case. Let $\varphi(x)$ is the function defined in the range $[0, a]$ along the x axis. The section $[0, a]$ is subdivided in a set of points x_i. For the homogeneous distribution $x_i = (i - 1)\Delta; i = 1, N$, $\Delta = a/(N - 1)$ (see Fig. 2.1).
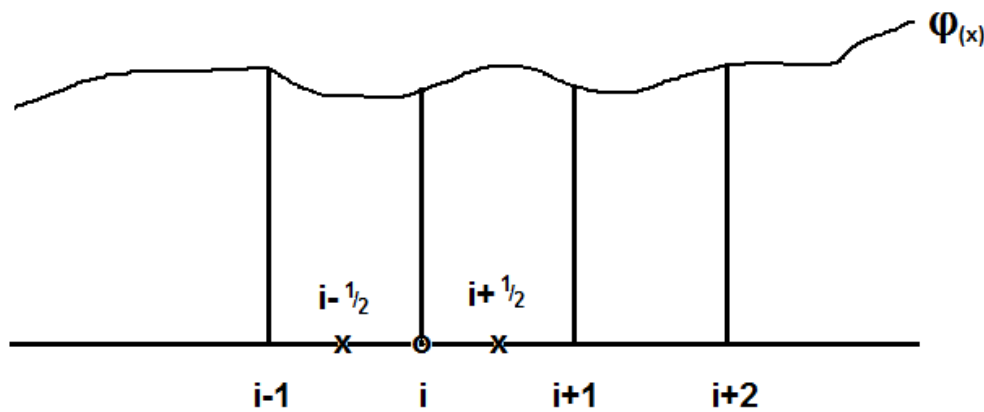
Figure 2.1: One dimensional case.

Let us approximate the derivative $\frac{\partial \varphi}{\partial x}$ [1]. The Taylor series of the function φ at points x_{i-1} and x_{i+1} are:

$$\varphi_{i-1} = \varphi_i - \Delta x \left(\frac{\partial \varphi}{\partial x}\right)_i + \frac{1}{2}\Delta x^2 \left(\frac{\partial^2 \varphi}{\partial x^2}\right)_i - \ldots \qquad (2.1)$$

$$\varphi_{i+1} = \varphi_i + \Delta x \left(\frac{\partial \varphi}{\partial x}\right)_i + \frac{1}{2}\Delta x^2 \left(\frac{\partial^2 \varphi}{\partial x^2}\right)_i + \ldots \qquad (2.2)$$

Expressing the derivative $\left(\frac{\partial \varphi}{\partial x}\right)_i$ from (2.1) we get the Backward Difference Scheme (BDS):

$$\left(\frac{\partial \varphi}{\partial x}\right)_i = \frac{1}{\Delta x}\left(\varphi_i - \varphi_{i-1}\right) + O\left(\Delta x\right) \qquad (2.3)$$

Expressing the derivative $\left(\frac{\partial \varphi}{\partial x}\right)_i$ from (2.2) we get the Forward Difference Scheme (FDS):

---

[1] We use the partial derivative although the function depends only on one variable

$$\left(\frac{\partial \varphi}{\partial x}\right)_i = \frac{1}{\Delta x}\left(\varphi_{i+1} - \varphi_i\right) + O\left(\Delta x\right) \qquad (2.4)$$

Accuracy of both schemes is of the first order. Subtracting (2.1) from (2.2) we get the Central Difference Scheme (CDS)

$$\left(\frac{\partial \varphi}{\partial x}\right)_i = \frac{1}{2\Delta x}\left(\varphi_{i+1} - \varphi_{i-1}\right) + O\left(\Delta x^2\right) \qquad (2.5)$$

which is of the second order accuracy.

For the approximation of derivatives $u_i \left(\frac{\partial \varphi}{\partial x}\right)_i$ where u_i is the flow velocity one uses the Upwind Difference Scheme (UDS):

$$\left(\frac{\partial \varphi}{\partial x}\right)_i = \begin{cases} \text{BDS}, & \text{if } u > 0 \\ \text{FDS}, & \text{if } u < 0 \end{cases} \qquad (2.6)$$

The accuracy of BDS, FDS and CDS can be improved using the polynomial representation of the function $\varphi(x)$. For instance, consider the approximation

$$\varphi(x) = ax^2 + bx + c$$

within the section $[x_{i-1}, x_{i+1}]$.

Without loss of generality we assume $x_{i-1} = 0$. The coefficient c can be obtained from the condition:

$$\varphi(0) = \varphi_{i-1} = c$$

Other two coefficients a and b are determined from the conditions:

$$\varphi_i = a\Delta x^2 + b\Delta x + \varphi_{i-1}$$

$$\varphi_{i+1} = a4\Delta x^2 + b2\Delta x + \varphi_{i-1}$$

$$a = \frac{\varphi_{i+1} - 2\varphi_i + \varphi_{i-1}}{2\Delta x^2}$$

$$b = \frac{-\varphi_{i+1} + 4\varphi_i - 3\varphi_{i-1}}{2\Delta x}$$

The first derivative using CDS is then

$$\left(\frac{\partial \varphi}{\partial x}\right)_i = 2a\Delta + b = \frac{\varphi_{i+1} - \varphi_{i-1}}{2\Delta x}$$

the second derivative:

$$\left(\frac{\partial^2 \varphi}{\partial x^2}\right)_i = 2a = \frac{\varphi_{i+1} - 2\varphi_i + \varphi_{i-1}}{\Delta x^2}$$

If the polynomial of the 3rd order $\varphi(x) = ax^3 + bx^2 + cx + d$ is applied, we get:

$$\left(\frac{\partial \varphi}{\partial x}\right)_i = \frac{1}{6\Delta x}\left(2\varphi_{i+1} + 3\varphi_i - 6\varphi_{i-1} + \varphi_{i-2}\right) + O\left(\Delta x^3\right) \qquad (2.7)$$

for the Backward Difference Scheme,

$$\left(\frac{\partial \varphi}{\partial x}\right)_i = \frac{1}{6\Delta x}\left(-\varphi_{i+2} + 6\varphi_{i+1} - 3\varphi_i - 2\varphi_{i-1}\right) + O\left(\Delta x^3\right) \qquad (2.8)$$

for the Forward Difference Scheme and

$$\left(\frac{\partial \varphi}{\partial x}\right)_i = \frac{1}{12\Delta x}\left(-\varphi_{i+2} + 8\varphi_{i+1} - 8\varphi_{i-1} + \varphi_{i-2}\right) + O\left(\Delta x^4\right) \qquad (2.9)$$

for the Central Difference Scheme. As seen the accuracy order is sufficiently improved by consideration of more adjacent points.
The second derivatives are:

$$\left(\frac{\partial^2 \varphi}{\partial x^2}\right)_i = \frac{1}{\Delta x^2}\left(\varphi_{i+1} - 2\varphi_i + \varphi_{i-1}\right) + O\left(\Delta x^2\right) \qquad (2.10)$$

for the polynomial of the second order and

$$\left(\frac{\partial^2 \varphi}{\partial x^2}\right)_i = \frac{1}{12\Delta x^2}\left(-\varphi_{i+2} + 16\varphi_{i+1} - 30\varphi_i + 16\varphi_{i-1} - \varphi_{i-2}\right) + O\left(\Delta x^4\right)$$
$$(2.11)$$

for the polynomial of the fourth order. The formula (2.10) can also be obtained using consequently CDS

$$\left(\frac{\partial^2 \varphi}{\partial x^2}\right)_i = \frac{1}{\Delta x}\left(\frac{\partial \varphi}{\partial x}_{i+1/2} - \frac{\partial \varphi}{\partial x}_{i-1/2}\right) \tag{2.12}$$

where $i+1/2$ and $i-1/2$ are intermediate points (see Fig. 2.1). Using again the CDS for the derivatives at intermediate points:

$$\left(\frac{\partial \varphi}{\partial x}\right)_{i+1/2} = \frac{\varphi_{i+1} - \varphi_i}{\Delta x} \tag{2.13}$$

$$\left(\frac{\partial \varphi}{\partial x}\right)_{i-1/2} = \frac{\varphi_i - \varphi_{i-1}}{\Delta x} \tag{2.14}$$

we obtain (2.10).

2.2   Two dimensional case

In the two dimensional case the function φ is the function of two variables $\varphi = \varphi(x, y)$. A sample of non-uniform grid is given in Fig. (2.2). In next chapters we will consider different grids and principles of their generation. In this chapter we consider uniform two dimensional grids (x_i, y_j) with equal spacing in both x and y directions.
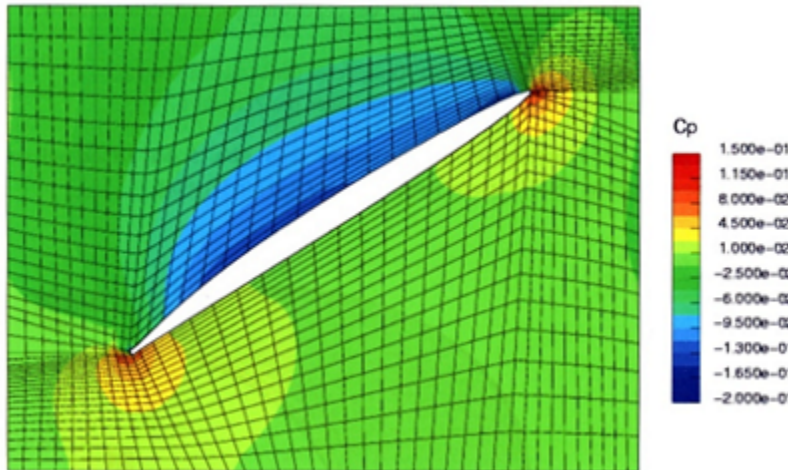
Figure 2.2: A sample of non uniform grid around the profile.

The function φ at a point (x_i, y_j) is φ_{ij}. The CDS approximation of the derivative on x at this point is:

$$\left(\frac{\partial \varphi}{\partial x}\right)_{ij} = \frac{\varphi_{i+1j} - \varphi_{i-1j}}{2\Delta x}$$

whereas on y is:

$$\left(\frac{\partial \varphi}{\partial y}\right)_{ij} = \frac{\varphi_{ij+1} - \varphi_{ij-1}}{2\Delta y}$$

2.3   Time derivatives. Explicit versus implicit

Let the unsteady partial differential equation is written in the form:

$$\frac{\partial g}{\partial t} = G(g, t) \tag{2.15}$$

The solution is known at the time instant n. The task is to find the solution at $n+1$ time instant. Using forward difference scheme we get:

$$g^{n+1} = g^n + G(g, t)\Delta t \tag{2.16}$$

Taking the r.h.s. of (2.15) from the $n - th$ time slice we obtain:

$$g^{n+1} = g^n + G(g^n, t)\Delta t \tag{2.17}$$

The scheme (2.17) is the so called explicit scheme (simple Euler approach). Taking the r.h.s. of (2.15) from the $n + 1 - th$ time slice we obtain:

$$g^{n+1} = g^n + G(g^{n+1}, t)\Delta t \tag{2.18}$$

The scheme (2.18) is the implicit scheme. The r.h.s. side of (2.18) depends on the solution g^{n+1}. With the other words, the solution at the time slice $n + 1$, g^{n+1} can not be expressed explicitly through the solutions known the from previous time slices $1, 2, .., n$ for nonlinear dependence $G(g, t)$.

Mix between explicit and implicit schemes is called the Crank-Nicolson Scheme:

$$g^{n+1} = g^n + \frac{1}{2}(G(g^n, t) + G(g^{n+1}, t))\Delta t$$

2.4   Exercises

1. Using the CDS find the derivative

$$\left[\frac{\partial}{\partial x}\left(\Gamma(x)\frac{\partial \varphi}{\partial x}\right)\right]_i = ... \tag{2.19}$$

2. Using the CDS approximate the mixed derivative

$$\frac{\partial^2 \varphi}{\partial x \partial y}_{ij} = \frac{\partial}{\partial x}\left(\frac{\partial \varphi}{\partial y}\right)_{ij} \tag{2.20}$$

3. Write the program on the language C to solve the following partial differential equation:

$$\frac{\partial \varphi}{\partial x} + \alpha \frac{\partial^2 \varphi}{\partial x^2} = f(x)$$

with the following boundary conditions:

$$\frac{\partial \varphi}{\partial x}(x = 0) = C_1$$

$$\varphi(x = 0) = C_2$$

Use the central difference scheme.

4. Write the program on the language C to solve the following partial differential equation:

$$\alpha \frac{\partial \varphi}{\partial t} + \frac{\partial^2 \varphi}{\partial x^2} = f(x, t)$$

with the following boundary conditions:

$$\frac{\partial \varphi}{\partial x}(x = 0) = C_1$$

$$\varphi(x = 0) = C_2$$

and initial condition $\varphi(x, 0) = F(x)$.

Use the explicit method and the central difference scheme for spatial derivatives.

Chapter 3

Stability and artificial viscosity of numerical methods

3.1   Artificial viscosity

Let us consider the generic linear equation:

$$\frac{\partial \xi}{\partial t} + u \frac{\partial \xi}{\partial x} = 0$$

The numerical upwind scheme (UDS) is:

$$\frac{\xi_i^{n+1} - \xi_i^n}{\Delta t} = \begin{cases} -\dfrac{u \cdot \xi_i^n - u \cdot \xi_{i-1}^n}{\Delta x} & u > 0 \\[3mm] -\dfrac{u \cdot \xi_{i+1}^n - u \cdot \xi_i^n}{\Delta x} & u < 0 \end{cases}$$

We consider only the case $u > 0$:

$$\frac{\xi_i^{n+1} - \xi_i^n}{\Delta t} = -\frac{u \cdot \xi_i^n - u \cdot \xi_{i-1}^n}{\Delta x} \qquad u > 0 \tag{3.1}$$

Taylor expansions of the function $\xi(x, t)$ in time and space gives

$$\xi_i^{n+1} = \xi_i^n + \left.\frac{\partial \xi}{\partial t}\right|_i^n \Delta t + \left.\frac{\partial^2 \xi}{\partial t^2} \frac{\Delta t^2}{2}\right|_i^n + \dots \tag{3.2}$$

$$\xi_i^n = \xi_{i-1}^n + \left.\frac{\partial \xi}{\partial x}\right|_{i-1}^n \Delta x + \left.\frac{\partial^2 \xi}{\partial x^2}\right|_{i-1}^n \frac{\Delta x^2}{2} + \dots \tag{3.3}$$

Substitution of (3.2) and (3.3) into (3.1) results in

$$\left.\frac{\partial \xi}{\partial t}\right|_i^n + \left.\frac{\partial^2 \xi}{\partial t^2}\right|_i^n \frac{\Delta t}{2} =$$

$$= -\frac{u}{\Delta x}\left(+ \left.\frac{\partial \xi}{\partial x}\right|_{i-1}^n \Delta x + \left.\frac{\partial^2 \xi}{\partial x^2}\right|_{i-1}^n \frac{\Delta x^2}{2} \right) \tag{3.4}$$

The derivatives at $i-1-th$ point can be expressed through these at $i-th$ point:

$$
\left.\frac{\partial \xi}{\partial x}\right|_{i-1}^{n} = \left.\frac{\partial \xi}{\partial x}\right|_{i}^{n} - \left.\frac{\partial^2 \xi}{\partial x^2}\right|_{i}^{n} \Delta x + \left.\frac{\partial^3 \xi}{\partial x^3}\right|_{i}^{n} \frac{\Delta x^2}{2} - ...,
$$
$$
\left.\frac{\partial^2 \xi}{\partial x^2}\right|_{i-1}^{n} = \left.\frac{\partial^2 \xi}{\partial x^2}\right|_{i}^{n} - \left.\frac{\partial^3 \xi}{\partial x^3}\right|_{i}^{n} \Delta x - ...
$$

$$(3.5)$$

The expressions (3.5) are then used in (3.4)

$$
\left.\frac{\partial \xi}{\partial t}\right|_{i}^{n} + \left.\frac{\partial^2 \xi}{\partial t^2}\right|_{i}^{n} \frac{\Delta t}{2} =
$$

$$
= -\frac{u}{\Delta x}\left(\left(\left.\frac{\partial \xi}{\partial x}\right|_{i}^{n} - \left.\frac{\partial^2 \xi}{\partial x^2}\right|_{i}^{n} \Delta x\right)\Delta x + \left(\left.\frac{\partial^2 \xi}{\partial x^2}\right|_{i}^{n} - \left.\frac{\partial^3 \xi}{\partial x^3}\right|_{i}^{n} \Delta x\right)\frac{\Delta x^2}{2} + ...\right) \quad (3.6)
$$

Finally we have:

$$
\left.\frac{\partial \xi}{\partial t}\right|_{i}^{n} + \left.\frac{\partial^2 \xi}{\partial t^2}\right|_{i}^{n} \frac{\Delta t}{2} =
$$

$$
= -\frac{u}{\Delta x}\left\{\Delta x \left.\frac{\partial \xi}{\partial x}\right|_{i}^{n} - \left.\frac{\partial^2 \xi}{\partial x^2}\right|_{i}^{n} \frac{\Delta x^2}{2} + ...\right\} \quad (3.7)
$$

Let us consider the left hand side of the equation (3.7). Differentiating $\frac{\partial \xi}{\partial t} = -u\frac{\partial \xi}{\partial x}$ on time results in

$$
\frac{\partial^2 \xi}{\partial t^2} = -u\frac{\partial}{\partial x}\left(\frac{\partial \xi}{\partial t}\right) = +u^2\frac{\partial^2 \xi}{\partial x^2} \quad (3.8)
$$

This allows one to find the derivative $\frac{\partial^2 \xi}{\partial t^2}$:

$$
\left.\frac{\partial^2 \xi}{\partial t^2}\right|_{i}^{n} = u^2 \left.\frac{\partial^2 \xi}{\partial x^2}\right|_{i}^{n} \quad (3.9)
$$

Using the last result the equation (3.7) is rewritten in form:

$$
\left.\frac{\partial \xi}{\partial t}\right|_{i}^{n} = -\frac{u}{\Delta x} \cdot \Delta x \left.\frac{\partial \xi}{\partial x}\right|_{i}^{n} + \left.\frac{\partial^2 \xi}{\partial x^2}\right|_{i}^{n} \frac{\Delta x^2}{2}\frac{u}{\Delta x} - u^2 \left.\frac{\partial^2 \xi}{\partial x^2}\right|_{i}^{n} \frac{\Delta t}{2} + ... \quad (3.10)
$$

Finally we have

$$
\boxed{\frac{\partial \xi}{\partial t} = -u\frac{\partial \xi}{\partial x} + \left(\frac{u \cdot \Delta x}{2}\left(1 - \frac{u \cdot \Delta t}{\Delta x}\right)\frac{\partial^2 \xi}{\partial x^2}\right) + ...}
$$

Compare now with the original equation:

$$\frac{\partial \xi}{\partial t} = -u \frac{\partial \xi}{\partial x}$$

The additional term

$$\left(\frac{u \cdot \Delta x}{2} \left(1 - \frac{u \cdot \Delta t}{\Delta x} \right) \frac{\partial^2 \xi}{\partial x^2} \right)$$

describes the error of numerical approximation of derivatives in the original equation (3.1). It looks like the term describing the physical diffusion $\nu \frac{\partial^2 \xi}{\partial x^2}$, where ν is the diffusion coefficient. Therefore, the error term can be interpreted as the numerical or artificial diffusion with the diffusion coefficient $\frac{u \cdot \Delta x}{2}(1 - \frac{u \cdot \Delta t}{\Delta x})$ caused by errors of equation approximation. The presence of the artificial diffusion is a serious drawback of numerical methods. It could be minimised by increase of the resolution $\Delta x \to 0$.

3.2 Stability. Courant Friedrich Levy criterion (CFL)

Let us consider the partial differential equation:

$$\frac{\partial \xi}{\partial t} + u \frac{\partial \xi}{\partial x} = 0 \qquad\qquad (3.11)$$

which is approximated using explicit method and upwind differential scheme at $u > 0$:

$$\frac{\xi_i^{n+1} - \xi_i^n}{\Delta t} = -u \frac{\xi_i^n - \xi_{i-1}^n}{\Delta x} \qquad (3.12)$$

It follows from (3.12):

$$\xi_i^{n+1} - \xi_i^n = -\frac{u \cdot \Delta t}{\Delta x}(\xi_i^n - \xi_{i-1}^n)$$

$$\xi_i^{n+1} = \xi_i^n(1 - \frac{u \cdot \Delta t}{\Delta x}) + \frac{u \cdot \Delta t}{\Delta x}\xi_{i-1}^n$$

Let us introduce the Courant Friedrich Levy parameter $c = \frac{u \cdot \Delta t}{\Delta x}$:

$$\xi_i^{n+1} = \xi_i^n(1 - c) + c\xi_{i-1}^n \qquad (3.13)$$

We consider the zero initial condition. At the time instant n we introduce the perturbation ε at the point i. The development of the perturbation is considered below in time and in x direction:

- time instant n:

$$\xi_i^n = \varepsilon$$

- time instant $n + 1$:

$$\xi_i^{n+1} = \xi_i^n(1 - c) + c \cdot \xi_{i-1}^n = \varepsilon(1 - c)$$
$$\xi_{i+1}^{n+1} = \xi_{i+1}^n(1 - c) + c \cdot \xi_i^n = c \cdot \varepsilon$$

- time instant $n + 2$:

$$\xi_i^{n+2} = \xi_i^{n+1}(1 - c) + c \cdot \xi_{i-1}^{n+1} = \varepsilon(1 - c)^2 = \varepsilon(1 - c)^2$$
$$\xi_{i+1}^{n+2} = \xi_{i+1}^{n+1}(1 - c) + c \cdot \xi_i^{n+1} = c \cdot \varepsilon(1 - c) + c \cdot \varepsilon(1 - c) = 2c \cdot \varepsilon(1 - c)$$
$$\xi_{i+2}^{n+2} = \xi_{i+2}^{n+1}(1 - c) + c \cdot \xi_{i+1}^{n+1} = c^2 \cdot \varepsilon$$

- time instant $n + 3$:

$$\xi_i^{n+3} = \xi_i^{n+2}(1 - c) + c \cdot \xi_{i-1}^{n+2} = \varepsilon(1 - c)^3$$
$$\xi_{i+1}^{n+3} = \xi_{i+1}^{n+2}(1 - c) + c \cdot \xi_i^{n+2} = 2c \cdot \varepsilon(1 - c)^2 + c \cdot \varepsilon(1 - c)^2$$
$$\xi_{i+2}^{n+3} = \xi_{i+2}^{n+2}(1 - c) + c \cdot \xi_{i+1}^{n+2} = c^2 \cdot \varepsilon(1 - c) + c^2(2\varepsilon)(1 - c)$$
$$\xi_{i+3}^{n+3} = \xi_{i+3}^{n+2}(1 - c) + c \cdot \xi_{i+2}^{n+2} = c^3 \cdot \varepsilon$$

- time instant $n + N$:

$$(\xi_{i+N}^{n+N}) = c^N \cdot \varepsilon$$

$$\dots\dots\dots\dots$$

As follows from the last formula,the perturbation decays if

$$c < 1 \qquad\qquad (3.14)$$

The condition (3.14) is the Courant Friedrich Levy criterion of the stability of explicit numerical schemes. If the velocity is changed within the computational domain, the maximum velocity u_{max} is taken instead of u in formula (3.14). Physically the condition $\frac{u_{max}\Delta t}{\Delta x} < 1$ means that the maximum displacement of the fluid particle within the time step $[t, t + \Delta t]$ does not exceed the cell size Δx. The CFL parameter c can be reduced by decrease of Δt (not by increase of Δx!).

3.3   Exercise

The field of the velocity component u_x is given as $u_{x,ij} = exp(-((i\Delta x - 0.5)^2 + (j\Delta y - 0.5)^2)$.
Calculate $u_{y,ij}$ from continuity equation (1.3) and the Δt satisfying the CFL criterion.
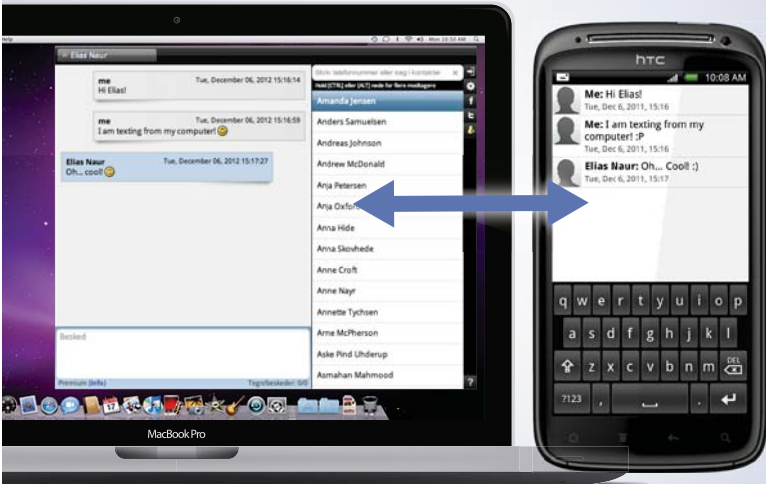
Chapter 4

Simple explicit time advance scheme for solution of the Navier Stokes Equation

4.1 Theory

The unsteady term of the Navier Stokes Equation

$$\frac{\partial u_i}{\partial t} = -\frac{\partial u_i u_j}{\partial x_j} - \frac{1}{\rho}\frac{\partial p}{\partial x_i} + \nu\frac{\partial}{\partial x_j}\frac{\partial u_i}{\partial x_j} \tag{4.1}$$

is written in explicit form:

$$u_i^{n+1} = u_i^n + \Delta t\left[-\frac{\delta u_i^n u_j^n}{\delta x_j} - \frac{1}{\rho}\frac{\delta p^n}{\partial x_i} + \nu\frac{\delta}{\delta x_j}\frac{\delta u_i^n}{\delta x_j}\right] \tag{4.2}$$

where $\frac{\delta}{\delta x_j}$ is the approximation of the derivative $\frac{\partial}{\partial x_j}$. Let us apply the divergence operator $\frac{\delta}{\delta x_i}$:

$$\frac{\delta u_i^{n+1}}{\delta x_i} = \frac{\delta u_i^n}{\delta x_i} + \Delta t\frac{\delta}{\delta x_i}\left[-\frac{\delta u_i^n u_j^n}{\delta x_j} - \frac{1}{\rho}\frac{\delta p^n}{\partial x_i} + \nu\frac{\delta}{\delta x_j}\frac{\delta u_i^n}{\delta x_j}\right] \tag{4.3}$$

Let u_i^n is the divergence free field, i.e. $\frac{\delta u_i^n}{\delta x_i} = 0$. The task is to find the velocity field at the time moment $n+1$ which is also divergence free

$$\frac{\delta u_i^{n+1}}{\delta x_i} = 0 \tag{4.4}$$

Substituting (4.4) into (4.3) one obtains:

$$\frac{\delta}{\delta x_i}\left[-\frac{\delta u_i^n u_j^n}{\delta x_j} - \frac{1}{\rho}\frac{\delta p^n}{\partial x_i} + \nu\frac{\delta}{\delta x_j}\frac{\delta u_i^n}{\delta x_j}\right] = 0 \tag{4.5}$$

Expressing (4.5) with respect to the pressure results in the Poisson equation:

$$\frac{\delta^2 p^n}{\partial x_i^2} = \rho\left[-\frac{\delta^2 u_i^n u_j^n}{\delta x_j \delta x_i} + \nu\frac{\delta^2}{\delta x_i \delta x_j}\frac{\delta u_i^n}{\delta x_j}\right] \tag{4.6}$$

The algorithm for time-advancing is as follows:

i) The solution at time n is known and divergence free.

ii) Calculation of the r.h.s. of (4.6) $\rho\left[-\frac{\delta^2 u_i^n u_j^n}{\delta x_j \delta x_i} + \nu\frac{\delta^2}{\delta x_i \delta x_j}\frac{\delta u_i^n}{\delta x_j}\right]$

iii) Calculation of the pressure p^n from the Poisson equation (4.6)

iv) Calculation of the velocity u_i^{n+1}. This is divergence free.

v) Go to the step ii).

In the following sections we consider the algorithm in details for the two dimensional case.

4.2   Mixed schemes

The high accuracy of the CDS schemes is their advantage. The disadvantage of CDS schemes is their instability resulting in oscillating solutions. On the contrary, the upwind difference schemes UDS possess a low accuracy and high stability. The idea to use the combination of CDS and UDS to strengthen their advantages and diminish their disadvantages. Let us consider a simple transport equation for the quantity φ:

$$\frac{\partial \varphi}{\partial t} + u\frac{\partial \varphi}{\partial x} = 0 \tag{4.7}$$

with $u > 0$. A simple explicit, forward time, central difference scheme for this equation may be written as

$$\varphi_i^{n+1} = \varphi_i^n - c([\varphi_i^n + \frac{1}{2}(\varphi_{i+1}^n - \varphi_i^n)] - [\varphi_{i-1}^n + \frac{1}{2}(\varphi_i^n - \varphi_{i-1}^n)]) =$$

$$= \varphi_i^n - c([\varphi_i^n - \varphi_{i-1}^n] + \frac{1}{2}[\varphi_{i+1}^n - \varphi_i^n] - \frac{1}{2}[\varphi_i^n - \varphi_{i-1}^n]) \tag{4.8}$$

where $c = \frac{u\Delta t}{\Delta_x}$ is the CFL parameter. The term $c[\varphi_i^n - \varphi_{i-1}^n]$ is the diffusive 1st order upwind contribution. The term $c(\frac{1}{2}[\varphi_{i+1}^n - \varphi_i^n] - \frac{1}{2}[\varphi_i^n - \varphi_{i-1}^n])$ is the anti-diffusive component. With TVD (total variation diminishing) schemes the anti-diffusive component is limited in order to avoid instabilities and maintain boundness $0 < \varphi < 1$:

$$\varphi_i^{n+1} = \varphi_i^n - c([\varphi_i^n - \varphi_{i-1}^n] + \frac{1}{2}[\varphi_{i+1}^n - \varphi_i^n]\Psi_{east}^n - \frac{1}{2}[\varphi_i^n - \varphi_{i-1}^n]\Psi_{west}^n) \tag{4.9}$$

where Ψ are limiters. Limiters functions for TVD schemes are given in table 4.1.

Table 4.1: **Limiters function for TVD schemes**

Scheme	Ψ
central	1
upwind	0
Roe minimod	$\Psi = max(0, min(r, 1))$
Roe superbee	$\Psi = max(0, min(2r, 1), min(r, 2))$
Van Leer	$\Psi = \frac{r + mod(r)}{1 + mod(r)}$
Branley and Jones	$\Psi = max(0, min(2r, 1))$

Here $r = (\frac{\partial \varphi}{\partial x})^n_{west} / (\frac{\partial \varphi}{\partial x})^n_{east}$, $(\frac{\partial \varphi}{\partial x})^n_{east} = \frac{\varphi^n_{i+1} - \varphi^n_i}{x_{i+1} - x_i}$. The mixed upwind and central difference scheme are used in Sec. 4.4 for approximation of the convective terms with the limiter (4.14).
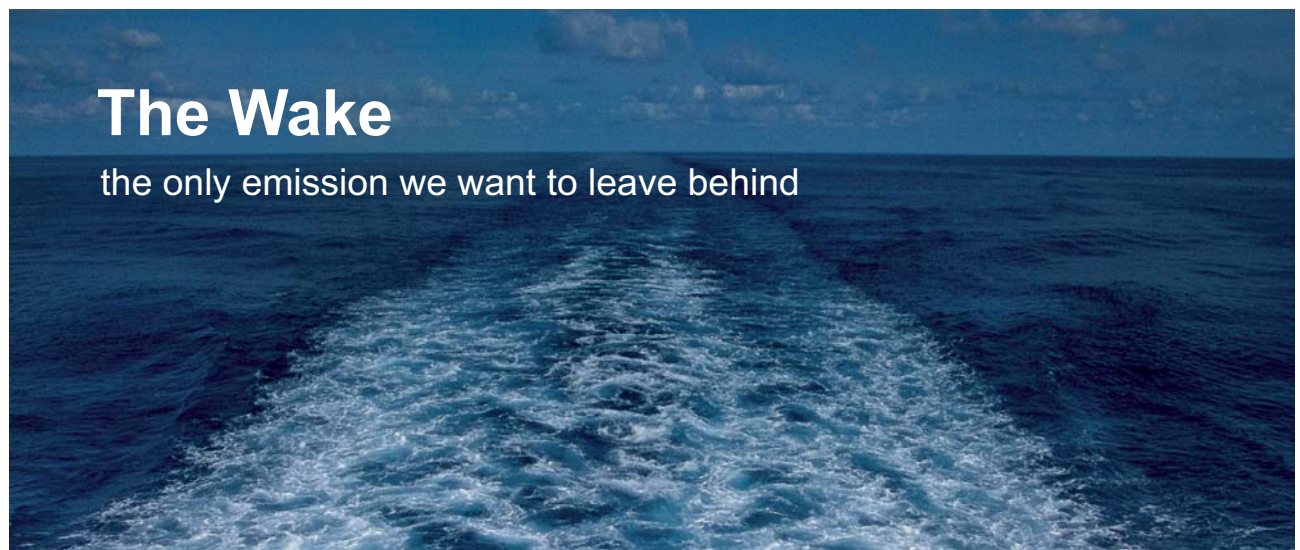
4.3   Staggered grid

The grids are subdivided into collocated and staggered ones. On collocated grids the unknown quantities are stored at centres of cells (points P in Fig. 4.1). The equations are also satisfied at cell centres. For the simplicity, we considered the case Δ_x and Δ_y are constant in the whole computational domain. Use of collocated grids meets the problem of decoupling between the velocity and pressure fields. Let us consider the Poisson equation (4.6) with the r.h.s.

$$\frac{\partial T_x}{\partial x} + \frac{\partial T_y}{\partial y} = \frac{\partial H_x}{\partial x} + \frac{\partial H_y}{\partial y} + \frac{\partial D_x}{\partial x} + \frac{\partial D_y}{\partial y}$$

where

$$D_x = \nu \frac{\partial^2 u_x}{\partial x^2} + \nu \frac{\partial^2 u_x}{\partial y^2}$$

$$D_y = \nu \frac{\partial^2 u_y}{\partial x^2} + \nu \frac{\partial^2 u_y}{\partial y^2}$$

$$H_x = -\frac{\partial u_x u_x}{\partial x} - -\frac{\partial u_x u_y}{\partial y} \qquad (4.10)$$

$$H_y = -\frac{\partial u_x u_y}{\partial x} - -\frac{\partial u_y u_y}{\partial y}$$

Application of the central difference scheme to the Poisson equation results in

$$\frac{(\frac{\partial p^n}{\partial x})_E - (\frac{\partial p^n}{\partial x})_W}{2\Delta_x} + \frac{(\frac{\partial p^n}{\partial y})_N - (\frac{\partial p^n}{\partial y})_S}{2\Delta_y} = \frac{T_{x,E}^n - T_{x,W}^n}{2\Delta_x} + \frac{T_{y,N}^n - T_{y,S}^n}{2\Delta_y}$$

or

$$\frac{\frac{p_{EE}^n - p_P^n}{2\Delta_x} - \frac{p_P^n - p_{WW}^n}{2\Delta_x}}{2\Delta_x} + \frac{\frac{p_{NN}^n - p_P^n}{2\Delta_y} - \frac{p_P^n - p_{SS}^n}{2\Delta_y}}{2\Delta_y} = \frac{T_{x,E}^n - T_{x,W}^n}{2\Delta_x} + \frac{T_{y,N}^n - T_{y,S}^n}{2\Delta_y} = Q_P^H$$

The last equation is expressed in the matrix form:

$$A_P^p p_P^n + \sum_l A_l^p p_l^n = -Q_P^H \qquad (4.11)$$

where

$$l = EE, WW, NN, SS, \ A_{EE}^p = A_{WW}^p = -\frac{1}{(2\Delta_x)^2}, \ A_{NN}^p = A_{SS}^p = -\frac{1}{(2\Delta_y)^2}$$
and $A_P^p = -\sum_l A_l^p$

This equation (4.11) has involves nodes which are 2Δ apart (see also [3])! It is a discretized Poisson equation on a grid twice as coarse as the basic one but the equations split into four unconnected systems, one with i and j both even, one with i even and j odd, one with i odd and j even, and one with both odd. Each of these systems gives a different solution. For a flow with a uniform pressure field, the checkerboard pressure distribution shown in Fig. 4.2 satisfies these equations and could be produced. However, the pressure gradient is not affected and the velocity field may be smooth.
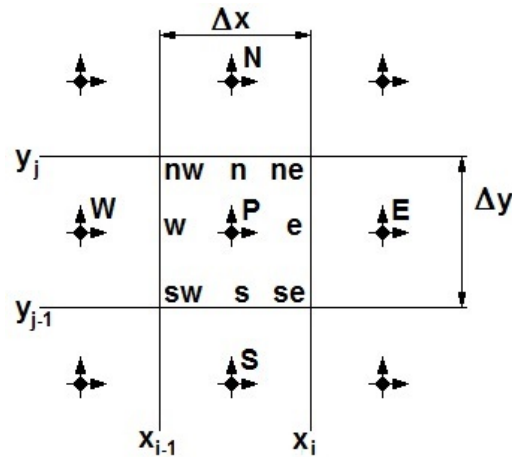
Figure 4.1: Sample of the collocated grid.
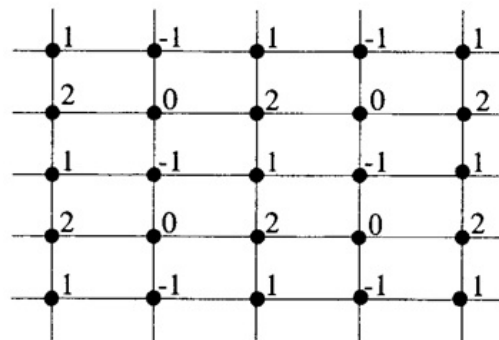
Figure 4.2: Checkerboard pressure solution on the collocated grid.

Numeration of points at which the X-components
of velocity (designated by U) are stored

Numeration of points at which the Y-components
of velocity (designated by V) are stored

x - arepoints at which the pressure P is stored
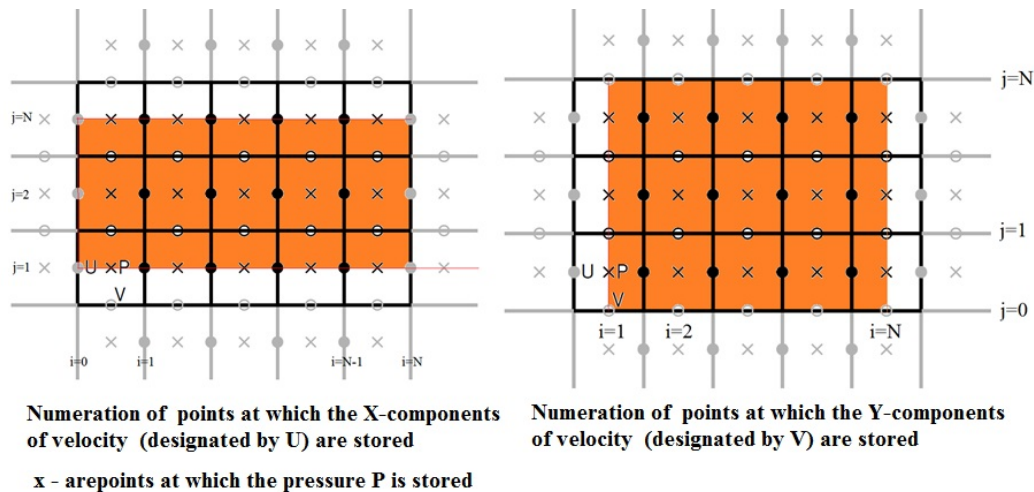
Figure 4.3: Grid points of staggered grid.

There is also the possibility that one may not be able to obtain a converged steady-state solution.

A possible solution of the problem is the application of the staggered grids (Fig. 4.3). The Poisson equation is satisfied at cell centres designated by crosses. The u_x velocities are stored at points staggered by $\Delta_x/2$ in x-direction (filled circles). At these points the first Navier- Stokes equation is satisfied:

$$\frac{\partial u_x}{\partial t} = -\frac{\partial u_x u_j}{\partial x_j} - \frac{1}{\rho}\frac{\partial p}{\partial x} + \nu\frac{\partial}{\partial x_j}\frac{\partial u_x}{\partial x_j} \tag{4.12}$$

The u_y velocities are stored at points staggered by $\Delta_y/2$ in y-direction (circles). At these points the second Navier-Stokes equation is satisfied:

$$\frac{\partial u_y}{\partial t} = -\frac{\partial u_y u_j}{\partial x_j} - \frac{1}{\rho}\frac{\partial p}{\partial y} + \nu\frac{\partial}{\partial x_j}\frac{\partial u_y}{\partial x_j} \tag{4.13}$$

The staggered grid is utilized below.

4.4 Approximation of $-\frac{\delta u_i^n u_j^n}{\delta x_j}$

The approximation of the convective term is a very critical point. For faster flows or larger time steps, the discretization shall be closer to an upwinding approach [4]. Following to [4] we implement a smooth transition between centered differencing and upwinding using a parameter $\gamma \in [0, 1]$. It is defined as

$$\gamma = min(1.2 \cdot \Delta t \cdot max(|u_x(i, j)|, |u_y(i, j)|), 1) \tag{4.14}$$

The value of gamma is the maximum fraction of a cells which information can travel in one time step, multiplied by 1.2, and capped by 1. The factor of 1.2 is taken from the experience that often times tending a bit more towards upwinding can be advantageous for accuracy [5].

$\gamma = 0$ corresponds to the central difference scheme (CDS) whereas $\gamma = 1$ results in the upwind difference scheme (UDS).

4.4.1 Approximation of $-\frac{\partial u_x u_x}{\partial x} - \frac{\partial u_x u_y}{\partial y} = -u_x\frac{\partial u_x}{\partial x} - u_y\frac{\partial u_x}{\partial y}$

- Point $(i + 1/2, j)$ for x-component of velocity:

  $u_x(i + 1/2, j) = (u_x(i + 1, j) + u_x(i, j))/2.0$
  If $u_x(i + 1/2, j) \geq 0$,

  then $u_x u_x|_{i+1/2,j} = u_x(i + 1/2, j)(\frac{1-\gamma}{2}u_x(i + 1, j) + \frac{\gamma + 1}{2}u_x(i, j))$

  else $u_x u_x|_{i+1/2,j} = u_x(i + 1/2, j)(\frac{\gamma + 1}{2}u_x(i + 1, j) + \frac{1-\gamma}{2}u_x(i, j))$

- Point $(i - 1/2, j)$ for x-component of velocity:

  $u_x(i - 1/2, j) = (u_x(i, j) + u_x(i - 1, j))/2.0$
  If $u_x(i - 1/2, j) \geq 0$,

then $u_x u_x|_{i-1/2,j} = u_x(i-1/2, j)(\dfrac{1-\gamma}{2}u_x(i, j) + \dfrac{\gamma+1}{2}u_x(i-1, j))$

else $u_x u_x|_{i-1/2,j} = u_x(i-1/2, j)(\dfrac{\gamma+1}{2}u_x(i, j) + \dfrac{1-\gamma}{2}u_x(i-1, j))$

- Point $(i + 1/2, j)$ for y-component of velocity:

  $u_y(i + 1/2, j) = (u_y(i + 1, j) + u_y(i, j))/2.0$
  If $u_y(i + 1/2, j) \geq 0$,

  then $u_x u_y|_{i+1/2,j} = u_y(i + 1/2, j)(\dfrac{\gamma+1}{2}u_x(i, j) + \dfrac{1-\gamma}{2}u_x(i, j + 1))$

  else $u_x u_y|_{i+1/2,j} = u_y(i + 1/2, j)(\dfrac{1-\gamma}{2}u_x(i, j) + \dfrac{\gamma+1}{2}u_x(i, j + 1))$

- Point $(i + 1/2, j - 1)$ for y-component of velocity:

$u_y(i + 1/2, j - 1) = (u_y(i + 1, j - 1) + u_y(i, j - 1))/2.0$
If $u_y(i + 1/2, j - 1) \geq 0$,

then $u_x u_y|_{i+1/2,j-1} = u_y(i + 1/2, j - 1)(\dfrac{\gamma+1}{2}u_x(i, j - 1) + \dfrac{1-\gamma}{2}u_x(i, j))$

else $u_x u_y|_{i+1/2,j-1} = u_y(i + 1/2, j - 1)(\dfrac{1-\gamma}{2}u_x(i, j - 1) + \dfrac{\gamma+1}{2}u_x(i, j))$

$H_x(i, j) = -\dfrac{\partial u_x u_x}{\partial x} - \dfrac{\partial u_x u_y}{\partial y} =$

$-\dfrac{u_x u_x|_{i+1/2,j} - u_x u_x|_{i-1/2,j}}{\Delta_x} - \dfrac{u_x u_y|_{i+1/2,j} - u_x u_y|_{i+1/2,j-1}}{\Delta_y}$

4.4.2 Approximation of $-\frac{\partial u_x u_y}{\partial x} - \frac{\partial u_y u_y}{\partial y} = -u_x\frac{\partial u_y}{\partial x} - u_y\frac{\partial u_y}{\partial y}$

- Point $(i, j + 1/2)$ for y-component of velocity:

  $u_y(i, j + 1/2) = (u_y(i, j) + u_y(i, j + 1))/2.0$
  If $u_y(i, j + 1/2) \geq 0$,

  then $u_y u_y|_{i,j+1/2} = u_y(i, j + 1/2)(\dfrac{1-\gamma}{2}u_y(i, j + 1) + \dfrac{\gamma+1}{2}u_y(i, j))$

  else $u_y u_y|_{i,j+1/2} = u_y(i, j + 1/2)(\dfrac{\gamma+1}{2}u_y(i, j + 1) + \dfrac{1-\gamma}{2}u_y(i, j))$

- Point $(i, j - 1/2)$ for y-component of velocity:

  $u_y(i, j - 1/2) = (u_y(i, j - 1) + u_y(i, j))/2.0$
  If $u_y(i, j - 1/2) \geq 0$,

  then $u_y u_y|_{i,j-1/2} = u_y(i, j - 1/2)(\dfrac{1-\gamma}{2}u_y(i, j) + \dfrac{\gamma+1}{2}u_y(i, j - 1))$

  else $u_y u_y|_{i,j-1/2} = u_y(i, j - 1/2)(\dfrac{\gamma+1}{2}u_y(i, j) + \dfrac{1-\gamma}{2}u_y(i, j - 1))$

- Point $(i, j + 1/2)$ for x-component of velocity:

$u_x(i, j + 1/2) = (u_x(i, j + 1) + u_x(i, j))/2.0$
If $u_x(i, j + 1/2) \geq 0$,

then $u_y u_x|_{i,j+1/2} = u_x(i, j + 1/2)(\frac{\gamma + 1}{2} u_y(i, j) + \frac{1 - \gamma}{2} u_y(i + 1, j))$

else $u_y u_x|_{i,j+1/2} = u_x(i, j + 1/2)(\frac{1 - \gamma}{2} u_y(i, j) + \frac{\gamma + 1}{2} u_y(i + 1, j))$

- Point $(i - 1, j + 1/2)$ for x-component of velocity:

$u_x(i - 1, j + 1/2) = (u_x(i - 1, j + 1) + u_x(i - 1, j))/2.0$
If $u_x(i - 1, j + 1/2) \geq 0$,

then $u_y u_x|_{i-1,j+1/2} = u_x(i - 1, j + 1/2)(\frac{\gamma + 1}{2} u_y(i - 1, j) + \frac{1 - \gamma}{2} u_y(i, j))$

else $u_y u_x|_{i-1,j+1/2} = u_x(i - 1, j + 1/2)(\frac{1 - \gamma}{2} u_y(i - 1, j) + \frac{\gamma + 1}{2} u_y(i, j))$

$H_y(i, j) = -\frac{\partial u_x u_y}{\partial x} - \frac{\partial u_y u_y}{\partial y} =$

$- \frac{u_y u_x|_{i,j+1/2} - u_y u_x|_{i-1,j+1/2}}{\Delta_x} - \frac{u_y u_y|_{i,j+1/2} - u_y u_y|_{i,j-1/2}}{\Delta_y}$

4.5 Approximation of $\frac{\delta}{\delta x_j} \frac{\delta u_i^n}{\delta x_j}$

The second derivative is calculated using the Central Difference Scheme (CDS):

$$D_x(i,j) = \frac{u_x(i+1,j) - 2u_x(i,j) + u_x(i-1,j)}{\Delta_x^2} + \frac{u_x(i,j+1) - 2u_x(i,j) + u_x(i,j-1)}{\Delta_y^2}$$

$$D_y(i,j) = \frac{u_y(i+1,j) - 2u_y(i,j) + u_y(i-1,j)}{\Delta_x^2} + \frac{u_y(i,j+1) - 2u_y(i,j) + u_y(i,j-1)}{\Delta_y^2}$$

4.6 Calculation of the r.h.s. for the Poisson equation (4.6)

The r.h.s. of (4.6) is

$$-\frac{\delta^2 u_i^n u_j^n}{\delta x_j \delta x_i} + \nu \frac{\delta^2}{\delta x_i \delta x_j} \frac{\delta u_i^n}{\delta x_j} = \frac{\partial H_x}{\partial x} + \frac{\partial H_y}{\partial y} + \frac{\partial D_x}{\partial x} + \frac{\partial D_y}{\partial y}$$

The derivatives at the point (i,j) of the pressure storage (designated as X in Fig. 4.3) are calculated using CDS

$$\frac{\partial H_x}{\partial x}\Big|_{ij} = \frac{H_x(i,j) - H_x(i-1,j)}{\Delta x}, \frac{\partial D_x}{\partial x}\Big|_{ij} = \frac{D_x(i,j) - D_x(i-1,j)}{\Delta x},$$

$$\frac{\partial H_y}{\partial y}\Big|_{ij} = \frac{H_y(i,j) - H_y(i,j-1)}{\Delta y}, \frac{\partial D_y}{\partial y}\Big|_{ij} = \frac{D_y(i,j) - D_y(i,j-1)}{\Delta y}$$

4.7 Solution of the Poisson equation (4.6)

The numerical solution of the Poisson equation is discussed in [3].

4.8 Update the velocity field

The velocity field is updated according to formula

$$u_x^{n+1}(i,j) = u_x^n(i,j) + \Delta_t(H_x^n(i,j) + D_x^n(i,j) - (p^n(i+1,j) - p^n(i,j))/\Delta_x)$$

$$u_y^{n+1}(i,j) = u_y^n(i,j) + \Delta_t(H_y^n(i,j) + D_y^n(i,j) - (p^n(i,j+1) - p^n(i,j))/\Delta_y)$$

4.9 Boundary conditions for the velocities

At this stage, the boundary conditions (BC) for the velocity field should be taken into account. The nodes at which the BC are enforced are shown by grey symbols in Fig. 4.3. Enforcement of the BC is easy, if the "grey" point lies exactly at the boundary of the computational domain. If not, two cases should be considered. If the Neumann condition is enforced $\frac{\partial u}{\partial n} = C$, the velocity component outside of the boundary $u(0)$ is calculated through the interior quantity $u(1)$ from

$$\frac{u(1) - u(0)}{\Delta_n} = C$$

If the Dirichlet condition $u = C$ is enforced and the point 0 is outside of the computational domain, the value $u(0)$ is calculated from the extrapolation procedure:

$$\frac{u(0) + u(1)}{2} = C$$

4.10 Calculation of the vorticity

The calculation of vorticity $\omega_z = \frac{\partial u_x}{\partial y} - \frac{\partial u_y}{\partial x}$ is performed as follows:

$$u_x(i - 1/2, j + 1/2) = \frac{1}{4}(u_x(i, j) + u_x(i, j + 1) + u_x(i - 1, j) + u_x(i - 1, j + 1)),$$

$$u_x(i - 1/2, j - 1/2) = \frac{1}{4}(u_x(i, j) + u_x(i - 1, j) + u_x(i, j - 1) + u_x(i - 1, j - 1)),$$

$$u_y(i + 1/2, j - 1/2) = \frac{1}{4}(u_y(i, j) + u_y(i + 1, j) + u_y(i, j - 1) + u_y(i + 1, j - 1)),$$

$$u_y(i - 1/2, j - 1/2) = \frac{1}{4}(u_y(i, j) + u_y(i - 1, j) + u_y(i, j - 1) + u_y(i - 1, j - 1)),$$

$$\omega_z(i, j) = \frac{u_x(i - 1/2, j + 1/2) - u_x(i - 1/2, j - 1/2)}{\Delta_y} -$$

$$- \frac{u_y(i + 1/2, j - 1/2) - u_y(i - 1/2, j - 1/2)}{\Delta_x}$$

Chapter 5

Splitting schemes for solution of multidimensional problems

5.1 Splitting in spatial directions. Alternating direction implicit (ADI) approach

Let us consider the two dimensional unsteady heat conduction equation:

$$\frac{\partial \phi}{\partial t} = \lambda \left(\frac{\partial^2 \phi}{\partial x^2} + \frac{\partial^2 \phi}{\partial y^2} \right) \tag{5.1}$$

We use implicit scheme proposed by Crank and Nicolson and CDS for spatial derivatives:

$$\frac{\phi^{n+1} - \phi^n}{\Delta t} = \frac{\lambda}{2} \left[\left(\frac{\partial^2 \phi^n}{\partial x^2} + \frac{\partial^2 \phi^n}{\partial y^2} \right) + \left(\frac{\partial^2 \phi^{n+1}}{\partial x^2} + \frac{\partial^2 \phi^{n+1}}{\partial y^2} \right) \right] \tag{5.2}$$
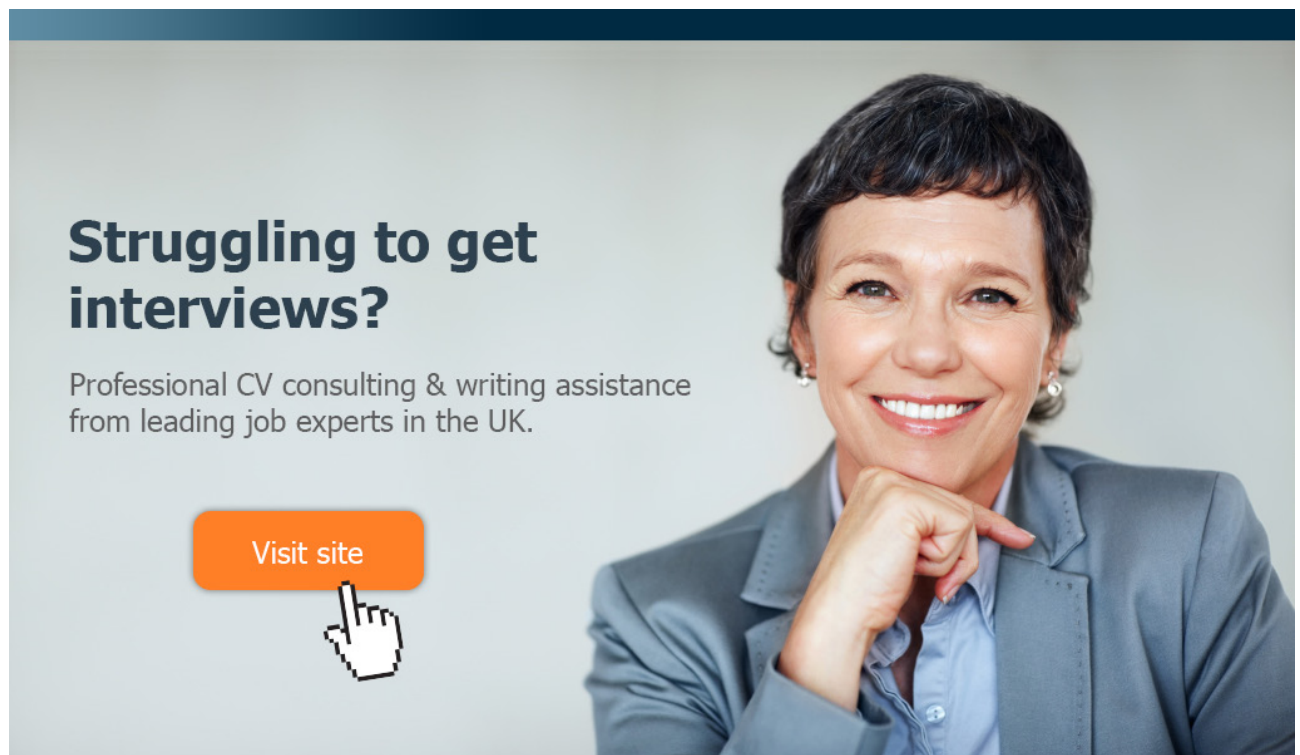
$$\left(\frac{\partial^2 \phi^n}{\partial x^2}\right)_{i,j} = \frac{\phi_{i+1,j}^n - 2\phi_{i,j}^n + \phi_{i-1,j}^n}{(\Delta x)^2} \tag{5.3}$$

$$\left(\frac{\partial^2 \phi^n}{\partial y^2}\right)_{i,j} = \frac{\phi_{i,j+1}^n - 2\phi_{i,j}^n + \phi_{i,j-1}^n}{(\Delta y)^2} \tag{5.4}$$

In what follows we use the designations for derivative approximations:

$$\frac{\delta^2}{\delta x^2}\phi^n = \frac{\phi_{i+1,j}^n - 2\phi_{i,j}^n + \phi_{i-1,j}^n}{(\Delta x)^2} \tag{5.5}$$

$$\frac{\delta^2}{\delta y^2}\phi^n = \frac{\phi_{i,j+1}^n - 2\phi_{i,j}^n + \phi_{i,j-1}^n}{(\Delta y)^2} \tag{5.6}$$

Using these designations we get from the original heat conduction equation:

$$\left(1 - \frac{\lambda \Delta t}{2}\frac{\delta^2}{\delta x^2}\right)\left(1 - \frac{\lambda \Delta t}{2}\frac{\delta^2}{\delta y^2}\right)\phi^{n+1} = \left(1 + \frac{\lambda \Delta t}{2}\frac{\delta^2}{\delta x^2}\right)\left(1 + \frac{\lambda \Delta t}{2}\frac{\delta^2}{\delta y^2}\right)\phi^n +$$
$$+ \frac{(\lambda \Delta t)^2}{4}\frac{\delta^2}{\delta x^2}\left[\frac{\delta^2}{\delta y^2}\left(\phi^{n+1} - \phi^n\right)\right]$$

$$\tag{5.7}$$

The last term is neglected since $(\phi^{n+1} - \phi^n)(\Delta t)^2 \sim \frac{\partial \phi}{\partial t}(\Delta t)^3$.
Numerical solution is performed in two following steps:

- Step 1: Solution of one dimensional problem in x-direction:

$$\left(1 - \frac{\lambda \Delta t}{2}\frac{\delta^2}{\delta x^2}\right)\phi^* = \left(1 + \frac{\lambda \Delta t}{2}\frac{\delta^2}{\delta y^2}\right)\phi^n \tag{5.8}$$

  The numerical solution of (5.8) ϕ^* is then substituted as the guess solution for the next step:

- Step 2: Solution of one dimensional problem in y-direction

$$\left(1 - \frac{\lambda \Delta t}{2}\frac{\delta^2}{\delta y^2}\right)\phi^{n+1} = \left(1 + \frac{\lambda \Delta t}{2}\frac{\delta^2}{\delta x^2}\right)\phi^* \tag{5.9}$$

It can be shown that the resulting method is of the second order of accuracy and unconditionally stable.

5.2 Splitting according to physical processes. Fractional step methods

Within the fractional step method the original equation is split according to physical processes. Splitting according to physical processes is used for unsteady problems. The general idea is illustrated for the transport equation:

$$\frac{\partial u}{\partial t} = Cu + Du + P \qquad (5.10)$$

Here

C is the convection operator,

D is the diffusion operator,

P is the pressure source operator.

Simple explicit Euler method can be written as

$$u^{n+1} = u^n + (Cu + Du + P)\Delta t \qquad (5.11)$$

The overall numerical solution is considered as the consequence of numerical solutions of the following partial problems:

$$
\begin{aligned}
u^* &= u^n + (Cu^n)\Delta t \quad &(*)\ \text{Convection step} \\
u^{**} &= u^* + (Du^*)\Delta t \quad &(**)\ \text{Diffusion step} \\
u^{n+1} &= u^{**} + (P)\Delta t \quad &(***)\ \text{Pressure step}
\end{aligned}
\qquad (5.12)
$$

solving sequentially. The sense of this splitting is that the numerical solution of partial problems (*)-(***) is simpler and more stable than that of the whole problem. The disadvantage of this procedure is that it is applicable to only unsteady problem formulation. Another disadvantage is the low order of accuracy with respect to time derivative approximation. The order of time derivative approximations can be derived using the sample with two physical processes described by operators L_1 and L_2:

$$\frac{\partial u}{\partial t} = L_1(u) + L_2(u) \qquad (5.13)$$

The splitting of (5.10) results in two steps procedure:

$$
\begin{aligned}
\frac{\partial u^*}{\partial t} &= L_1(u^*), \quad u^*|_{t=t_n} = u^n \\
\frac{\partial u^{n+1}}{\partial t} &= L_2(u^{n+1}), \quad u^{n+1}|_{t=t_n} = u^*
\end{aligned}
\qquad (5.14)
$$

where

$$u^* = u^n + \Delta t L_1(u^n) + O(\Delta t^2),$$

$$u^{n+1} = u^* + \Delta t L_2(u^*) + O(\Delta t^2) =$$

$$= u^n + \Delta t L_1(u^n) + \Delta t L_2(u^n + \Delta t L_1(u^n)) + O(\Delta t^2) =$$

$$= u^n + \Delta t (L_1(u^n) + L_2(u^n)) + O(\Delta t^2). \tag{5.15}$$

The accuracy of the final solution u^{n+1} is of the first order in time.

Very often the diffusion step is treated implicitly. This is done to diminish the time step restriction for the diffusion process. Otherwise, the stability requires Δt to be proportional to the spacial discretization squared, if a pure explicit scheme is applied. The semi implicit scheme for the two dimensional Navier Stokes equation reads:

- Convection step is treated explicitly:

$$\frac{u_x^* - u_x^n}{\Delta t} = -\frac{\delta u_x^n u_x^n}{\delta x} - \frac{\delta u_x^n u_y^n}{\delta y} \tag{5.16}$$

$$\frac{u_y^* - u_y^n}{\Delta t} = -\frac{\delta u_y^n u_x^n}{\delta x} - \frac{\delta u_y^n u_y^n}{\delta y} \tag{5.17}$$

- The solutions $u_{x,y}^*$ are used then for the diffusion process which is treated implicitly:

$$\frac{u_x^{**} - u_x^*}{\Delta t} = \nu\left(\frac{\delta^2 u_x^{**}}{\delta x^2} + \frac{\delta^2 u_x^{**}}{\delta y^2}\right) \tag{5.18}$$

$$\frac{u_y^{**} - u_y^*}{\Delta t} = \nu\left(\frac{\delta^2 u_y^{**}}{\delta x^2} + \frac{\delta^2 u_y^{**}}{\delta y^2}\right) \tag{5.19}$$

- The solutions $u_{x,y}^{**}$ are used then for the next process which is treated explicitly:

$$\frac{u_x^{n+1} - u_x^{**}}{\Delta t} = -\frac{\delta p^{n+1}}{\delta x} \tag{5.20}$$

$$\frac{u_y^{n+1} - u_y^{**}}{\Delta t} = -\frac{\delta p^{n+1}}{\delta y} \tag{5.21}$$

where the pressure p^{n+1} should be pre computed from the continuity equation demanding the velocity at $n + 1$ time slice is divergency free:

$$\frac{\delta u_x^{n+1}}{\delta x} + \frac{\delta u_y^{n+1}}{\delta y} = 0 \tag{5.22}$$

Applying the operator ∇ to the equations (5.20) and (5.21) we get the Poisson equation for the pressure:

$$\frac{\delta^2 p^{n+1}}{\delta x^2} + \frac{\delta^2 p^{n+1}}{\delta y^2} = \frac{1}{\Delta t}\left(\frac{\delta u_x^{**}}{\delta x} + \frac{\delta u_y^{**}}{\delta y}\right) \tag{5.23}$$

5.3 Increase of the accuracy of time derivatives approximation using the Lax-Wendroff scheme

Let us consider the general transport equation:

$$\frac{\partial u}{\partial t} + \frac{\partial F(u)}{\partial x} = 0 \tag{5.24}$$

We introduce the following designations:

$$A = \frac{\partial F}{\partial u}$$

$$u_{tt} = -F_{xt} = -F_{tx}, \quad F_t = F_u u_t = -F_u F_x \equiv -AF_x \tag{5.25}$$

Substitution of these results into the time Taylor series gives the Lax-Wendroff scheme which is of the second order in time:

$$u(t + \tau) = u(t) + \tau u_t(t) + \frac{\tau^2}{2} u_{tt}(t) + O(\tau^3)$$
$$= u(t) - \tau F_x(t) + \frac{\tau^2}{2} (A(t) F_x(t))_x + O(\tau^3) \qquad (5.26)$$

A difficulty arising in the LW approach is the computation of the operator A. One can easy derive that the Lax Wendroff scheme results in the solution of the equation:

$$\frac{u^{n+1} - u^n}{\tau} + \frac{\partial F^n}{\partial x} = \frac{\tau}{2} \frac{\partial}{\partial x} \left(A^n \frac{\partial F^n}{\partial x} \right)$$
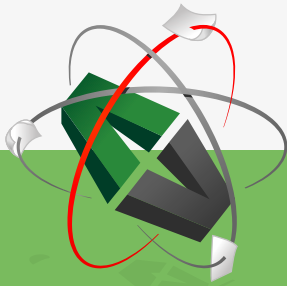
Chapter 6

Finite Volume Method

6.1 Transformation of the Navier-Stokes Equations in the Finite Volume Method

The Navier Stokes equation

$$\frac{\partial u_i}{\partial t} + \frac{\partial(u_i u_j)}{\partial x_j} = F_i - \frac{1}{\rho}\frac{\partial p}{\partial x_i} + \nu\frac{\partial}{\partial x_j}\left(\frac{\partial}{\partial x_j}u_i\right) \qquad (6.1)$$

is fulfilled within each mesh element (finite volume U) in the integral sense. For that it is integrated over the volume U:

$$\int\limits_U\left[\frac{\partial u_i}{\partial t} + \frac{\partial(u_i u_j)}{\partial x_j}\right]dU = \int\limits_U\left[F_i - \frac{1}{\rho}\frac{\partial p}{\partial x_i} + \nu\frac{\partial}{\partial x_j}\left(\frac{\partial}{\partial x_j}u_i\right)\right]dU \qquad (6.2)$$

Application of the Gauss theorem results in

$$\frac{\partial}{\partial t}\int\limits_U u_i\,dU + \int\limits_S u_i\vec{u}\vec{n}\,dS = \int\limits_U F_i\,dU - \frac{1}{\rho}\int\limits_S p\vec{e_i}\vec{n}\,dS + \nu\int\limits_S grad u_i\vec{n}\,dS \quad (6.3)$$

The same procedure applied to the continuity equation gives

$$\int\limits_S \vec{u}\vec{n}\,dS = 0 \qquad (6.4)$$
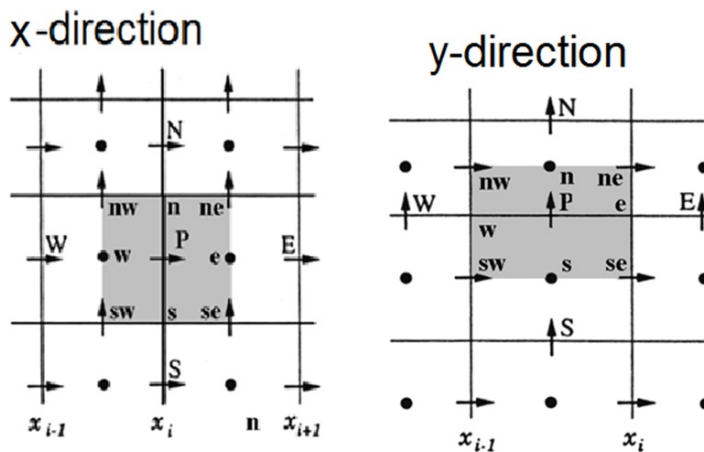
Figure 6.1: Staggered arrangement of finite volumes.

6.2   Sample

Let us consider the two dimensional transport equation without the diffusion term

$$\begin{cases} \dfrac{\partial u_i}{\partial t} + \dfrac{\partial u_i u_j}{\partial x_j} = -\dfrac{\partial p}{\partial x_i} \\[4mm] \qquad\quad \dfrac{\partial u_j}{\partial x_j} = 0 \end{cases} \qquad (6.5)$$

In the integral form this equation reads

$$\frac{\partial}{\partial t} \int\limits_U u_i \, dU + \int\limits_S u_i \vec{u}\vec{n} \, dS = -\int\limits_S p\vec{e}_i \vec{n} \, dS \qquad (6.6)$$

We use the staggered grid (Fig. 13.2). The pressure is stored at the volume centers. The u_x velocity is stored at the centers of vertical faces, whereas the velocity u_y component at centers of horizontal faces. The x- equation is satisfied for volumes displaced in x-direction, whereas the y-equation for these displaced in y-direction.
Below we consider approximations of different terms:

6.2.1   Pressure and unsteady terms

Source (pressure) term for x-equation:

$$Q_1^p = -\int\limits_S p\vec{e}_1 \vec{n} \, dS \approx -\left(p_e S_e - p_w S_w \right) = -\left(p_{i+1j} - p_{ij} \right)\Delta \qquad (6.7)$$

Unsteady term for x-equation:

$$\frac{\partial}{\partial t} \int\limits_U u_x \, dU = \Delta^2 \frac{u_{xij}^{n+1} - u_{xij}^n}{\Delta t} \qquad (6.8)$$

Pressure term for y-equation:

$$Q_2^p = -\int\limits_S p\vec{e}_2 \vec{n} \, dS \approx -\left(p_n S_n - p_s S_s \right) = -\left(p_{ij+1} - p_{ij} \right)\Delta \qquad (6.9)$$

Unsteady term for y-equation:

$$\frac{\partial}{\partial t} \int\limits_U u_y \, dU = \Delta^2 \frac{u_{yij}^{n+1} - u_{yij}^n}{\Delta t} \qquad (6.10)$$

6.2.2 Convection term of the x-equation

The integrand in convection term $u_i \vec{u} \vec{n}$ is represented in the table 6.1.

Table 6.1: $\vec{n}\vec{u}$ and u_i at different sides. x-equation

side	$\vec{n}\vec{u}$	u_i
east	u_{xe}	u_{xe}
west	$-u_{xw}$	u_{xw}
north	u_{yn}	u_{xn}
south	$-u_{ys}$	u_{xs}

The necessary velocities are approximated as shown in the table 6.2. Herewith the convection term has the form presented in the table 6.3.

6.2.3 Convection term of the y-equation

The integrand in convection term $u_i \vec{u} \vec{n}$ is represented in the table 6.4. The necessary velocities are approximated as shown in the table 6.5. Herewith the convection term has the form presented in the table 6.6.

Table 6.2: **Velocities at different sides. x-equation**

velocity	approximation
u_{xe}	$u_{xe} = \frac{1}{2}(u_{xij} + u_{xi+1j})$
u_{xw}	$u_{xw} = \frac{1}{2}(u_{xij} + u_{xi-1j})$
u_{xn}	$u_{xn} = \frac{1}{2}(u_{xij} + u_{xij+1})$
u_{xs}	$u_{xs} = \frac{1}{2}(u_{xij} + u_{xij-1})$
u_{yn}	$u_{yn} = \frac{1}{2}(u_{yij} + u_{yi+1j})$
u_{ys}	$u_{ys} = \frac{1}{2}(u_{yij-1} + u_{yi+1j-1})$

Table 6.3: **Convection flux. x-equation**

side	flux
east	$\frac{\Delta}{4}(u_{xij} + u_{xi+1j})^2$
west	$-\frac{\Delta}{4}(u_{xij} + u_{xi-1j})^2$
north	$\frac{\Delta}{4}(u_{xij} + u_{xij+1})(u_{yij} + u_{yi+1j})$
south	$-\frac{\Delta}{4}(u_{xij} + u_{xij-1})(u_{yi+1j-1} + u_{yij-1})$

Table 6.4: $\vec{n}\vec{u}$ **and** u_i **at different sides. y-equation**

side	$\vec{n}\vec{u}$	u_i
east	u_{xe}	u_{ye}
west	$-u_{xw}$	u_{yw}
north	u_{yn}	u_{yn}
south	$-u_{ys}$	u_{ys}

Table 6.5: **Velocities at different sides. y-equation**

velocity	approximation
u_{xe}	$u_{xe} = \frac{1}{2}(u_{xij} + u_{xij+1})$
u_{xw}	$u_{xw} = \frac{1}{2}(u_{xi-1j} + u_{xi-1j+1})$
u_{yn}	$u_{yn} = \frac{1}{2}(u_{yij} + u_{yij+1})$
u_{ys}	$u_{ys} = \frac{1}{2}(u_{yij} + u_{yij-1})$
u_{ye}	$u_{ye} = \frac{1}{2}(u_{yij} + u_{yi+1j})$
u_{yw}	$u_{yw} = \frac{1}{2}(u_{yij} + u_{yi-1j})$

6.2.4   X-equation approximation

$$\Delta^2 \frac{u_{xij}^{n+1} - u_{xij}^{n}}{\Delta t} +$$

Table 6.6: **Convection flux. y-equation**

side	flux
east	$\frac{\Delta}{4}(u_{xij} + u_{xij+1})(u_{yij} + u_{yi+1j})$
west	$-\frac{\Delta}{4}(u_{xi-1j} + u_{xi-1j+1})(u_{yij} + u_{yi-1j})$
north	$\frac{\Delta}{4}(u_{yij} + u_{yij+1})^2$
south	$-\frac{\Delta}{4}(u_{yij} + u_{yij-1})^2$

$$\frac{\Delta}{4}(u_{xij} + u_{xi+1j})^2 - \frac{\Delta}{4}(u_{xij} + u_{xi-1j})^2 +$$

$$\frac{\Delta}{4}(u_{xij} + u_{xij+1})(u_{yij} + u_{yi+1j}) - \frac{\Delta}{4}(u_{xij} + u_{xij-1})(u_{yij-1} + u_{yi+1j-1})$$

$$+\left(p_{i+1j} - p_{ij}\right)\Delta = 0$$

6.2.5   Y-equation approximation

$$\Delta^2 \frac{u_{yij}^{n+1} - u_{yij}^n}{\Delta t} +$$

$$\frac{\Delta}{4}(u_{xij} + u_{xij+1})(u_{yij} + u_{yi+1j}) - \frac{\Delta}{4}(u_{xi-1j} + u_{xi-1j+1})(u_{yij} + u_{yi-1j}) +$$

$$\frac{\Delta}{4}(u_{yij} + u_{yij+1})^2 - \frac{\Delta}{4}(u_{yij} + u_{yij-1})^2 +$$

$$+\left(p_{ij+1} - p_{ij}\right)\Delta = 0$$

6.3   Explicit scheme

The next task is to specify the upper index in X and Y equations. If the index is n we get fully explicit scheme which is similar to that derived above for finite difference method

$$\Delta^2 \frac{u_{xij}^{n+1} - u_{xij}^n}{\Delta t} +$$

$$\frac{\Delta}{4}(u_{xij}^n + u_{xi+1j}^n)^2 - \frac{\Delta}{4}(u_{xij}^n + u_{xi-1j}^n)^2 +$$

$$\frac{\Delta}{4}(u_{xij}^n + u_{xij+1}^n)(u_{yij}^n + u_{yi+1j}^n) - \frac{\Delta}{4}(u_{xij}^n + u_{xij-1}^n)(u_{yij-1}^n + u_{yi+1j-1}^n)$$

$$+\left(p_{i+1j}^n - p_{ij}^n\right)\Delta = 0 \qquad\qquad (6.11)$$

$$\Delta^2 \frac{u_{yij}^{n+1} - u_{yij}^n}{\Delta t} +$$

$$\frac{\Delta}{4}(u_{yij}^n + u_{yi+1j}^n)(u_{xij}^n + u_{xij+1}^n) - \frac{\Delta}{4}(u_{yij}^n + u_{yi-1j}^n)(u_{xi-1j}^n + u_{xi-1j+1}^n) +$$

$$\frac{\Delta}{4}(u_{yij}^n + u_{yij+1}^n)^2 - \frac{\Delta}{4}(u_{yij}^n + u_{yij-1}^n)^2 +$$

$$+\left(p_{ij+1}^n - p_{ij}^n\right)\Delta = 0 \tag{6.12}$$

The Poisson equation for pressure is derived in the same manner as above for finite difference method. For that the equations (6.11) is differentiated on x, whereas the equation (6.12) is differentiated on y. Then both results are summed under assumptions that both u_{ij}^{n+1} and u_{ij}^n are divergence free:

$$\frac{\delta u_{xij}^{n+1}}{\delta x} + \frac{\delta u_{yij}^{n+1}}{\delta y} = 0, \frac{\delta u_{xij}^n}{\delta x} + \frac{\delta u_{yij}^n}{\delta y} = 0$$

This equation is coupled with equations (6.11) and (6.12). The explicit scheme has advantage that the solution at the time instant $n + 1$ is explicitly expressed through the solution at time instant n. The solution of linear algebraic equations which is the most laborious numerical procedure is necessary only for the solution of the Poisson equation. The momentum equations (6.11) and (6.12) are solved explicitly. Velocities u_{xij}^{n+1} and u_{yij}^{n+1} are computed then from simple algebraic formula (6.11) and (6.12). The big disadvantage of the explicit method is the limitation forced by the Courant Friedrich Levy criterion. The time step Δt should be very small to secure the numerical stability. This disadvantage can be overcome within the implicit schemes.

6.4   Implicit scheme

If the index is $n + 1$ we get implicit scheme

$$\Delta^2 \frac{u^{n+1}_{xij} - u^n_{xij}}{\Delta t} +$$

$$\frac{\Delta}{4}(u^{n+1}_{xij} + u^{n+1}_{xi+1j})^2 - \frac{\Delta}{4}(u^{n+1}_{xij} + u^{n+1}_{xi-1j})^2 +$$

$$\frac{\Delta}{4}(u^{n+1}_{xij} + u^{n+1}_{xij+1})(u^{n+1}_{yij} + u^{n+1}_{yi+1j}) - \frac{\Delta}{4}(u^{n+1}_{xij} + u^{n+1}_{xij-1})(u^{n+1}_{yij-1} + u^{n+1}_{yi+1j-1})$$

$$+ \left(p^{n+1}_{i+1j} - p^{n+1}_{ij} \right)\Delta = 0 \qquad (6.13)$$

$$\Delta^2 \frac{u^{n+1}_{yij} - u^n_{yij}}{\Delta t} +$$

$$\frac{\Delta}{4}(u^{n+1}_{yij} + u^{n+1}_{yi+1j})(u^{n+1}_{xij} + u^{n+1}_{xij+1}) - \frac{\Delta}{4}(u^{n+1}_{yij} + u^{n+1}_{yi-1j})(u^{n+1}_{xi-1j} + u^{n+1}_{xi-1j+1}) +$$

$$\frac{\Delta}{4}(u^{n+1}_{yij} + u^{n+1}_{yij+1})^2 - \frac{\Delta}{4}(u^{n+1}_{yij} + u^{n+1}_{yij-1})^2 +$$

$$+ \left(p^{n+1}_{ij+1} - p^{n+1}_{ij} \right)\Delta = 0 \qquad (6.14)$$

The Poisson equation for pressure is derived in the same manner as above for finite difference method. For that the equations (6.13) is differentiated on x, whereas the equation (6.14) is differentiated on y. Then both results are summed under assumptions that both u^{n+1}_{ij} and u^n_{ij} are divergence free:

$$\frac{\delta u^{n+1}_{xij}}{\delta x} + \frac{\delta u^{n+1}_{yij}}{\delta y} = 0, \frac{\delta u^n_{xij}}{\delta x} + \frac{\delta u^n_{yij}}{\delta y} = 0$$

The resulting Poisson equation can not be solved because both the r.h.s. (velocities) and the l.h.s (pressure) depend on $n + 1$. The term on r.h.s. cannot be computed until the computation of velocity field at time $n + 1$ is completed and vice versa. Other problem is that the equations (6.13) and (6.14) are non linear.

6.5   Iterative procedure for implicit scheme

To solve the nonlinear system and the whole system of equations we use the iterative procedure. Let m be an iteration number. The nonlinear term is represented in form:

$$\frac{\partial u_i u_j}{\partial x_j} = \frac{\partial u^{(m)}_i u^{(m-1)}_j}{\partial x_j} \qquad (6.15)$$

The velocity u_j is taken from the previous iteration $(m-1)$. The system (6.11) and (6.12) is rewritten in the form

$$\Delta^2 \frac{u_{xij}^{(m)} - u_{xij}^n}{\Delta t} +$$

$$\frac{\Delta}{4}(u_{xij}^{(m)} + u_{xi+1j}^{(m)})(u_{xij}^{(m-1)} + u_{xi+1j}^{(m-1)}) - \frac{\Delta}{4}(u_{xij}^{(m)} + u_{xi-1j}^{(m)})(u_{xij}^{(m-1)} + u_{xi-1j}^{(m-1)}) +$$

$$\frac{\Delta}{4}(u_{xij}^{(m)} + u_{xij+1}^{(m)})(u_{yij}^{(m-1)} + u_{yi+1j}^{(m-1)}) - \frac{\Delta}{4}(u_{xij}^{(m)} + u_{xij-1}^{(m)})(u_{yij-1}^{(m-1)} + u_{yi+1j-1}^{(m-1)})$$

$$+\left(p_{i+1j}^{(m)} - p_{ij}^{(m)}\right)\Delta = 0$$

$$\Delta^2 \frac{u_{yij}^{(m)} - u_{yij}^n}{\Delta t} +$$

$$\frac{\Delta}{4}(u_{yij}^{(m)} + u_{yi+1j}^{(m)})(u_{xij}^{(m-1)} + u_{xij+1}^{(m-1)}) - \frac{\Delta}{4}(u_{yij}^{(m)} + u_{yi-1j}^{(m)})(u_{xi-1j}^{(m-1)} + u_{xi-1j+1}^{(m-1)}) +$$

$$\frac{\Delta}{4}(u_{yij}^{(m)} + u_{yij+1}^{(m)})(u_{yij}^{(m-1)} + u_{yij+1}^{(m-1)}) - \frac{\Delta}{4}(u_{yij}^{(m)} + u_{yij-1}^{(m)})(u_{yij}^{(m-1)} + u_{yij-1}^{(m-1)}) +$$

$$+\left(p_{ij+1}^{(m)} - p_{ij}^{(m)}\right)\Delta = 0$$

or

$$q_{xi-1j}u_{xi-1j}^{(m)} + q_{xij}u_{xij}^{(m)} + q_{xi+1j}u_{xi+1j}^{(m)} + q_{xij-1}u_{xij-1}^{(m)} + q_{xij+1}u_{xij+1}^{(m)} + \quad (6.16)$$

$$+\left(p_{i+1j}^{(m)} - p_{ij}^{(m)}\right)\Delta = r_{xij}$$

$$q_{yi-1j}u_{yi-1j}^{(m)} + q_{yij}u_{yij}^{(m)} + q_{yi+1j}u_{yi+1j}^{(m)} + q_{yij-1}u_{yij-1}^{(m)} + q_{yij+1}u_{yij+1}^{(m)} + \quad (6.17)$$

$$+\left(p_{ij+1}^{(m)} - p_{ij}^{(m)}\right)\Delta = r_{yij}$$

where

$$q_{xij} = \Delta^2/\Delta t + \frac{\Delta}{4}[(u_{xij}^{(m-1)} + u_{xi+1j}^{(m-1)}) - (u_{xij}^{(m-1)} + u_{xi-1j}^{(m-1)}) +$$

$$+ (u_{yij}^{(m-1)} + u_{yi+1j}^{(m-1)}) - (u_{yij-1}^{(m-1)} + u_{yi+1j-1}^{(m-1)})]$$

$$q_{xi+1j} = \frac{\Delta}{4}(u_{xij}^{(m-1)} + u_{xi+1j}^{(m-1)}), q_{xi-1j} = -\frac{\Delta}{4}(u_{xi-1j}^{(m-1)} + u_{xij}^{(m-1)}),$$

$$q_{xij+1} = \frac{\Delta}{4}(u_{yij}^{(m-1)} + u_{yi+1j}^{(m-1)}), q_{xij-1} = -\frac{\Delta}{4}(u_{yij-1}^{(m-1)} + u_{yi+1j-1}^{(m-1)})$$

$$q_{yij} = \frac{\Delta^2}{\Delta t} + \frac{\Delta}{4}\big[(u_{yij}^{(m-1)} + u_{yij+1}^{(m-1)}) - (u_{yij}^{(m-1)} + u_{yij-1}^{(m-1)}) +$$

$$+ (u_{xij}^{(m-1)} + u_{xij+1}^{(m-1)}) - (u_{xi-1j}^{(m-1)} + u_{xi-1j+1}^{(m-1)})\big]$$

$$q_{yi-1j} = -\frac{\Delta}{4}(u_{xi-1j}^{(m-1)} + u_{xi-1j+1}^{(m-1)}), \quad q_{yi+1j} = \frac{\Delta}{4}(u_{xij}^{(m-1)} + u_{xij+1}^{(m-1)})$$

$$q_{yij-1} = -\frac{\Delta}{4}(u_{yij}^{(m-1)} + u_{yij-1}^{(m-1)}), \quad q_{yij+1} = \frac{\Delta}{4}(u_{yij}^{(m-1)} + u_{yij+1}^{(m-1)})$$

$$r_{xij} = \Delta^2 \frac{u_{xij}^n}{\Delta t}, r_{yij} = \Delta^2 \frac{u_{yij}^n}{\Delta t}$$

Dividing the equations (6.16) by q_{xij} and (6.17) by q_{yij} we obtain

$$a_{xi-1j}u^{(m)}_{xi-1j} + u^{(m)}_{xij} + a_{xi+1j}u^{(m)}_{xi+1j} + a_{xij-1}u^{(m)}_{xij-1} + a_{xij+1}u^{(m)}_{xij+1}+ \quad (6.18)$$

$$+\left(p^{(m)}_{i+1j} - p^{(m)}_{ij} \right)\Delta/q_{xij} = R_{xij}$$

$$a_{yi-1j}u^{(m)}_{yi-1j} + u^{(m)}_{yij} + a_{yi+1j}u^{(m)}_{yi+1j} + a_{yij-1}u^{(m)}_{yij-1} + a_{yij+1}u^{(m)}_{yij+1}+ \quad (6.19)$$

$$+\left(p^{(m)}_{ij+1} - p^{(m)}_{ij} \right)\Delta/q_{yij} = R_{yij}$$

where $a_{x,ykl} = q_{x,ykl}/q_{x,yij}$ and $R_{x,ykl} = r_{x,ykl}/q_{x,yij}$. In what follows we use the operator form of equations (6.18) and (6.19):

$$u = Au + Bp + C \qquad (6.20)$$

6.6 Pressure correction method

The velocity field satisfying the equation (6.20) is the solution of the linearized Navier Stokes equation. It doesn't fulfill the continuity equation. The iterative solution satisfying the whole system of equations is computed using the pressure correction method.

The iterative scheme consists of following steps. First, the intermediate solution is calculated with pressure taken from the previous iteration:

$$u^* = Au^* + Bp^{(m-1)} + C \qquad (6.21)$$

The velocity and pressure corrections

$$u^{(m)} = u^* + u', \quad p^{(m)} = p^{(m-1)} + p' \qquad (6.22)$$

are computed within next steps. Substitution of (6.22) into (6.20) gives

$$(u^* + u') = A(u^* + u') + B(p^{(m-1)} + p') + C \qquad (6.23)$$

Since u^* satisfies the equation (6.21) the equation for the velocity correction reads

$$u' = Au' + Bp' \qquad (6.24)$$

The velocity at the iteration (m) is

$$u^{(m)} = u^* + Au' + Bp' \qquad (6.25)$$

It should satisfy the continuity equation

$$\nabla u^{(m+1)} = 0 \qquad (6.26)$$

what results in

$$\nabla u^* = -\nabla B p' - \nabla A u' \qquad (6.27)$$

6.7 SIMPLE method

A very popular pressure correction method is the SIMPLE method. The main assumption of this method is neglect of the term $\nabla A u'$ in (6.27) and (6.24):

$$\nabla B p' = -\nabla u^* \qquad (6.28)$$
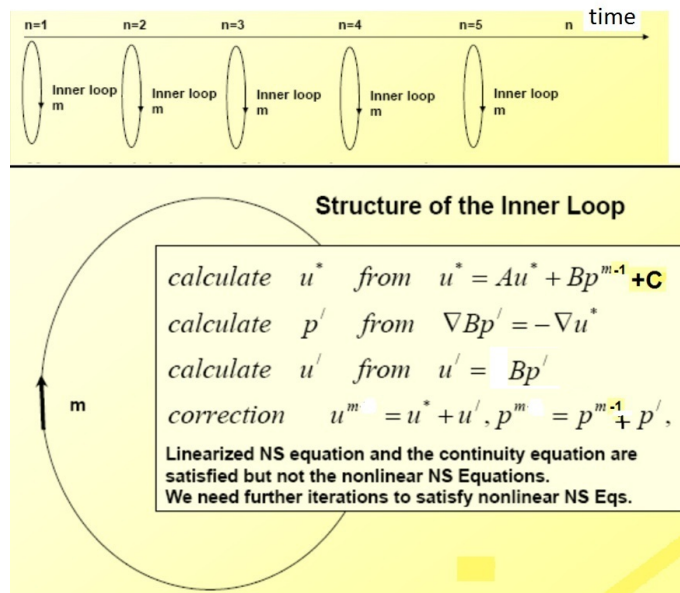
Figure 6.2: SIMPLE algorithm.

The equation (6.28) is the Poisson equation for the pressure correction p'.

The solution algorithm is summarized in Fig. 6.2. Let the solution is known at time slice n, the solution at the next time instant $n+1$ is seeking. In the first iteration all quantities are taken from the previous time instant

$$u_{x,yij}^{(m=1)} = u_{x,yij}^n, \; p_{ij}^{(m=1)} = p_{ij}^n$$

At each time instant the inner loop iterations are performed until residuals are getting smaller than some threshold

$$max|u_{x,yij}^{(m)} - u_{x,yij}^{(m-1)}| < \varepsilon_u, \qquad max|p_{ij}^{m(m)} - p_{ij}^{(m-1)}| < \varepsilon_p$$

As soon as the inner loop iterations are converged the solution at time instant $n+1$ is equaling to the solution from the last iteration and the next time instant is computed. The structure of the inner loop is shown in Fig. 6.2.

6.7.1   Pressure correction equation

Let us consider the pressure correction equation (6.28) in details. This equation is solved for the control volume shown in Fig. 6.3. The divergency operator $\nabla \mathbf{f} = \frac{\partial f_x}{\partial x} + \frac{\partial f_y}{\partial y}$ is represented within Finite Volume Method as follows

$$\int_U \nabla \mathbf{f} dU = \int_U (\frac{\partial f_x}{\partial x} + \frac{\partial f_y}{\partial y}) dU = \int_S \mathbf{f} \mathbf{n} dS = (f_{xe} - f_{xw} + f_{yn} - f_{ys})\Delta \quad (6.29)$$

Therefore, the right hand side of the equation (6.28) takes the form

$$\int_U \nabla \mathbf{u}^* dU = \int_S \mathbf{u}^* \mathbf{n} dS = (u^*_{xij} - u^*_{xi-1j} + u^*_{yij} - u^*_{yij-1})\Delta \quad (6.30)$$

As follows from (6.18) and (6.19) the operator Bp' has the following values at faces of the control volume

$$(Bp')_{xij} = \left(p'_{i+1j} - p'_{ij} \right)\Delta/q_{xij}, (Bp')_{xi-1j} = \left(p'_{ij} - p'_{i-1j} \right)\Delta/q_{xi-1j}$$

$$(Bp')_{yij} = \left(p'_{ij+1} - p'_{ij} \right)\Delta/q_{yij}, (Bp')_{yij-1} = \left(p'_{ij} - p'_{ij-1} \right)\Delta/q_{yij-1}.$$

$$(6.31)$$

Substitution of (6.30) and (6.31) into (6.28) results in

$$
\left(p'_{i+1j} - p'_{ij}\right)/q_{xij} - \left(p'_{ij} - p'_{i-1j}\right)/q_{xi-1j} + \left(p'_{ij+1} - p'_{ij}\right)/q_{yij}
$$

$$
-\left(p'_{ij} - p'_{ij-1}\right)/q_{yij-1} = -(u^*_{xij} - u^*_{xi-1j} + u^*_{yij} - u^*_{yij-1}) \qquad (6.32)
$$

or

$$
\beta_{i+1j}\, p'_{i+1j} + \beta_{ij}\, p'_{ij} + \beta_{i-1j}\, p'_{i-1j} + \beta_{ij+1}\, p'_{ij+1} + \beta_{ij-1}\, p'_{ij-1} = c_{ij} \quad (6.33)
$$

where

$$
c_{ij} = -(u^*_{xij} - u^*_{xi-1j} + u^*_{yij} - u^*_{yij-1}),\; \beta_{ij} = -\left(\frac{1}{q_{xij}} + \frac{1}{q_{xi-1j}} + \frac{1}{q_{yij}} + \frac{1}{q_{yij-1}}\right),
$$

$$
\beta_{i+1j} = \frac{1}{q_{xij}},\; \beta_{i-1j} = \frac{1}{q_{xi-1j}},\; \beta_{ij+1} = \frac{1}{q_{yij}},\; \beta_{ij-1} = \frac{1}{q_{yij-1}}.
$$

6.7.2　Summary of the SIMPLE algorithm

We introduce one dimensional numbering instead of two dimensional one according to the rule

$$
\alpha = (i-1)N_y + j
$$

Let the solution at the time instant n be known. The task is to find the solution at the time $n + 1$. At each time instant the guess solution is taken from the previous time instant:

$$
u^{(1)}_{x,y\alpha} = u^n_{x,y\alpha},\; p^{(1)}_{\alpha} = p^n_{\alpha}
$$

The solution is found within the next substeps:

i) Calculation of the auxiliary velocity $u^*_{x,y\alpha}$ from two independent systems of linear algebraic equations:

$$
a_{x\alpha-N_y} u^*_{x\alpha-N_y} + u^*_{x\alpha} + a_{x\alpha+N_y} u^*_{x\alpha+N_y} + a_{x\alpha-1} u^*_{x\alpha-1} + a_{x\alpha+1} u^*_{x\alpha+1} +
$$

$$
+\left(p^{(m-1)}_{\alpha+N_y} - p^{(m-1)}_{\alpha}\right)\Delta/q_{x\alpha} = R_{x\alpha}
$$

$$a_{y\alpha-N_y}u^*_{y\alpha-N_y} + u^*_{y\alpha} + a_{y\alpha+N_y}u^*_{y\alpha+N_y} + a_{y\alpha-1}u^*_{y\alpha-1} + a_{y\alpha+1}u^*_{y\alpha+1} +$$

$$+\left(p^{(m-1)}_{\alpha+1} - p^{(m-1)}_{\alpha}\right)\Delta/q_{y\alpha} = R_{y\alpha}$$

ii) Calculation of the pressure correction p'_α from the system of linear algebraic equations:

$$\beta_{\alpha+N_y}p'_{\alpha+N_y} + \beta_\alpha p'_\alpha + \beta_{\alpha-N_y}p'_{\alpha-N_y} + \beta_{\alpha+1}p'_{\alpha+1} + \beta_{\alpha-1}p'_{\alpha-1} = c_\alpha$$

iii) Calculation of the velocity correction $u'_{x,y\alpha}$:

$$u'_{x\alpha} = -\left(p'_{\alpha+N_y} - p'_\alpha\right)\Delta/q_{x\alpha}$$

$$u'_{y\alpha} = -\left(p'_{\alpha+1} - p'_\alpha\right)\Delta/q_{y\alpha}$$

iv) Correction of the velocity and pressure:

$$u^{(m)}_{x,y\alpha} = u^*_{x,y\alpha} + u'_{x,y\alpha}, \quad p^{(m)}_\alpha = p^{(m-1)}_\alpha + p'_\alpha$$

Figure 6.3: Control volume used for the pressure correction equation.

v) Check the difference between two iterations:

$$max|u_{x,y\alpha}^{(m)} - u_{x,y\alpha}^{(m-1)}| < \varepsilon_u, \qquad max|p_\alpha^{(m)} - p_\alpha^{(m-1)}| < \varepsilon_p$$

If these conditions are not fulfilled then

$$u_{x,y\alpha}^{(m-1)} = u_{x,y\alpha}^{(m)}, p_\alpha^{(m-1)} = p_\alpha^{(m)}$$

and go to the step i). Otherwise the calculation at the time moment $n+1$ is completed

$$u_{x,y\alpha}^{n+1} = u_{x,y\alpha}^{(m)}, p_\alpha^{n+1} = p_\alpha^{(m)}$$

and one proceeds to the next time instant $n+2$.

Chapter 7

Overview of pressure correction methods

7.1   SIMPLE algorithm

The linearized Navier Stokes equation written in operator form is

$$u = Au + Bp + C \tag{7.1}$$

Within the SIMPLE algorithm the solution is seeking at each time step in form of the loop:

- Calculation of the auxiliary velocity

$$u^* = Au^* + Bp^{(m-1)} + C \tag{7.2}$$

- Calculation of the pressure correction

$$\nabla Bp' = -\nabla u^* \tag{7.3}$$

- Calculation of the velocity correction

$$u' = Bp' \tag{7.4}$$

- Correction
$$u^{(m)} = u^* + u', \, p^{(m)} = p^{(m-1)} + p' \tag{7.5}$$

7.2   PISO algorithm

In the SIMPLE algorithm we neglected the term $\nabla Au'$ (see 6.25). In PISO algorithm this term is taken into account. Actually the term $\nabla Au'$ can not be calculated before the velocity correction is computed. Therefore, the term is taken into account in an iterative way.

7.2.1   First iteration

The term Au' is neglected, i.e. $Au' = 0$. The pressure correction is found from the Poisson equation

$$\nabla Bp' = -\nabla u^* \tag{7.6}$$

The velocity correction is then

$$u' = Bp' \qquad (7.7)$$

7.2.2   Second iteration

The pressure correction within the second iteration is found from the Poisson equation

$$\nabla Bp'' = -\nabla Au' \qquad (7.8)$$

The velocity correction within the second iteration is then

$$u'' = Au' + Bp'' \qquad (7.9)$$

7.2.3   Correction

Corrected velocities and pressure are

$$u^{(m)} = u^* + u' + u'', \, p^{(m)} = p^{(m-1)} + p' + p'' \qquad (7.10)$$

Using formula derived above

$$\nabla Bp' = -\nabla u^*, u' = Bp', u'' = Au' + Bp'', \nabla Bp'' = -\nabla Au'$$

it is easy to prove that the velocity $u^{(m)}$ satisfies the continuity equation. Now we prove the equation $u^{(m)} = Au^{(m)} + Bp^{(m)} + C$:

$$u^* + u' + u'' = A(u^* + u' + u'') + B(p^{(m-1)} + p' + p'') + C \qquad (7.11)$$

Since

$$u^* = Au^* + Bp^{(m-1)} + C, u' = Bp', u'' = Au' + Bp''$$

the equation (7.11) is not satisfied. The residual is Au''. The residual can be reduced within next iterations. However, usually, PISO algorithm uses only two iterations.

7.2.4   Summary

The PISO algorithm can be summarized as follows:

- Calculation of the auxiliary velocity

$$u^* = Au^* + Bp^{(m-1)} + C \qquad (7.12)$$

- Calculation of the pressure correction p':

$$\nabla B p' = -\nabla u^* \qquad (7.13)$$

- Calculation of the velocity correction u'

$$u' = B p' \qquad (7.14)$$

- Calculation of the pressure correction p'':

$$\nabla B p'' = -\nabla A u' \qquad (7.15)$$

- Calculation of the velocity correction u''

$$u'' = A u' + B p'' \qquad (7.16)$$

- Correction

$$u^{(m)} = u^* + u' + u'', \, p^{(m)} = p^{(m-1)} + p' + p'' \qquad (7.17)$$

Both algorithms PISO and SIMPLE are widely used in CFD codes.

7.3   SIMPLEC algorithm

Another way to hold the term $\nabla A u'$ (see 6.25) is implemented in the SIMPLEC algorithm. The velocity correction at $\alpha - th$ control volume u'_α can be calculated using the interpolation over N adjacent control volumes:

$$\sum_{\beta=1}^{N} A_\beta u'_\beta \approx u'_\alpha \sum_{\beta=1}^{N} A_\beta \tag{7.18}$$

where β is the number of adjacent control volumes around the control volume with the number α.

$$u'_\alpha \approx \frac{\sum_{\beta=1}^{N} A_\beta u'_\beta}{\sum_{\beta=1}^{N} A_\beta} \tag{7.19}$$

The equation for the velocity correction is

$$u' = A u' + B p' \tag{7.20}$$

or

$$u'_\alpha = \sum_{\beta=1}^{N} A_\beta u'_\beta + B p' \tag{7.21}$$

Substitution of (7.19) into (7.21) yields

$$u'_\alpha = u'_\alpha \sum_{\beta=1}^{N} A_\beta + B p' \tag{7.22}$$

and

$$u'_\alpha = \frac{B p'}{1 - \sum_{\beta=1}^{N} A_\beta} \tag{7.23}$$

The pressure correction equation

$$\nabla B p' = -\nabla u^* - \nabla A u'$$

takes the form

$$\nabla B p' = -\nabla u^* - \nabla A \frac{B p'}{1 - \sum_{\beta=1}^{N} A_\beta}$$

or

$$\nabla \left(B + A \frac{B}{1 - \sum_{\beta=1}^{N} A_\beta} \right) p' = -\nabla u^* \tag{7.24}$$

The computational steps are the same as these in SIMPLE algorithm with only difference that the equation (7.24) is solved instead of (7.3).

Chapter 8
Computational grids

8.1 Grid types

The computational grids are subdivided into:

- structured grids (see Fig. 8.1a),

- block structured grids (see Fig. 8.1b),

- unstructured grids (see Fig. 8.1c).

Disadvantage of the structured grid is shown in Fig. 8.2. Refinement of the grid close to the wall results in the refinement in areas where this refinement is not necessary. This disadvantage can be overcome by use of block-structured (Fig. 8.1b) and unstructured grid (Fig. 8.1c).
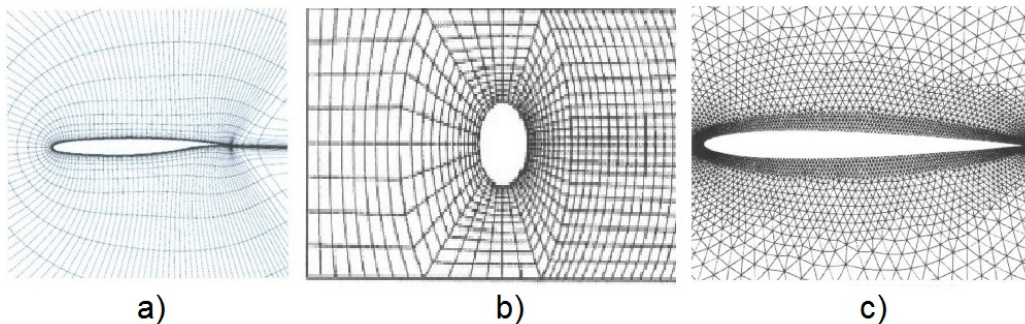
Figure 8.1: Samples of a) structured grid for an airfoil, b) block structured grid for cylinder in channel and c) unstructured grid for an airfoil.

The quality of the grid has a strong impact on the accuracy of numerical prediction. The change of the cell topology within the computational domain
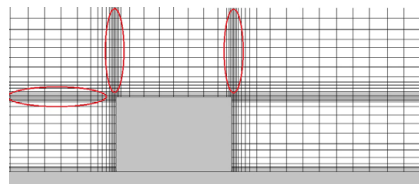
Figure 8.2: Illustration of structured grid disadvantage.

should be smooth especially at the border between different grid blocks. The grid resolution should be high especially in areas of boundary layers and close to the free surface. For this sake the special refinement is used in these areas. To increase the accuracy of the computations in boundary layers one uses special grid boundary layers close to walls.

8.2   Overset or Chimera grids

For complicated objects one uses overset or Chimera grids. The idea of chimera or overset grids is to generate the grids separately around each geometrical entity in the computational domain. After that the grids are combined together in such a way that they overlap each other where they meet. The crucial operation is an accurate transfer of quantities between the different grids at the overlapping region. The most important advantage of the overset or Chimera grid is the possibility to generate high quality structured particular grids separately for different body elements completely independent of each other, without having to take care of the interface between grids.

8.3   Morphing grids

Very efficient way of CFD body simulation is the use of moving or morphing grids [6]. The idea is the computational grid is moved in accordance with the displacement of the body by using an analytical weighted regridding which is a type of extrapolation of rigid transformation. The possible problem of morphing grid is poor quality caused by its motion. Consequently if the mesh surrounding the body is allowed to deform the elements around the body deform. This can quickly lead to poor quality elements if care is not taken. An alternative method is to replicate the motion of the body with the fluid domain split into an inner and outer region. The outer domain remains fixed in space while the inner domain containing the body moves laterally to replicate the motion. The mesh in the inner sub domain remains locked in position relative to the lateral motion of the body. This prevents deformation of the detailed mesh around the body. The outer mesh is deformed due to the motion of the inner region.

If moving grids are used the Navier Stokes should be transformed to take the velocity of grid faces $\vec{U}_g$ into account,

$$\frac{\partial \vec{u}}{\partial t} + \left\{ \left(\vec{u} - \vec{U}_g \right) \nabla \right\} \vec{u} = \vec{f} - \frac{1}{\rho} \nabla p + \nu \Delta \vec{u} \tag{8.1}$$

Thomas and Lombard have shown that the function $\vec{U}_g$ can not be arbitrary rather than they have to be found from the Geometric Conservation Law

$$\frac{\partial}{\partial t} \int\limits_U dU - \int\limits_S \vec{U}_g \vec{n} dS = 0 \tag{8.2}$$

Where U and S are respectively volume and surface of cells. The equation (8.2) is derived from the condition that the computation of the control volumes or of the grid velocities must be performed in a such a way that the resulting numerical scheme preserves the state of the uniform flow, independently of the deformation of the grid. The equation (8.2) is satisfied automatically if the control volumes don't change their shape. The Geometric conservation law (8.2) should solve coupled with other fluid flow equations using the same discretizations schemes.

More detailed information about grid generation can be found in [3], [7] and [8].

Part II

Mathematical modelling of turbulent flows

Chapter 9

Physics of turbulence

9.1　Definition of the turbulence

Flow motions are subdivided into laminar flows and turbulent ones. The word " Laminar" in Greek means layer. The fluid particles move orderly in layers without intense lateral mixing. The disruption between layers is absent. On the contrary the turbulent flow is very chaotic with strong eddies and intense mixing across the flow.
Turbulent motion is the three dimensional unsteady flow motion with

- chaotical trajectories of fluid particles,

- fluctuations of the velocity and

- strong mixing

arisen at large Re numbers due to unstable vortex dynamics.

9.2　Vortex dynamics

The vortex dynamics is the key to understand what happens in the turbulent flow.

9.2.1　Vorticity transport equation

The vector calculus relation reads:

$$\frac{1}{2}\nabla(\mathbf{A} \cdot \mathbf{A}) = \mathbf{A} \times (\nabla \times \mathbf{A}) + (\mathbf{A}\nabla)\mathbf{A} \qquad (9.1)$$

Taking $\mathbf{u} = \mathbf{A}$ we get:

$$\frac{1}{2}\nabla(\mathbf{u} \cdot \mathbf{u}) = \mathbf{u} \times \omega + (\mathbf{u}\nabla)\mathbf{u} \qquad (9.2)$$

where $\omega = \nabla \times \mathbf{u}$ is the vorticity.
Application of the curl operator to (9.2) results in

$$\nabla \times ((\mathbf{u}\nabla)\mathbf{u}) = -\nabla \times (\mathbf{u} \times \omega) = -\mathbf{u}(\nabla\omega) + \omega(\nabla\mathbf{u}) - (\omega\nabla)\mathbf{u} + (\mathbf{u}\nabla)\omega \quad (9.3)$$

Here we used the identity $\nabla \times (\frac{1}{2}\nabla(\mathbf{u} \cdot \mathbf{u})) = 0$.

Both vectors $\mathbf{u}$ and ω satisfy the continuity equation, i.e. $\nabla\omega = 0$ and $\nabla\mathbf{u} = \mathbf{0}$:

$$\nabla \times ((\mathbf{u}\nabla)\mathbf{u}) = -(\omega\nabla)\mathbf{u} + (\mathbf{u}\nabla)\omega \tag{9.4}$$

Let us apply the curl operator to the Navier Stokes equation

$$\nabla \times (\frac{\partial \mathbf{u}}{\partial t} + (\mathbf{u}\nabla)\mathbf{u}) = \nabla \times (-\frac{1}{\rho}\nabla p + \nu\Delta\mathbf{u}) \tag{9.5}$$

$$\frac{\partial \omega}{\partial t} + \nabla \times ((\mathbf{u}\nabla)\mathbf{u}) = \nu\Delta(\nabla \times \mathbf{u}) = \nu\Delta\omega \tag{9.6}$$

Substituting (9.4) into (9.6) results in

$$\frac{\partial \omega}{\partial t} + (\mathbf{u}\nabla)\omega = (\omega\nabla)\mathbf{u} + \nu\Delta\omega \tag{9.7}$$

$$\frac{D\omega}{Dt} = (\omega\nabla)\mathbf{u} + \nu\Delta\omega \tag{9.8}$$

The equation (9.8) is the vorticity transport equation.

9.2.2   Vorticity and vortices

The vortices are main players in turbulent flows. Here we would like to emphasize the difference between the vorticity and vortices. The vorticity is the curl of the velocity $\omega = \nabla \times \mathbf{u}$. The vorticity is usually not zero in viscous flows especially in areas close to the walls. Speaking about vortices we bear in mind the concentrated structures of the vorticity field $\omega = \nabla \times \mathbf{u}$. The difference between the vorticity and vortices is illustrated in Fig. 9.1. The boundary layer is the flow area with strong but smoothly distributed vorticity (Fig. 9.1a). Due to instabilities, that will be discussed later, the concentrated vortex structures arise in the smooth vorticity field (Fig. 9.1b).

A famous sample of concentrated vortex structures is the tornado (Fig. 9.2).

The vorticity is solenoidal:

$$\nabla \omega = \nabla(\nabla \times \mathbf{u}) = 0 \qquad (9.9)$$

The consequence of the condition (9.9) is:

- All vortex lines, defined as the lines which are tangential to the vorticity vector $\omega \times d\mathbf{l} = 0$, are closed in the three dimensional case (Fig. 9.3).

The velocity induced by vorticity ω occupied the volume U are calculated from the Biot-Savart law:

$$\mathbf{u}(\mathbf{x}, t) = \frac{1}{4\pi} \int_U \frac{\omega \times (\mathbf{x} - \mathbf{r})}{|\mathbf{x} - \mathbf{r}|^3} \; dU \qquad (9.10)$$

The velocities induced by two dimensional and three dimensional vortex structures are shown in Fig. 9.4. An important fact is the appearance of self induced velocities on curvilinear three dimensional vortex structures. They are responsible for leapfrog vortex ring motion (http://www.lemos.uni-rostock.de/galerie/). The self induced velocities is the reason for convective instability of three dimensional vortex structures.
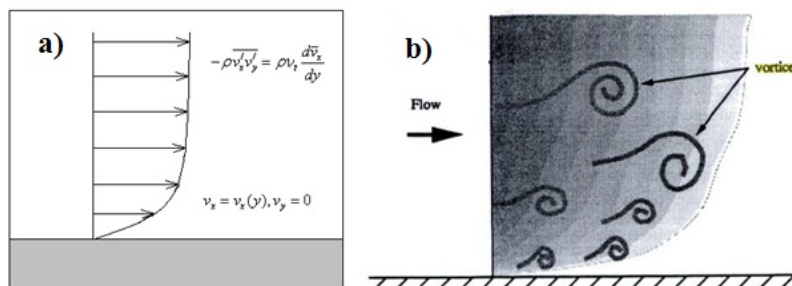
Figure 9.1: Vorticity and vortices.

9.2.3   Vortex amplification as an important mechanism of the turbulence generation

As mentioned above the vortices are main players during the laminar- turbulent transition. The vorticity can be essentially intensified (amplified) due to action of neighboring vortices or even due to self induction.

Figure 9.2: Tornado.
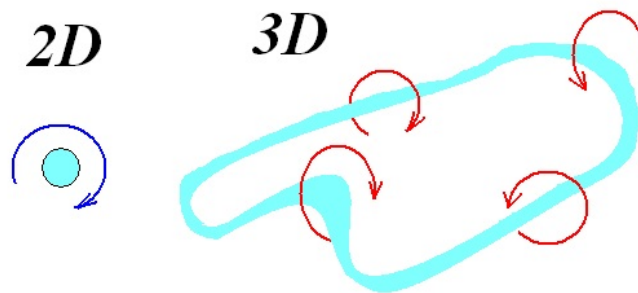
Figure 9.3: Vortices in two-dimensional and three dimensional cases.

The reason for that can be explained by analysis of the vorticity transport equation

$$\frac{D\omega}{Dt} = (\omega\nabla)\mathbf{u} + \nu\Delta\omega \qquad (9.11)$$

The r.h.s. of (9.11) contains two terms. The first term $(\omega\nabla)\mathbf{u}$ is responsible for the rotation of the vorticity vector ω and enlargement or reduction of its magnitude $|\omega|$. The second diffusion term results in spreading of the vorticity in the space. The term $(\omega\nabla)\mathbf{u}$ is responsible for the amplification of the vorticity.

The effect of the amplification can easily be understood if we consider the vortex with vector aligned along the x-axis $\omega_x > 0$. If such a vortex is in the fluid stretching area $\frac{\partial u_x}{\partial x} > 0$, the term $\omega_x \frac{\partial u_x}{\partial x} > 0$ is positive. As a result, $\frac{D\omega_x}{Dt} > 0$ is positive, what leads to the increase of the vorticity ω_x. As shown analytically by Novikov [9] for a simple model problem, the vortex strength
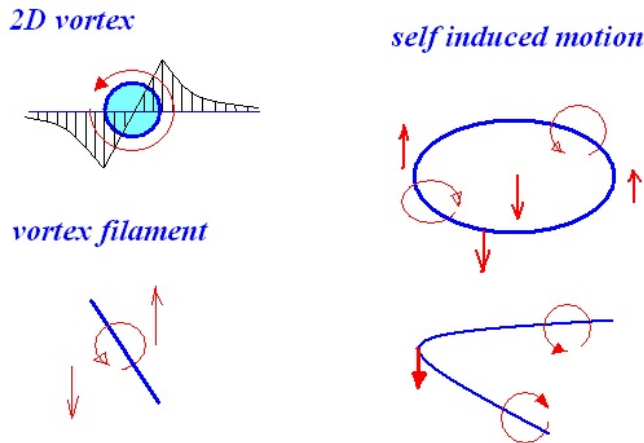
Figure 9.4: Velocities induced by vortices. Three dimensional curvilinear vortices induce self induced velocities.

of vortons structures can increase exponentially up to the infinity without viscosity effects. The vorticity growth caused by inviscid amplification term is counterbalanced by the diffusion term. Two terms on r.h.s. of (9.11) compete with each other. In the inviscid fluid the circulation of the vortex core is constant $\Gamma = \int_S \omega_x dS = const$. Increase of ω_x results in the decrease of the cross section S. The vortex becomes thinner. The diffusion acts against and makes the vortex thicker. In some flow regions the amplification can be stronger that diffusion. The thin vortex losses the stability and is folded.

As shown by Chorin [10] and [11] the folding is necessary mechanism preventing the exponential growth of vorticity. If the amplification is too strong, the vorticity goes to infinity and the energy is not kept constant. Chorin [10] notes that "as the vortices stretch, their cross-section decreases and the energy associated with them would increase unless they arranged themselves in such a way that their velocity canceled. The foldings achieves such cancelation". This could be easily explained using a simple sample. If we have just one straight infinite vortex it induces the velocity in the plane perpendicular to its axis. If this vortex is tangled the vortex pieces with different vorticity direction are approaching close each to other canceling their induction (see Fig. 9.5).

Chorin [11] explicitly specifies typical scales of folding: " the inertial range [1] properties are due to the appearance of folded vortex tubes, which behave on large scales as self-avoiding walks, and on small scales contain a large num-
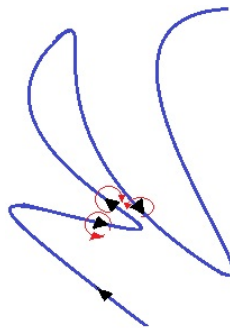
Figure 9.5: Illustration of the vortex folding.

ber of folds (=hairpins) that are needed to satisfy the constraint of energy conservation".

Summarizing all effects mentioned above one can imagine the following scenario (see Fig. 9.6). Let the vorticity at a certain point of the flow grows. In the real physical process folding prevents the growth of the kinetic energy and increases the canceling effect of viscosity. Then the vortex structures breaks down into small structures due to reconnection mechanism described in the next subsection.

---

[1] this term will be introduced in the next chapter
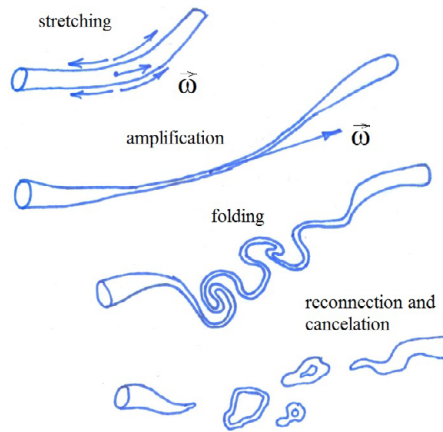
Figure 9.6: Scenario of vortex amplification.

9.2.4　Vortex reconnection

Let us consider the vortex ring (see Fig. 9.7). Due to convective instability or influence of neighboring vortices the vortex ring is deformed. Due to self
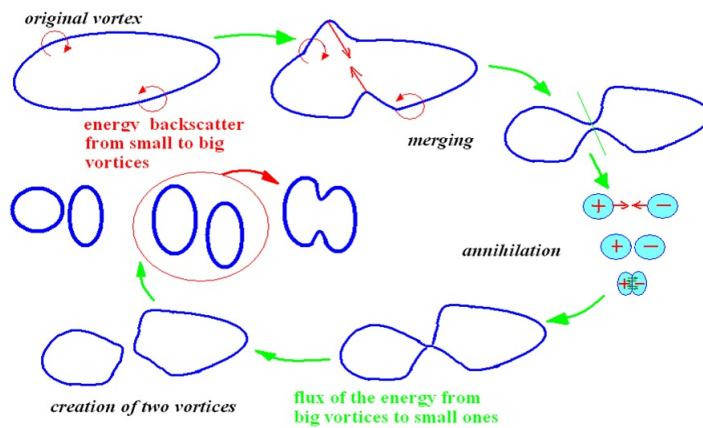
Figure 9.7: Scenario of vortex reconnection.

induction two opposite sides of the ring are merged. As soon as two elements with opposite vorticity sign are approaching each to other, they start to cancel each other by mutual diffusion. The vortices disappear in the area of the contact. Two small vortices are created from one big vortex. Each small vortex ring breaks then down into smaller vortices and so on. The energy of small vortices is equal to the energy of the big vortex with a small loss caused by the dissipation. This fact is formulated in the sentence, which is common in the turbulence theory: The energy is transferred from large scale vortices to small scales vortices. The reconnection process can be observed on macroscales. The decay, break up of tip vortices behind the airplane proceeds according to the same scenario (see Fig. 9.8). The reconnection process is, perhaps, the main mechanism of vortex cascade in the turbulent flows, i.e. transformation of big vortices into small ones. The reconnection can also lead to enlargement of small vortices if two rings approach each to other as shown in Fig. 9.7 (see red circle). In this case the energy of small vortices turns into the energy of the big vortex. This process is referred to as the energy back scattering. Statistically, the direct energy flux sufficiently surpasses the backward one.

9.2.5   Richardson poem (1922)

The vortex turbulence cascade means that large eddies break down to form small eddies as turbulence cascades from large scales to small ones. This idea was formulated in the famous poem by Richardson (1922):

Big whorls have little whorls,
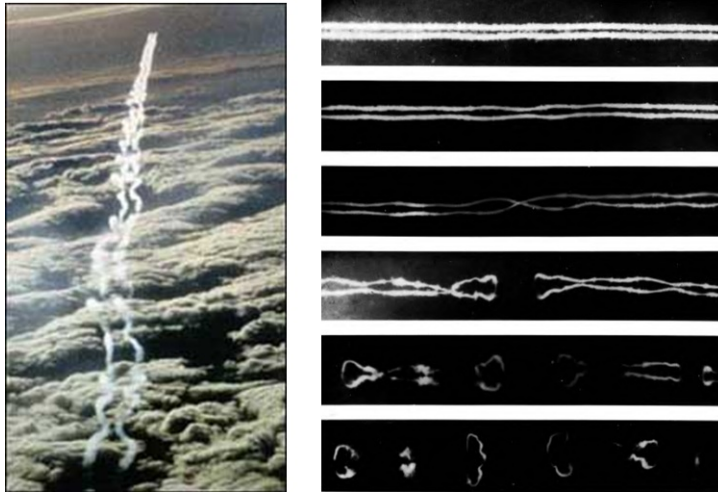
Figure 9.8: Sample of the vortex reconnection of tip vortices behind an airplane.

Which feed on their velocity;
And little whorls have lessor whorls,
And so on to viscosity (in the molecular sense).

9.2.6   Summary

Vortex arise in the fluid due to viscosity effects. They experience instability and amplification. Diffusion counteracts the amplification. If the Reynolds number is large, the vortex structures are strong and concentrated. The amplification can dominate at some fluid region over the diffusion. The vortex instability is not damped by viscosity. The flow becomes stochastic due to mutual interaction of unstable vortices. The big vortices break down into small ones by means of vortex reconnection. The vortex instability process is identified as the turbulence.

9.3   Experimental observations

Different regimes of the fluid motion were revealed very early, perhaps, in antique times. Much later, Leonardo da Vinci recognized two states of the fluid motion and introduced the term "la turbolenza". Arkady Tsinober in his book "An informal introduction to turbulence" [1] presented most outstanding results in turbulence research in chronological order (Fig. 9.9).

1500 Recognition of two states of fluid motion by Leonardo da Vinci and use of the term *la turbolenza*.
1839 'Rediscovery' of two states of fluid motion by G. Hagen.
1883 Osborne Reynolds' experiments on pipe flow. Concept of critical Reynolds number - transition from laminar to turbulent flow regime.
1887 Introduction of the term 'turbulence' by Lord Kelvin.
1895 Reynolds decomposition.
1909 D. Riabuchinsky invents the constant-current hot-wire anemometer.
1912 J.T. Morris invents the constant-temperature hot-wire anemometer.
1921, 1935 Statistical approach by G.I. Taylor.
1922 L.F. Richardson's hierarchy of eddies.
1924 L.V. Keller and A.A. Friedman formulate the hierarchy of moments.
1938 G.I. Taylor discovers the prevalence of vortex stretching.
1941 A.N. Kolmogorov local isotropy, 2/3 and 4/5 laws.
1943 S. Corrsin establishes the existence of the sharp laminar/turbulent interface in shear flows.
1949 Discovery of intrinsic intermittence by G. Batchelor and A. Townsend
1951 Turbulent spot of H.W. Emmons
1952 E. Hopf functional equation.
1967 Bursting phenomenon by S. J. Kline *et al.*
1976 Recapitulation of large scale coherent structures by A. Roshko.

Figure 9.9: Most outstanding results in turbulence research according to [1].

9.3.1 Laminar - turbulent transition in pipe. Experiment of Reynolds

Quantitative study of turbulence was started by Osborne Reynolds (1842-1912) who performed in 1883 very famous experiment shown in Fig. 9.10. The water flows from the vessel A to the pipe B. The ink injected into the pipe B with the local flow velocity is not mixed in transversal direction and keeps its identity if the flow velocity is small (Fig. 9.10, right). The flow under such a condition is laminar. As soon as the flow velocity increases due to water level raise in the vessel A, the ink jet loses the stability and is mixed with surrounding water (Fig. 9.10, right). The flow becomes turbulent. Ink jet development at different flow velocities in the circular pipe is shown in Fig. 9.11.

The great merit of Reynolds lies in the fact, that he in contrast to his predecessors quantified the laminar turbulent transition. He showed that the transition in pipes occurs if the Reynolds number $Re = U_b D / \nu$ exceeds the threshold around ~ 2400. Here U_b is the bulk velocity in pipe determined as the ratio of the flow rate to the pipe cross section, i.e. $U_b = Q/(\pi D^2/4)$, D is the pipe diameter and ν is the kinematic viscosity coefficient ($\nu \sim 10^{-6} m^2 s^{-1}$ for water and $\nu \sim 10^{-6} m^2 s^{-1}$ for air). Later, it was shown that the transition strongly depends on the perturbations presented in the flow. The experimental setup of Reynolds has been preserved at the University of Manchester in
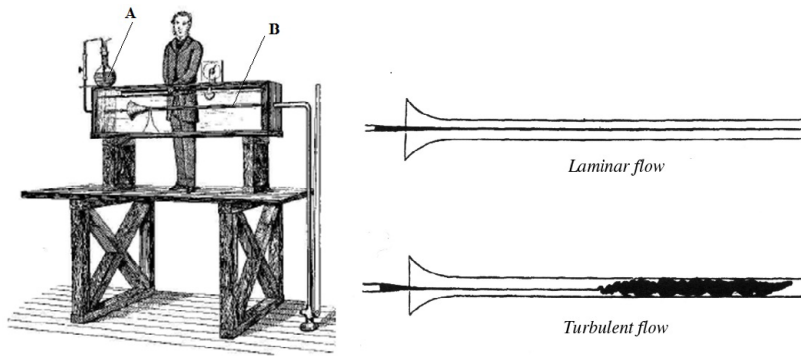
Figure 9.10: Sketch of the Reynolds experiment.
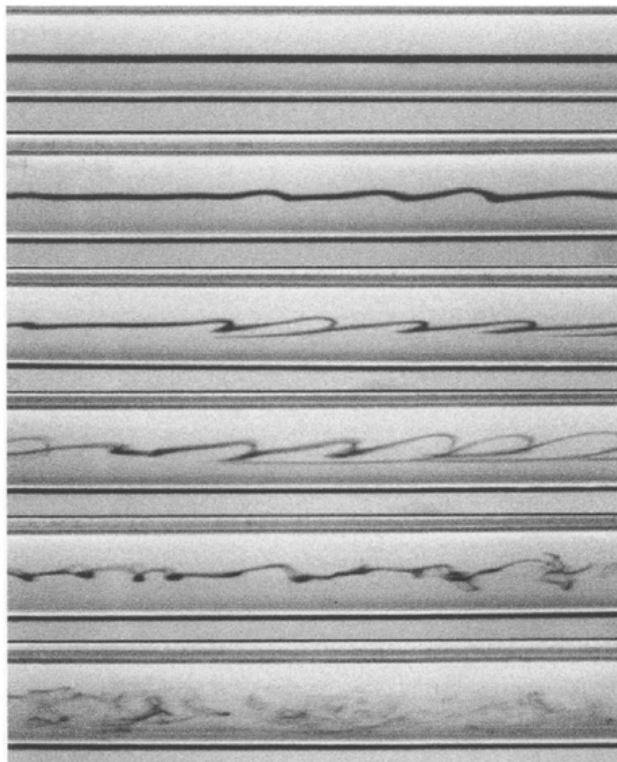
Figure 9.11: Development of instability during the laminar- turbulent transition in the circular pipe (taken from [1]).

UK. The experiments done nowadays shown that the laminar- turbulent transition Reynolds number is less than that documented originally by Reynolds. The reason is, presumably, the building vibration and noise caused by traffic which was not in time of Reynolds. If the perturbations are eliminated the transition can be delayed up to $Re \sim 40000...50000$.

9.3.2 Laminar - turbulent transition and turbulence in jets

The jet flows experiences also laminar turbulent transition shown in Fig. 9.12. Obviously, the flow can be fully or only partially turbulent. Close to the nozzle the flow is laminar. The instability is developed downstream. The shear flow at the jet boundary is the area of rapid velocity change from the jet velocity to zero outside of the jet. The shear flow experiences the so called Kelvin Helmholtz instability (Fig. 9.13) resulting in formation of concentrated vortices which are approximately circular. It happens close to jet nozzle at $x/D < 1$ (see Fig. 9.14), where x is the distance from the nozzle and D is the nozzle diameter.

The Kelvin Helmholtz vortices experience then the pairing (see Fig. 9.14). One vortex overtakes the neighbor vortex creating a pair. This process has an inviscid convective nature and can be explained thinking back to the famous leapfrog motion of two vortex rings. In the inviscid flow the leapfrog motion is running as long as the convective instability destroys the vortices. One vortex runs the next down, its radius decreases whereas the speed increases. The radius of the next vortex increases, the speed decreases. The first ring moves through the second one. The process is then repeated. The movie illustrating this process can be downloaded from http://www.lemos.uni-rostock.de/en/gallery/.

The paired vortices experience the azimuthal instability and takes the crude ring form. Later they are destroyed downstream in the region $1 < x/D < 6$. In far field at large x/D the vortex structures look like a tree with branches oriented against the main flow direction (see Fig. 9.15).
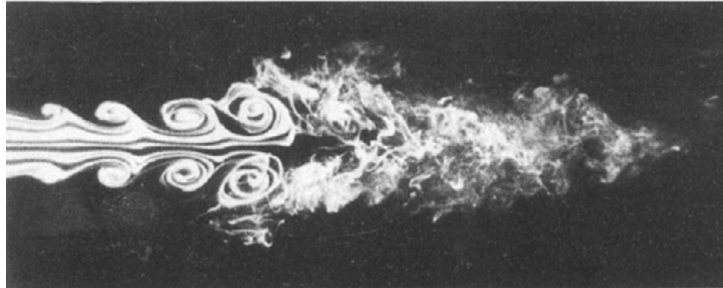
Figure 9.12: Development of instability in the jet (taken from [1]).
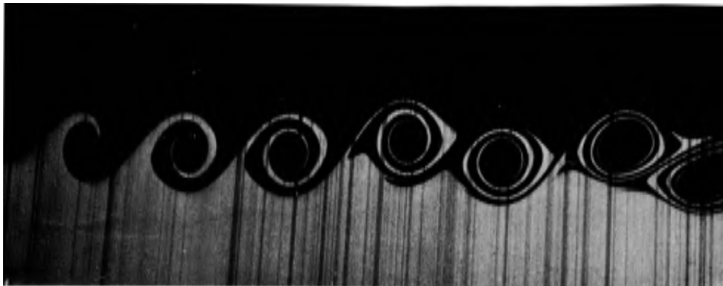
Figure 9.13: Development of instability in the free jet.
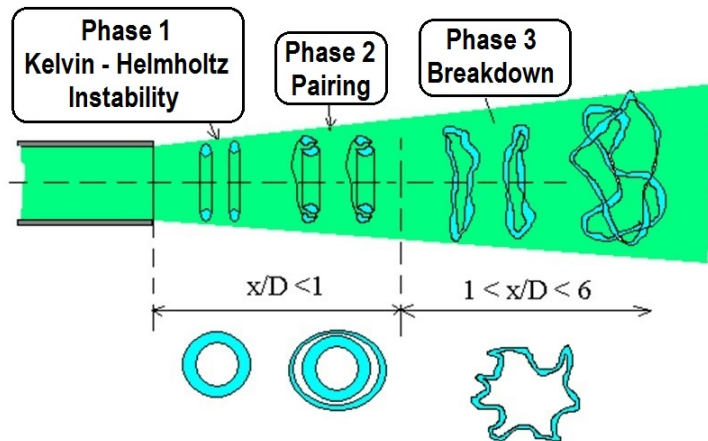
Figure 9.14: Development of instability in the free jet.

Creation of vortex rings is the reason for the jet noise. The noise produced, for instance, by jet propulsors of airplanes is the action of these vortices. The vortices play a significant positive role in jet mixers widely used in food industry, chemical engineering, etc. That is why, one of the most perspective way to reduce the noise or to increase mixing is the manipulation of vortices arising behind the jet nozzle. To increase the mixing it is necessary to strengthen the Kelvin Helmholtz vortices. To decrease the noise the vortices should be broken down into small ones. Fig. 9.16 shows the effect of the acoustic impact on jet. The original vortices (lower picture) are split into small ones (upper picture).

High resolution laser diagnostics methods LIF and PIV allow to get a deep inside into the structure of the turbulent flow. Fig. 9.17 shows the structure of the confined jet mixer flow displayed by Planar Laser Induced Fluorescence (PLIF) Method. The macrostructure obtained with low resolution is shown in the upper Figure. A small window with sizes $2.08mm \times 2.72mm$
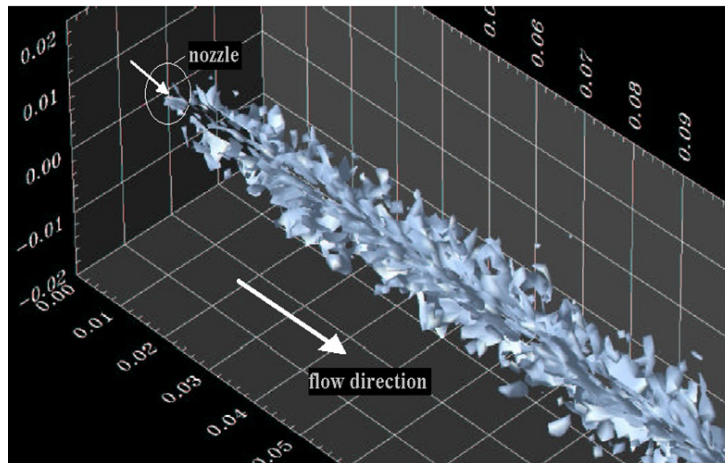
Figure 9.15: Vortex structures in a free jet in a far field.
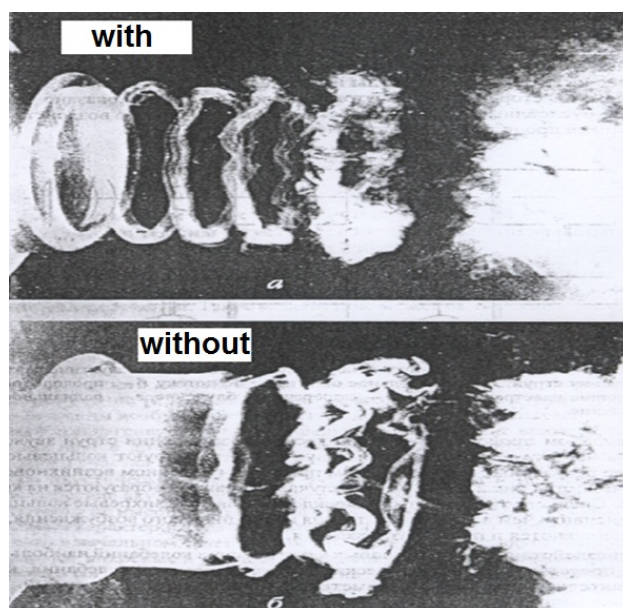
Figure 9.16: Vortex structures in a free jet with acoustic impact [46].
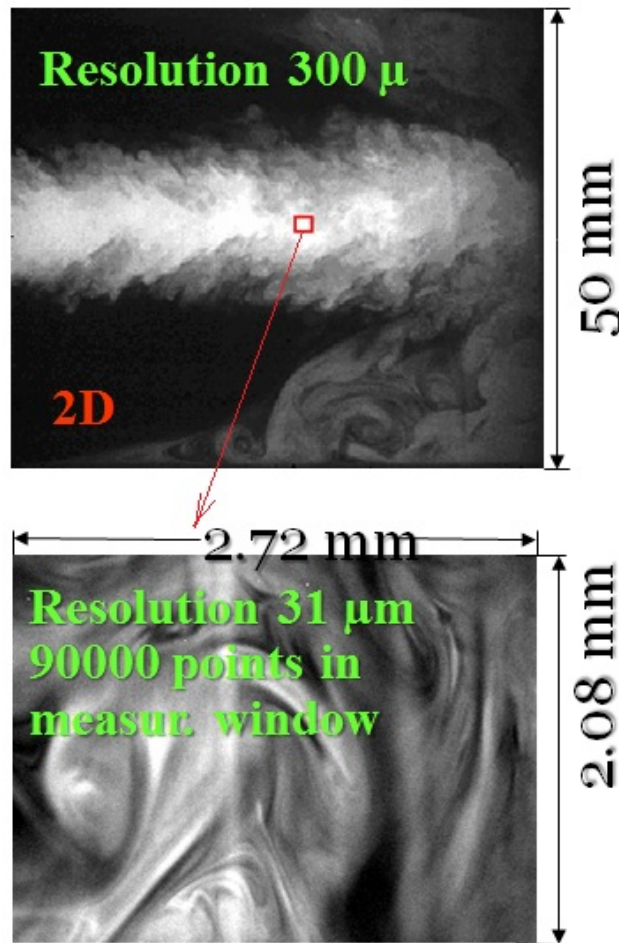
Figure 9.17: Vortex structures in a confined jet mixer flow [47].

9.3.3 Laminar - turbulent transition in wall bounded flows

The boundary layer on a plate is the thin layer of rapid change of the velocity from zero to 99.5% of the incident flow. A possible scenario of the laminar turbulent transition in the boundary layer on a flat plate is shown in Fig. 9.19 First, the transversal vortices are generated in the boundary layer due to the so called Tollmien- Schlichting instability [12]. They experience the secondary instability and form downstream the lambda structures. The latter interact each with other and experience the tertiary instability. They loss original regular form and become stochastic. An important feature of the turbulent boundary layer is the presence of streaks (strips) of the low velocity fluid regions (see Fig. 9.20). They arise due to induction of lambda
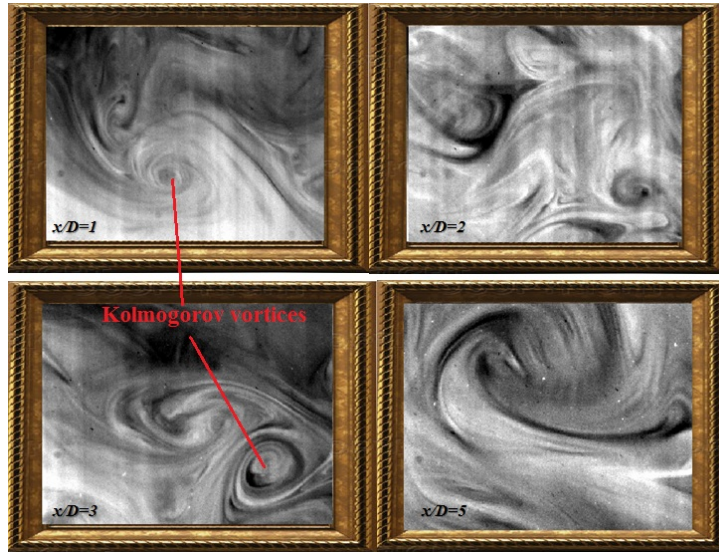
Figure 9.18: Fine vortex structures in a confined jet mixer flow. PLIF measurements by Valery Zhdanov (LTT Rostock). Spatial resolution is $31\mu m$.

structures schematically shown in Fig. 9.21.

9.3.4 Distribution of the averaged velocity in the turbulent boundary layer

A remarkable feature of the turbulent boundary flow is the presence of three typical velocity distribution regions. The instantaneous velocity distributions can be quite different (see Fig. 9.24). However, the averaged velocity has typical distribution close to the wall regardless of the flow type.

Let us introduce the following designations:

- y is the distance from the wall,

- τ_w is the stress at the wall,

- $u_\tau = \sqrt{\frac{\tau_w}{\rho}}$ is the friction velocity,

- $y^+ = \frac{u_\tau y}{\nu}$ is the dimensionless wall distance.

The stress in wall turbulence flow can be considered as the sum of the laminar and turbulent stresses:

$$\tau = \tau_l + \tau_t \tag{9.12}$$
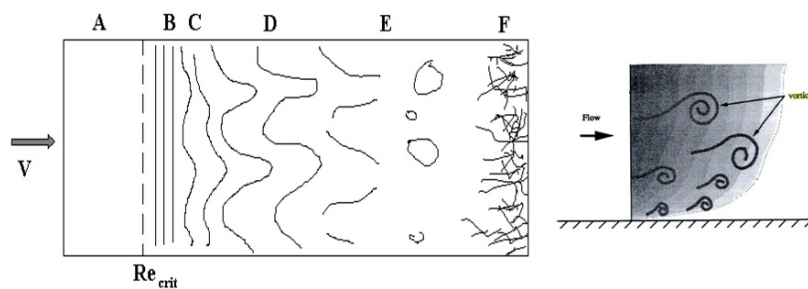
Figure 9.19: Scenario of laminar turbulent transition in the boundary layer on a flat plate.
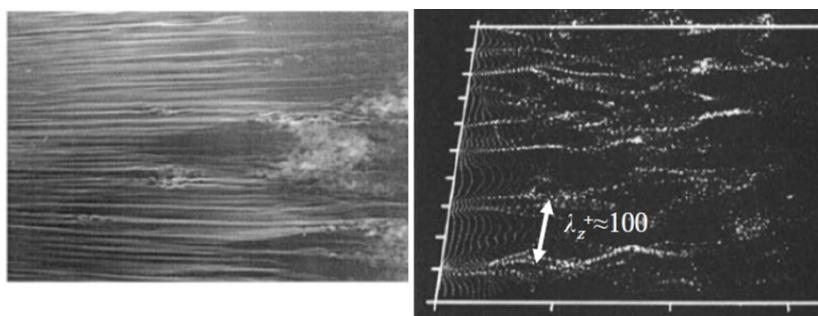
Figure 9.20: Streaks visualized by hydrogen bubbles in the boundary layer on a flat plate.

Close to the wall the turbulent fluctuations are weak. The laminar stress τ_l dominates over the turbulent one τ_t, i.e. $\tau \sim \tau_l$. We consider the thin boundary layer, i.e. the stress is approximately equal to the wall stress τ_w:

$$\tau \approx \tau_w \tag{9.13}$$

Applying the Newton hypothesis (1.18) to the two dimensional wall bounded flow, one gets from (9.13)

$$\tau_w = \rho v \frac{du_x}{dy} \tag{9.14}$$

or

$$\frac{u_x}{u_\tau} = y^+ + C \tag{9.15}$$

From the condition at the wall $u_x = 0$ the unknown constant C is zero, i.e.
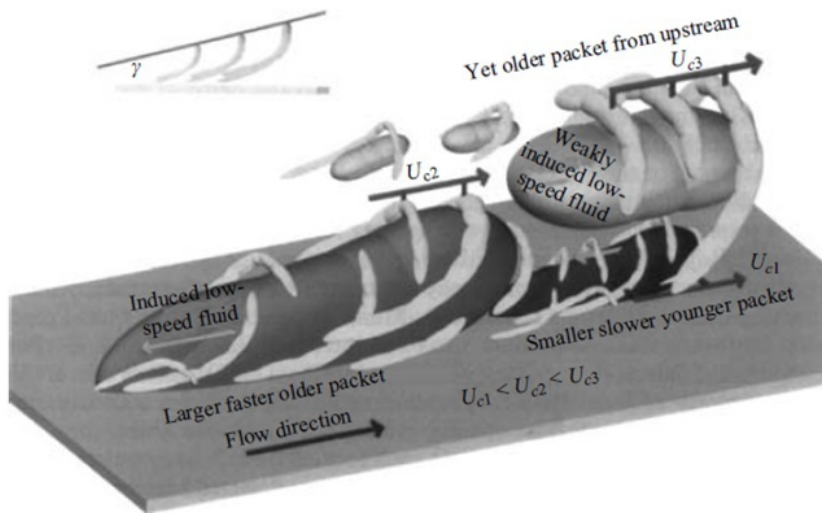
Figure 9.21: Conceptual model of the organization of the turbulence close to the wall proposed by Adrian et al. (2000).
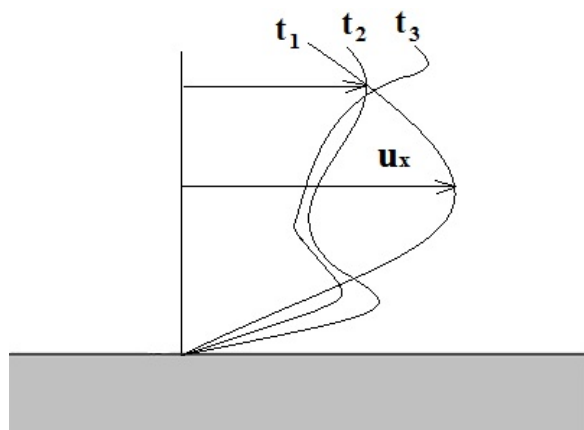
Figure 9.22: Vertical distribution of the velocity u_x at three different time instants in boundary layer.

$$\frac{u_x}{u_\tau} = y^+ \qquad (9.16)$$

Close to the wall the velocity increases linearly $u_x \sim y$. This law confirmed in measurements is valid in the range $0 < y^+ < 5$. This region is reffered to as the viscous sublayer.

Far from the wall the laminar stresses are smaller than the turbulent ones $\tau \sim \tau_t$. The turbulent stress τ_t can be found from the Prandtl mixing length model. The instantaneous velocities are presented as the sum of averaged $\overline{u}$ and fluctuation u' parts:

$$u_x = \overline{u}_x + u'_x, u_y = u'_y, \overline{u}_y = 0 \qquad (9.17)$$

The averaged velocities are defined as

$$\overline{u}_x = \lim_{T \to \infty} \int_0^T u_x(t)dt \qquad (9.18)$$

The turbulent stress $\tau_{12} = \tau_{xy}$ according to the definition is

$$\tau_{12} = \rho \overline{u'_x u'_y} \qquad (9.19)$$
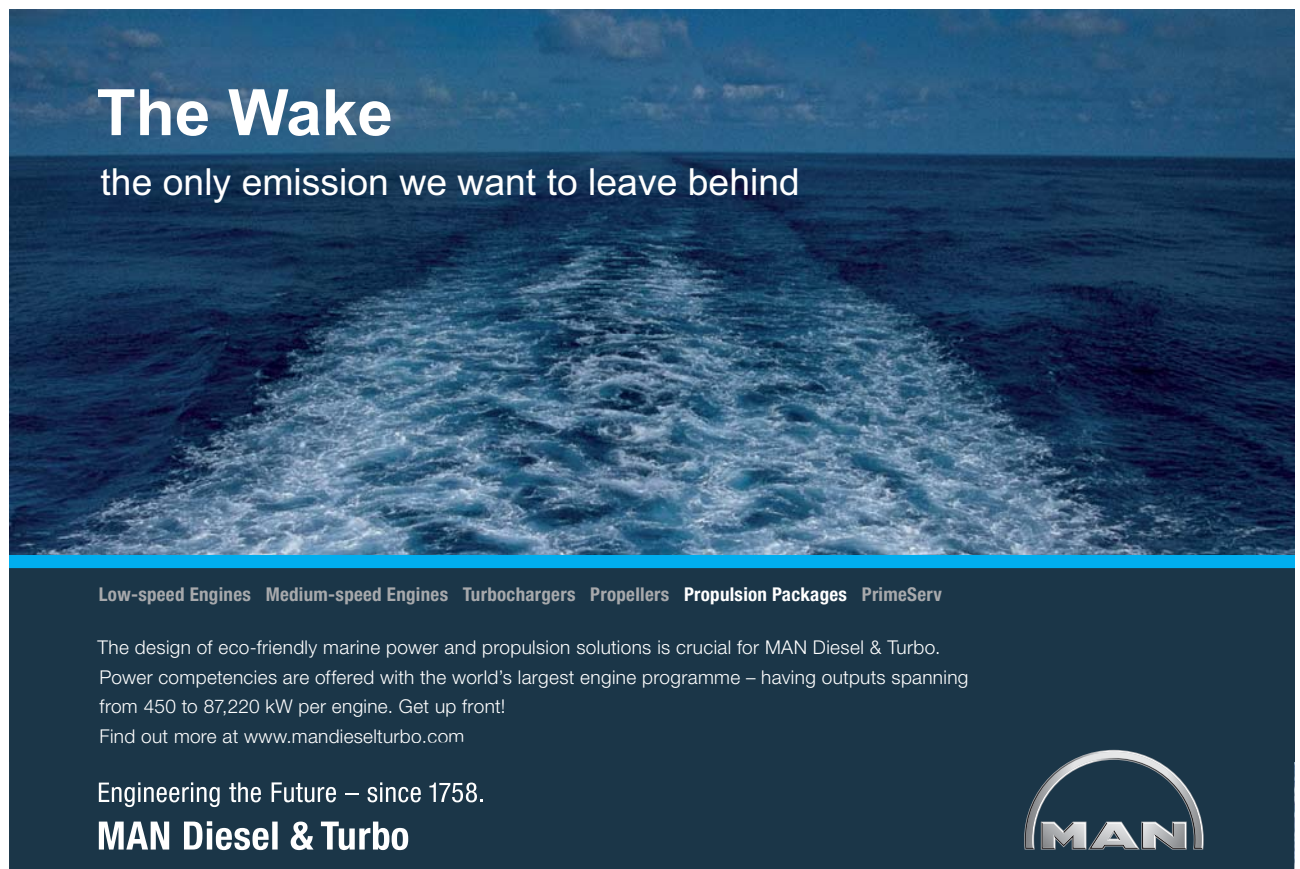
$$u_x = \overline{u}_x + u_x', \, u_y = u_y', \, \overline{u}_y = 0$$
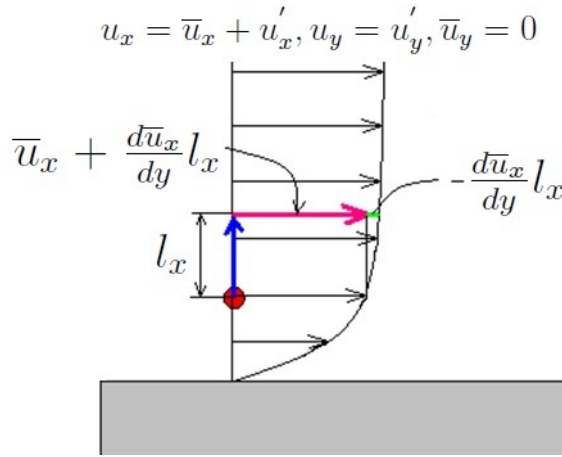
Figure 9.23: Illustration of the Prandtl derivation.

Prandtl proposed in 1925 a very simple algebraic relation for $\overline{u_x' u_y'}$ using ideas from the kinetic gas theory developed by Boltzmann. Let us consider the fluid particle at the distance y from the wall. Let the particle velocity be equal to the averaged velocity at y: $\overline{u}_x$. Due to some perturbations the particle jumps from the position y to the position $y + l_x$ and attains the fluid layer with the averaged velocity $\overline{u}_x + \frac{d\overline{u}_x}{dy} l_x$. Since the particle has velocity $\overline{u}_x$, the velocity at the point $y + dy$ is changed. Obviously, this change is $-\frac{d\overline{u}_x}{dy} l_x$, or:

$$\sqrt{\overline{u_x'^2}} = \frac{d\overline{u}_x}{dy} l_x \tag{9.20}$$

Root square of the averaged squared pulsation in vertical direction is written in a similar form:

$$\sqrt{\overline{u_y'^2}} = \frac{d\overline{u}_x}{dy} l_y \tag{9.21}$$

Introducing the correlation coefficient $R_{xy} = \overline{u_x' u_y'} / \left(\sqrt{\overline{u_y'^2}} \sqrt{\overline{u_y'^2}} \right)$ and using (9.20) and (9.21) one gets:

$$|\tau_{12}| = |\tau_t| = \rho R_{xy} l_x l_y \left(\frac{d\overline{u}_x}{dy} \right)^2 = \rho l^2 \left(\frac{d\overline{u}_x}{dy} \right)^2 \tag{9.22}$$

where $l^2 = R_{xy} l_x l_y$ is the mixing length of Prandtl. The mixing length is determined from empirical data. For instance, the length for the wall bounded flow is

$$l = \kappa y \tag{9.23}$$

κ is the first constant of the turbulence, or the constant of Karman. It is equal to 0.41. Van Driest proposed the modification of (9.23) to take the wall damping effect into account:

$$l = \kappa y \left(1 - e^{\frac{-y u_\tau}{\nu A}} \right) \tag{9.24}$$

where A is the Van Driest constant, which is equal to **26** or **27**. In shear flows $l = Const \cdot \delta(x)$, where δ is the shear layer thickness.

We consider again the thin boundary layer, i.e. the stress is approximately equal to the wall stress $\tau_w = \tau_{12}$. Using (9.22) and (9.23) we get

$$\tau_w = \rho l^2 \left(\frac{d\bar{u}_x}{dy} \right)^2 \tag{9.25}$$

$$\frac{d\bar{u}_x}{dy} = \frac{1}{l} \sqrt{\frac{\tau_w}{\rho}} = \frac{u_\tau}{\kappa y} \tag{9.26}$$

The differential equation (9.26) reads

$$\frac{u_x}{u_\tau} = \frac{1}{\kappa} \ln y^+ + C \tag{9.27}$$

The constant C is approximately equal to **5.2**. The region (9.27) is referred to as the logarithmic region which takes place within $30 < y^+ < 300$. The region $5 < y^+ < 30$ between the viscous and the logarithmic regions is called the buffer layer. The region at $y^+ > 300$ is the wake region. The results of the analysis are summarized in Fig. 9.24
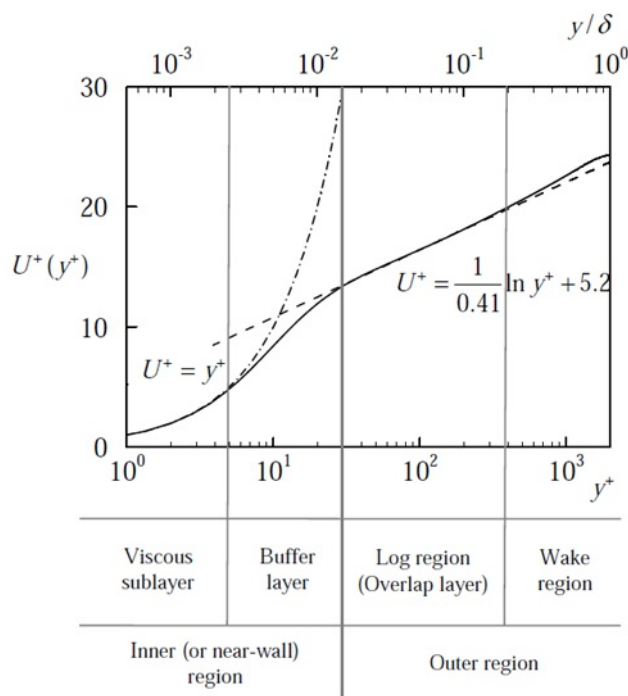
Figure 9.24: Structure of the velocity distribution in the turbulent boundary layer. $U^+ = u_x/u_\tau$.

Chapter 10

Basic definitions of the statistical theory of turbulence

10.1 Reynolds averaging

Reynolds proposed to represent any stochastic quantity in turbulent flow as the sum of its averaged part and fluctuation. For instance, this representation applied for velocity components reads

$$u_x = \bar{u}_x + u'_x; \quad u_y = \bar{u}_y + u'_y; \quad u_z = \bar{u}_z + u'_z; \quad (10.1)$$

The Reynolds averaged velocities are

$$\left.\begin{array}{l} \bar{u}_x = \lim_{T\to\infty} \dfrac{1}{T} \displaystyle\int_0^T u_x dt; \quad \bar{u}_y = \lim_{T\to\infty} \dfrac{1}{T} \displaystyle\int_0^T u_y dt; \\[3em] \bar{u}_z = \lim_{T\to\infty} \dfrac{1}{T} \displaystyle\int_0^T u_z dt \end{array}\right\} \quad (10.2)$$

The averaged fluctuation is zero

$$\overline{u'_{x,y,z}} = 0$$

The root of the averaged square of fluctuations is called root mean square, or r.m.s.. The quantity averaged twice is equal to quantity averaged once $\overline{\overline{u}} = \overline{u}$.

If the turbulence process is statistically unsteady (for instance r.m.s is changed in time), the definition of the Reynolds averaging (10.2) is not applicable and should be extended using the concept of ensemble averaging. Within the ensemble averaging the stochastic process is repeated N times from the initial state. The turbulent quantity u is measured at a certain time t^* N times. The ensemble averaged quantity is then:

$$\overline{u}(t^*) = \lim_{N \to \infty} \frac{1}{N} \sum_{i=1}^{N} u_i(t^*)$$

10.2 Isotropic and homogeneous turbulence

The turbulence is isotropic if r.m.s of all three velocity fluctuations are equal

$$\overline{u'^2_x} = \overline{u'^2_y} = \overline{u'^2_z} \tag{10.3}$$

The turbulence parameters are invariant with respect to the rotation of the reference system. The turbulence is homogeneous in some fluid volume if all statistical parameters are the same for all points in this volume, i.e. $\overline{u'^2_{x,y,z}(\vec{x})} = \overline{u'^2_{x,y,z}(\vec{x} + \vec{r})}$. This equality can be written for all statistical moments. The turbulence parameters are invariant with respect to the translation of the reference system.

10.3 Correlation function. Integral length

The product of two fluctuations is the correlation. The product of two fluctuations at two point separated by the distance $\vec{r}$ is the correlation function:

$$R_{ij}(\vec{x}, \vec{r}) = \overline{u'_i(\vec{x}) u'_j(\vec{x} + \vec{r})} \tag{10.4}$$

If $i = j$ the correlation function R_{ii} is reffered as to the autocorrelation function. In homogeneous turbulence R_{ii} depends only on the separation:

$$R_{ij}(\vec{r}) = \overline{u'_i(\vec{x}) u'_j(\vec{x} + \vec{r})} \tag{10.5}$$

The coefficient of the autocorrelation function is changed between zero and
one:

$$\rho_{ii}(\vec{x}, \vec{r}) = \frac{\overline{u_i'(\vec{x})u_i'(\vec{x}+\vec{r})}}{\overline{u_i'^2(\vec{x})}} \qquad (10.6)$$

A sample of the autocorrealtion function coefficient for scalar fluctuation f'
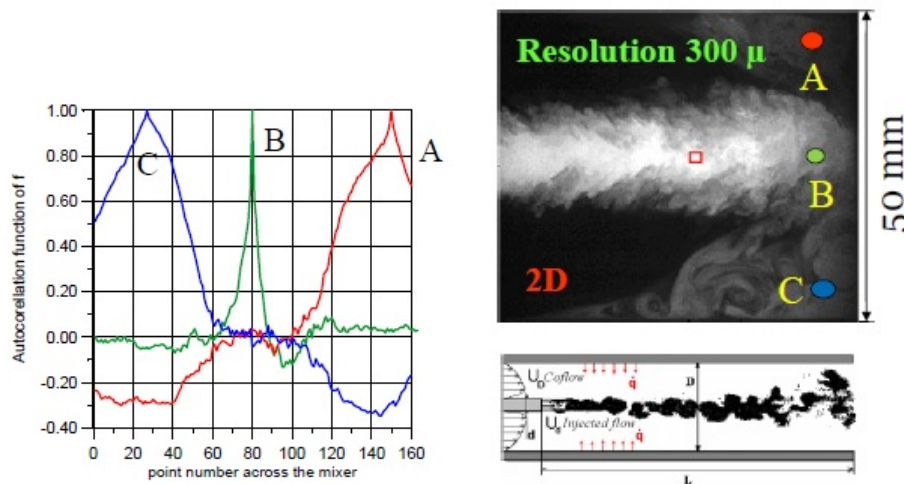
Figure 10.1: Autocorrelation function coefficient for scalar fluctuation at
three different points A, B and C across the jet mixer [47].

$$\rho_f(\vec{x}, \vec{r}) = \frac{\overline{f'(\vec{x})f'(\vec{x}+\vec{r})}}{\overline{f'^2(\vec{x})}} \qquad (10.7)$$

at three different points A, B and C across the jet mixer is shown in Fig. 10.1.
In measurements presented in Fig. 10.1 the scalar f is the concentration of
the dye injected from the nozzle (see Fig. 10.1, low picture, right). The
change of the function has a certain physical meaning. Let us consider the
autocorrelation function with respect to the point C (blue line):

$$\rho_f(r_C, r) = \frac{\overline{f'(r_C)f'(r_C+r)}}{\overline{f'^2(r_C)}} \qquad (10.8)$$

where r is the radial coordinate across the pipe. The $\rho_f(r_C, r_A)$ is negative. It
means the increase of the quantity f at the point C ($f'(r_C) > 0$) is followed
by the decrease of this quantity at the point A ($f'(r_A) < 0$) . This is true in
statistical sense, i.e. the most probable consequence of the increase $f(r_C)$ is
the decrease of $f(r_A)$.

The correlation function and autocorrelation function can be written not only for spatial separation but also for separation in time. For example, the autocorrelation temporal function of the u_i fluctuation is

$$\rho_{ii}(\vec{x}, \tau) = \frac{\overline{u_i'(\vec{x}, t)u_i'(\vec{x}, t + \tau)}}{\overline{u_i'^2(\vec{x}, t)}} \qquad (10.9)$$

The integral of the spatial autocorrelation functions

$$L_{ij}(\vec{x}) = \int\limits_0^\infty \rho_{ii}(\vec{x}, x_j)dx_j \qquad (10.10)$$

is the integral length. The integral lengths are estimations of the size of the largest vortex in flow. A sample of the integral length of the scalar field f along the jet mixer centerline (Fig. 10.1, right)

$$L_f(x) = \int\limits_{-D/2}^{D/2} \rho_f(r)dr \qquad (10.11)$$

is shown in fig. 10.2, where ρ_f is the autocorrelation function across the jet mixer, d is the nozzle diameter, D is the diameter of the closing pipe. L_f is the estimation of the largest structure of the scalar field (in this case, the size of the spot of colored liquid injected from the nozzle).

The integral of the temporal autocorrelation functions

$$T_i(\vec{x}) = \int_0^\infty \rho_{ii}(\vec{x}, \tau)d\tau \qquad (10.12)$$

is the integral time length.

Coefficients of the autocorrelation function of the axial velocity fluctuations for the free jet are presented in Fig. 10.3. The line 1 corresponds to the autocorrelation function calculated along the jet boundary line (shown by the blue line in Fig. 10.3, right). The line 2 corresponds to the autocorrelation function calculated along the jet axis. Oscillating character of the dependency $R_{uu}(\Delta x/d)$ indicates the presence of vortex structures arising at the jet boundary and attaining the jet axis. The distance between zero points is roughly the vortex size.

10.3.1   Some relations in isotropic turbulence

In the isotropic turbulence $u'^2 = \overline{u'_l(x)u'_l(x)} = \overline{u'_t(x)u'_t(x)} = ...$ the autocorrelation function can be represented in the form [13]
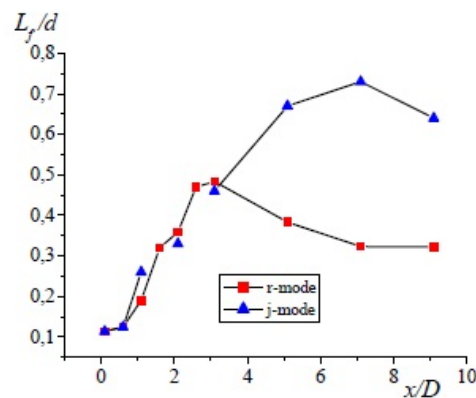
Figure 10.2: Distribution of the integral length of the scalar field along the jet mixer centerline. [47].
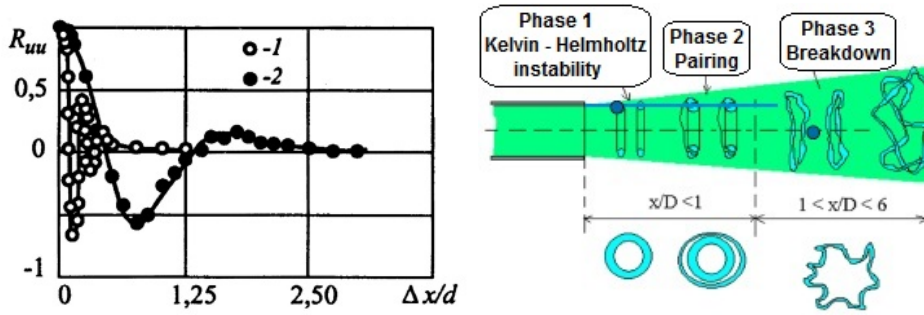
Figure 10.3: Autocorrelation functions in free jet flow [46].

$$R_{ij} = u^2 \left(\frac{f - g}{r^2} r_i r_j + g \delta_{ij} \right) \tag{10.13}$$

where

$$f(r) = \frac{\overline{u'_l(x) u'_l(x + r)}}{\overline{u'_l(x) u'_l(x)}}, \tag{10.14}$$

is the autocorrelation of the longitudinal velocity calculated in longitudinal direction. For instance, the autocorrelation function of the u_x fluctuation calculated in x direction,

$$f(r) = \frac{\overline{u'_x(x) u'_x(x + r)}}{\overline{u'_x(x) u'_x(x)}}, \tag{10.15}$$

or the autocorrelation function of the u_y fluctuation calculated in y direction:

$$f(r) = \frac{\overline{u'_y(y) u'_y(y + r)}}{\overline{u'_y(y) u'_y(y)}}, \tag{10.16}$$

The function $f(r)$ is the same in both cases (10.15) and (10.16). The autocorrelaton function $g(r)$ is calculated for transversal velocities along any direction

$$g(r) = \frac{\overline{u'_t(x) u'_t(x + r)}}{\overline{u'_t(x) u'_t(x)}} \tag{10.17}$$

For instance, the autocorrelation function of the u_x fluctuation calculated in y direction,

$$g(r) = \frac{\overline{u'_x(y) u'_x(y + r)}}{\overline{u'_x(y) u'_x(y)}}, \tag{10.18}$$

or the autocorrelation function of the u_y fluctuation calculated in x direction:

$$g(r) = \frac{\overline{u'_y(x) u'_y(x + r)}}{\overline{u'_y(x) u'_y(x)}}, \tag{10.19}$$

The function $g(r)$ is the same in both cases (10.18) and (10.19). The velocities components used in the previous definitions are illustrated in Fig. 10.4. u_i is the velocity pulsation vector, u_{il} is its projection on the direction connecting two points (i.e. longitudinal direction), u_{it} is its projection on the transversal direction. Products like $u_{it}u_{it}$ are the correlations between points 1 and 2.
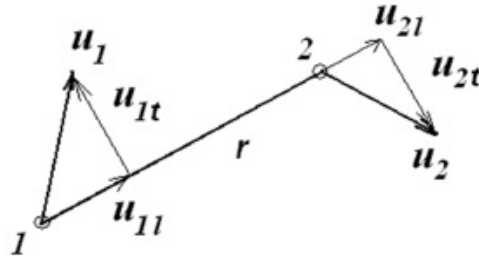
Figure 10.4: Illustrations of velocities used in calculations of the longitudinal f and transversal g autocorrelations.
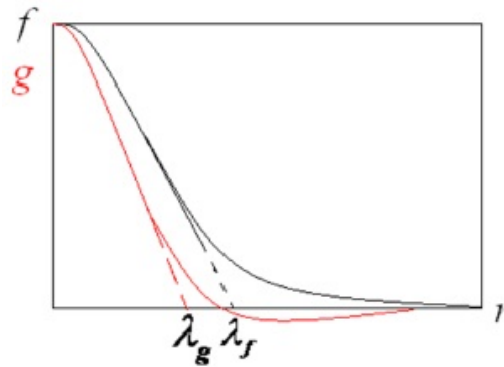
Figure 10.5: Illustration of the autocorrelation functions f and g and Taylor microscales.

The following relations are valid between g and f in the isotropic homogeneous turbulence (see [13]):

$$g = f + \frac{1}{2}r\frac{\partial f}{\partial r} \qquad (10.20)$$

Typical form of f and g is shown in Fig. 10.5. The change of the sign of g function is due to the continuity equation of the velocity field. The integral length calculated using f is twice as large as that calculated using g.

10.3.2 Taylor microscale λ

Until Kolmogorov derived his estimations for vortices in 1941, it has been thought that the minimum vortices arising in the turbulent flow have sizes estimated by Taylor. Let us consider the parabola fitted to the autocorrelation function at point $r = 0$. The parabola intersects the horizontal axis at a certain point. The coordinate of this point λ is the scale introduced by Taylor and called as the Taylor microscale. The Taylor microscale can be calculated through the second derivative of the autocorrelation function at $r = 0$. The Taylor series of f in the vicinity of the point $r = 0$ is

$$f(r) = 1 + \frac{1}{2}\frac{\partial^2 f}{\partial r^2}(0)r^2 + \mathrm{O}(r^4) \qquad (10.21)$$

The parabola fitted to the curve $f(r)$ at $r = 0$ intersects the horizontal axis at the point:

$$\lambda_f = \sqrt{-\frac{2}{\frac{\partial^2 f}{\partial r^2}(0)}} \qquad (10.22)$$

Similar relations can be derived for the transversal autocorrelation

$$\lambda_g = \sqrt{-\frac{2}{\frac{\partial^2 g}{\partial r^2}(0)}} \qquad (10.23)$$

Today the Taylor microscale λ is still in use in turbulent research although it has no physical meaning. Very popular is the Reynolds number based on the Taylor microscale

$$Re = u'\lambda/\nu \qquad (10.24)$$

which characterizes the state of the turbulence in the flow.

10.3.3 Correlation functions in the Fourier space

Any continuous function can be represented in the Fourier space:

$$f(\vec{r}, t) = \int\limits_{-\infty}^{\infty} \hat{f}(\vec{k}, t) e^{i\vec{k}\vec{r}} d\vec{k} \qquad (10.25)$$

The new function $\hat{f}(\vec{k}, t)$ is then known as the Fourier transform and/or the frequency spectrum of the function f. The Fourier transform is also a reversible operation:

$$\hat{f}(\vec{k}, t) = \frac{1}{8\pi^3} \int\limits_{-\infty}^{\infty} f(\vec{r}, t) e^{-i\vec{k}\vec{r}} d\vec{r} \qquad (10.26)$$

The Fourier transformation can be also written for the correlation function:

$$R_{ij}(\vec{r}) = \int\limits_{-\infty}^{\infty} \Phi_{ij}(\vec{k}) e^{i\vec{k}\vec{r}} d\vec{k}, \quad \Phi_{ij}(\vec{k}) = \frac{1}{8\pi^3} \int\limits_{-\infty}^{\infty} R_{ij}(\vec{r}) e^{-i\vec{k}\vec{r}} d\vec{r} \qquad (10.27)$$

Very often one uses one dimensional correlation functions defined as

$$\Theta_{ij}(k_1) = \frac{1}{2\pi} \int\limits_{-\infty}^{\infty} R_{ij}(r_1, 0, 0) e^{-ik_1 r_1} dr_1 = \int\limits_{-\infty}^{\infty}\int\limits_{-\infty}^{\infty} \Phi_{ij}(k_1, k_2, k_3) dk_2 dk_3 \qquad (10.28)$$

Proof of the formula (10.28) The inverse Fourier transform of the function $R_{ij}(r_1, 0, 0)$:

$$\Theta_{ij}(k_1, 0, 0) = \frac{1}{2\pi} \int\limits_{-\infty}^{\infty} R_{ij}(r_1, 0, 0) e^{ik_1 r_1} dr_1 \qquad (10.29)$$

The inverse transformation reads:

$$R_{ij}(r_1, 0, 0) = \int\limits_{-\infty}^{\infty} \Theta_{ij}(k_1, 0, 0) e^{-ik_1 r_1} dk_1 \qquad (10.30)$$

The general definition is

$$R_{ij}(r_1, r_2, r_3) = \int_{-\infty}^{\infty} \int_{-\infty}^{\infty} \int_{-\infty}^{\infty} \Phi_{ij}(k_1, k_2, k_3) e^{i\vec{k}\vec{r}} dk_1 dk_2 dk_3 \qquad (10.31)$$

From the last formula we have:

$$R_{ij}(r_1, 0, 0) = \int_{-\infty}^{\infty} \left(\int_{-\infty}^{\infty} \int_{-\infty}^{\infty} \Phi_{ij}(k_1, k_2, k_3) dk_2 dk_3 \right) e^{ik_1 r_1} dk_1 \qquad (10.32)$$

Comparison of (10.32) with (10.30) results in the desired formula

$$\Theta_{ij}(k_1, 0, 0) = \int_{-\infty}^{\infty} \int_{-\infty}^{\infty} \Phi_{ij}(k_1, k_2, k_3) dk_2 dk_3 \qquad (10.33)$$

10.3.4 Spectral density of the turbulent kinetic energy

According to the definition of the correlation function

$$R_{ij}(\vec{r}) = \overline{u_i'(\vec{x}) u_j'(\vec{x} + \vec{r})} \qquad (10.34)$$

the total turbulent kinetic energy is

$$TKE = \frac{1}{2}R_{ii}(0) = \frac{1}{2}\int_{-\infty}^{\infty} \Phi_{ii}(\vec{k})d\vec{k} = \int_{0}^{\infty} \Phi_{ii}(\vec{k})d\vec{k} \qquad (10.35)$$

The quantity

$$E(k) = \int_{|\vec{k}|} \Phi_{ii}(\vec{k})d\vec{k} \qquad (10.36)$$

is the spectral density of the turbulent kinetic energy. Physically it is the energy on the sphere $k = \sqrt{k_1^2 + k_2^2 + k_3^2}$ in the Fourier space. The total turbulent kinetic energy is then:

$$TKE = \int_{0}^{\infty} E(k)dk \qquad (10.37)$$

10.4   Structure functions

10.4.1   Probability density function

We take the definitions from Wikipedia: In probability theory, a probability density function (pdf), or density of a continuous random variable, is a function that describes the relative likelihood for this random variable to take on a given value. The probability for the random variable to fall within a particular region is given by the integral of this variables density over the region. The probability density function is non negative everywhere, and its integral over the entire space is equal to one.

10.4.2   Structure function

Kolmogorov introduced the structure function of q order for any stochastic function. For instance, for the longitudinal velocity along the longitudinal direction (see Fig. 10.5) it reads:
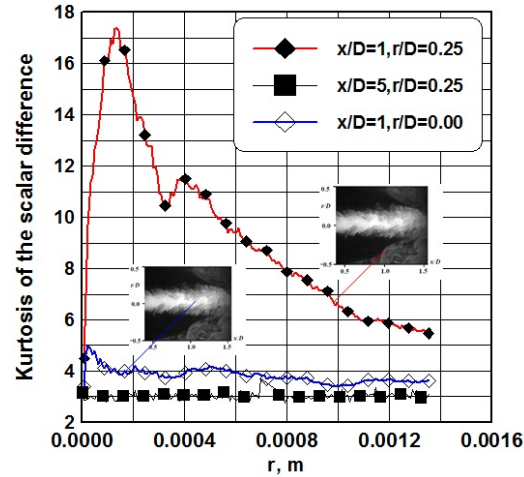
Figure 10.6: Kurtosis of the structure function for the concentration of the scalar field obtained in the jet mixer [47].

$$S_q(l) = \langle (u_{2l} - u_{1l})^q \rangle \tag{10.38}$$

The standard deviation squared is then $\sigma^2 = S_2$. If the p.d.f. of the structure function is described by the Gaussian function

$$p.d.f.(x) = \frac{1}{\sqrt{2\pi}\sigma} e^{\frac{-(x-\mu)^2}{2\sigma^2}} \tag{10.39}$$

where μ is the mean value of the stochastic value, the turbulence is Gaussian. In reality, the most of the turbulence parameters are not Gaussian. The deviations from the Gaussian turbulence is characterized by the kurtosis $Kurt$ and skewness Sk. The kurtosis

$$Kurt = \frac{\langle (u_{2l} - u_{1l})^4 \rangle}{(\langle (u_{2l} - u_{1l})^2 \rangle)^2} \tag{10.40}$$

is three for the Gaussian turbulence. Big values of the kurtosis means that the p.d.f. distribution of the structure function $S_1(l) = \langle u_{2l} - u_{1l} \rangle$ is very flat. The kurtosis is also often called as flatness. If kurtosis for small $l \sim 0$ is big, it means that the field of the stochastic field is very intermittent. Big differences are possible even if the separation between two points l is small. The p.d.f. function has long tails in this case. A sample of kurtosis for the scalar structure function $S(x) = f(x + r) - f(x)$ is given in Fig.10.6.

The skewness

$$Sk = \frac{\langle (u_{2l} - u_{1l})^3 \rangle}{(\langle (u_{2l} - u_{1l})^2 \rangle)^{3/2}} \tag{10.41}$$

is zero for the Gaussian process. For the isotropic turbulence the skewness of the derivative

$$Sk = \frac{\langle \left(\frac{\partial u_l}{\partial l}\right)^3 \rangle}{\left[\langle \left(\frac{\partial u_l}{\partial l}\right)^2 \rangle\right]^{3/2}} \tag{10.42}$$

is equal to -0.5. Physically it means that negative values of the derivative $\frac{\partial u_l}{\partial l}$ are more probable than positive ones. Please prove that the skewness (10.42) is the skewness of the structure functions of the first order $S_1(l) = \langle u_{2l} - u_{1l} \rangle$ calculated at $l \to 0$.

Exercise 1.
Calculate the Reynolds averaged values of the time dependent signals

$$u(t) = \cos^2 t,$$
$$u(t) = \sin t,$$
$$u(t) = \begin{cases} 1 - t, & t \leq 1, \\ 0, & t > 1. \end{cases}$$

Solution:

$$\overline{u(t)} = \frac{1}{2},$$
$$\overline{u(t)} = 0,$$
$$\overline{u(t)} = 0.$$

Exercise 2.
Find the Reynolds stresses for the isotropic turbulence.

$$\begin{pmatrix} 2 & r_{12} & r_{13} \\ r_{21} & r_{22} & r_{23} \\ r_{31} & r_{32} & r_{33} \end{pmatrix}$$

Solution:

$$\begin{pmatrix} 2 & 0 & 0 \\ 0 & 2 & 0 \\ 0 & 0 & 2 \end{pmatrix}$$

Exercise 3.
Calculate the turbulent kinetic energy of the isotropic turbulence, if $r_{33} = 1$

Solution:

$$k = 3/2$$

Exercise 4.
Relation between longitudinal autocorrelation function

$$f(r) = \frac{\overline{u_l(x)u_l(x+r)}}{\overline{u_l^2(x)}}$$

and energy density $E(k)$ is given by formula [13]

$$f(r) = \frac{2}{u_l^2} \int_0^\infty E(k)k^{-2}r^{-2}(\frac{\sin kr}{kr} - \cos kr)dk \qquad (10.43)$$

Energy density of the isotropic decaying turbulence is described as $E(k) = k^4 Exp[-k^2]$. Calculate

- longitudinal autocorrelation function f,

- integral length and

- Taylor microscale

for the isotropic decaying turbulence.

Solution:

$$f(r) = \frac{2}{u_l^2} \int_0^\infty E(k)k^{-2}r^{-2}(\frac{\sin kr}{kr} - \cos kr)dk = \qquad (10.44)$$

$$= \frac{2}{u_l^2} \int\limits_0^\infty Exp[-k^2]k^2 r^{-2}(\frac{\sin kr}{kr} - \cos kr)dk = \frac{1}{4}\sqrt{\pi}Exp[-r^2/4]$$

$$L = \int\limits_0^\infty f(r)dr = \frac{\pi}{4}$$

$$\lambda = \frac{4}{\pi^{1/4}}$$

Exercise 5.

Calculate the probability density function of the time dependent signal

time	0	1	2	3	4	5	6	7	8	9	10	11	12	13	14
signal	0	0.1	0.9	0.5	0.7	0.5	0.05	0.65	0.2	0.78	0.43	0.98	0.67	0.92	0.55

using the increment 0.2.

Solution:

signal	0-0.2	0.2-0.4	0.4-0.6	0.6-0.8	0.8-1.0
p.d.f.	3/15	2/15	3/15	4/15	3/15

Exercise 6.

The velocity u was measured at N points across the pipe: u_i^k, where $i = 1, N$ and $k = 1, K$ is the time step number. Write a program to calculate the autocorrelation function of u with respect to point $N/2$.

Solution:

$$u_i^{k,\prime} = u_i^k - \overline{u_i}$$

$$\overline{u_i} = \frac{1}{K}\sum_{k=1}^K u_i^k$$

$$R(i, N/2) = \frac{\sum\limits_{k=1}^K u_i^{k,\prime} u_{N/2}^{k,\prime}}{\sum\limits_{k=1}^K u_{N/2}^{k,\prime 2}}$$

Chapter 11

Kolmogorov theory K41

11.1 Physical background

One of the most outstanding results in turbulence theory was obtained by Kolmogorov (s. Fig. 11.1) in 1941. The Kolmogorov theory known as K41 is based on the hypothesis of local isotropy of the turbulent motion at small scales. The physical model behind the Kolmogorov theory is the vortex cascado illustrated in Fig. 11.2. Big vortices with scales L (corresponds to the wave numbers π/L in the Fourier space) break up to small ones, which in turn split into even smaller and so on up to the smalles vortices with the scale η. One of the most important vortex break up mechanisms is the vortex reconnection described above. The energy is transferred from big vortices to small ones almost without the loss. The massive dissipation ε takes place at small vortices referred to as the dissipative or the Kolmogorov vortices. The real turbulent vortices are similar to these calculated by Isazawa et al. (Fig. 11.3). Vortices are displayed at three different time instants. The upper pictures are obtained from the lower ones by filtering out the hight frequencies. As seen big vortices are revealed in low frequency simulation. If the resolution is increased, more and more small scale vortex filaments appears on the place of big smooth vortices. Thus, the most important physical processes during the vortex break up are:

- Transfer energy from large scales to small ones and

- Dissipation of the energy in small vortices.

Figure 11.1: Andrey Kolmogorov was a mathematician, preeminent in the 20th century, who advanced various scientific fields (among them probability theory, topology, intuitionistic logic, turbulence, classical mechanics and computational complexity).

Figure 11.2: Illustration of the vortex cascado.

Isazawa et al. Int. J. Pure Appl. Math.(4) 2007.
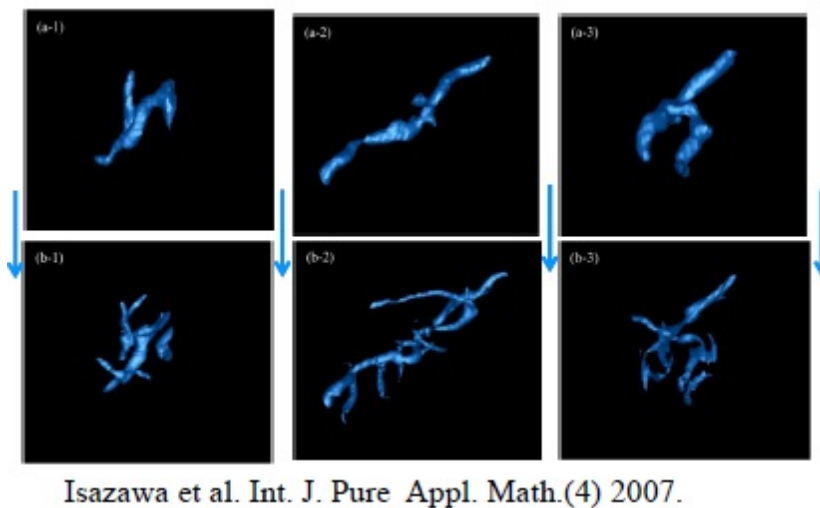
Figure 11.3: Turbulent vortices revealed in DNS calculations performed by Isazawa et al. (2007).

11.2   Dissipation rate

Two parameters, which are of importance during the cascado process, are the kinematic viscosity ν and the dissipation rate ε. The energy dissipation rate per unit mass of a turbulent fluid is given by

$$\varepsilon = \frac{\nu}{2} \sum_{i,j} \left(\frac{\partial u'_i}{\partial x_j} + \frac{\partial u'_j}{\partial x_i} \right)^2 = 2\nu s_{ij} s_{ij} \tag{11.1}$$

where $s_{ij} = \frac{1}{2}\left(\frac{\partial u'_i}{\partial x_j} + \frac{\partial u'_j}{\partial x_i} \right)$ is the fluctuating rate of strain:

$$s_{ij} = S_{ij} - \overline{S}_{ij} = \frac{1}{2}\left(\frac{\partial u_i}{\partial x_j} + \frac{\partial u_j}{\partial x_i} \right) - \frac{1}{2}\left(\frac{\partial \overline{u}_i}{\partial x_j} + \frac{\partial \overline{u}_j}{\partial x_i} \right) \tag{11.2}$$

The dissipation ε is a random function of the coordinates and time, which fluctuates together with the field $\mathbf{u}(\mathbf{x}, t)$. In what follows we consider the mean dissipation rate $\bar{\varepsilon}$ designating it as ε. The energy dissipated by the small vortices is generated by large scale vortices. The energy production is defined as

$$P = \overline{u_i' u_j'} \frac{\partial \overline{u}_i}{\partial x_j} \tag{11.3}$$

Based on the dimension analysis, Prandtl and Kolmogorov proposed the estimation of the integral length of the turbulent flow

$$L \sim \frac{k^{3/2}}{\varepsilon} \tag{11.4}$$

The formula (11.4) is valid for very high Reynolds numbers for the turbulence being in the equilibrium, i.e. the production of the turbulence is compensated by its dissipation, i.e. $P = \varepsilon$.

11.3 Kolmogorov hypotheses

The basis of the Kolmogorov theory are three hypotheses, which are supposed to be valid for high Reynolds numbers $Re_t = \frac{vL}{\nu}$, where $v = \sqrt{TKE} = \sqrt{k}$ is the characteristic fluctuation velocity.

The **Kolmogorov hypothesis of local isotropy** reads:

At sufficiently high Reynolds number Re_t, the small-scale turbulent motions ($l \ll l_{EI}$) are statistically isotropic

Here l_{EI} is the lengthscale as the demarcation between the anisotropic large eddies and the isotropic small eddies. Kolmogorov argued that all information about the geometry of the large eddies - determined by the mean flow field and boundary conditions - is also lost. Directional information at small scales is lost. With the other words, the direction of the vorticity vector ω of small turbulent vortices is uniformly distributed over the sphere. As a consequence, the statistics of the small-scale motions are in a sense universal - similar in every high-Reynolds-number turbulent flow (see [14]).

The **Kolmogorov first similarity hypothesis** reads:

In every turbulent flow at sufficiently high Reynolds number Re_t, the statistics of the small-scale motions ($l < l_{EI}$) have a universal form that is uniquely determined by ν and ε.

For this range of scales we can introduce characteristic size η, characteristic velocity u_η and characteristic time τ_η which depend only on two parameters ν and ε:

$$\eta = \nu^{\alpha_\eta}\varepsilon^{\beta_\nu}, \quad u_\eta = \nu^{\alpha_u}\varepsilon^{\beta_u}, \quad \tau_\eta = \nu^{\alpha_\tau}\varepsilon^{\beta_\tau} \tag{11.5}$$

The analysis of dimension allows one to derive the following dependences:

$$
\begin{aligned}
\eta &= \left(\frac{\nu^3}{\varepsilon}\right)^{1/4}, \\
u_\eta &= (\nu\varepsilon)^{1/4}, \\
\tau_\eta &= (\nu/\varepsilon)^{1/2}
\end{aligned}
\tag{11.6}
$$

Here η is the scale of the smallest dissipative vortices (Kolmogorov scale),
u_η is the characteristic velocity of turning of Kolmogorov vortices,
τ_η is characteristic turn over time of Kolmogorov vortices.
Using expressions

$$\varepsilon \approx \frac{k^{3/2}}{L} \qquad u \approx k^{1/2} \tag{11.7}$$

some useful estimations can be derived from (11.6):

$$\eta/\mathrm{L} \approx (\mathrm{Re_t})^{-3/4},$$
$$\mathrm{u}_\eta/\mathrm{u} = (\mathrm{Re_t})^{-1/4}, \qquad (11.8)$$
$$\tau_\eta/\mathrm{T} = (\mathrm{Re_t})^{-1/2}$$

Very remarkable is the first formula defining the ratio between the smallest and largest vortices in the flow. If L is, say one meter, and the fluctuation $1 m/s$, the turbulent Reynolds number in water is $Re_t = 10^6$. The Kolmogorov scale is in this case 32000 as less as the flow macroscale L. Estimations of the Kolmogorov scale in the jet mixer with nozzle diameter of $d = 1cm$ and closing pipe of $D = 5cm$ diameter is shown in Fig. 11.4.

The **Kolmogorov second similarity hypothesis** reads:

In every turbulent flow at sufficiently high Reynolds number, the statistics of the motions of scale l in the range $L \gg l \gg \eta$ have a universal form that is uniquely determined by ε, independent of ν.

This range is called as the inertial subrange. Since the vortices of this range are much larger than Kolmogorov vortices, we can assume that their Reynolds numbers lu_l/ν are large and their motion is little affected by the viscosity. The energy density depends on the wave number k and the dissipation rate ε

$$E(k) = \varepsilon^\alpha k^\beta \qquad (11.9)$$
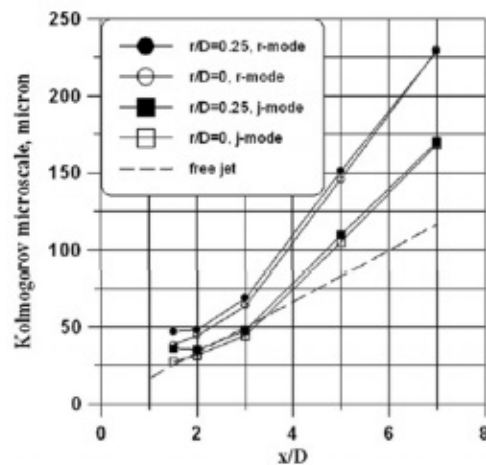
Figure 11.4: Distribution of the Kolmogrov scale along the centerline of the jet mixer and free jet [47]. The dissipation rate ε is calculated from the $k - \varepsilon$ model and the experimental estimation of the Miller and Dimotakis (1991) $\varepsilon = 48(U_d^3/d)((x - x_0)/d)^{-4}$.

The analysis of dimension leads to the Kolmogorov law

$$E(k) = \alpha \varepsilon^{2/3} k^{-5/3} \qquad (11.10)$$

where $\alpha \approx 1.5$ is the constant.

11.4   Three different scale ranges of turbulent flow

Three different ranges can be distinguished in the spectrum of scales in the full developed turbulence at high Reynolds numbers Re_t (Fig.11.5):

- Energy containing range at $l > l_{EI}$ (according to Pope [14], $l_{EI} \approx \frac{1}{6}L$). Within this range the kinetic energy of turbulence is generated and big turbulent eddies are created.

- Inertial subrange at $l_{DI} < l < l_{EI}$ (according to Pope [14], $l_{DI} \approx 60\eta$). Within this subrange the energy is transferred along the scales towards dissipative vortices without any significant loss, i.e. $\varepsilon \sim 0$. The energy density obeys the Kolmogorov law (11.10).

- Dissipation range $l < l_{DI}$. The dissipation of the energy of big vortices occurs within the dissipation range.

The inertial subrange and dissipation range belong to the universal equilibrium range. Three corresponding ranges can be distinguished in the distribution of the energy density over the wave numbers k Fig. 11.6. The presence of the inertial and dissipation subranges was confirmed in numerous experimental measurements performed after development of the K41 theory (see Fig. 11.7, 11.8).
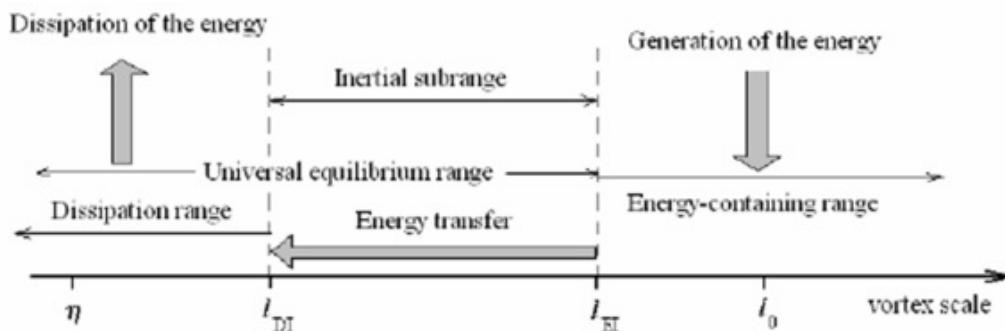
Figure 11.5: Three typical scale ranges in the turbulent flow at high Reynolds numbers.
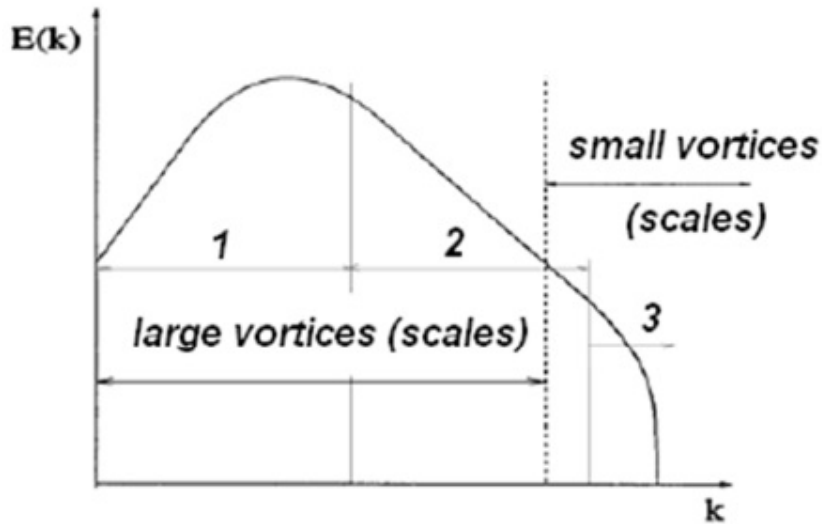
Figure 11.6: Three typical ranges of the energy density spectrum in the turbulent flow at high Reynolds number. 1- energy containing range, 2- inertial subrange, 3- dissipation range.
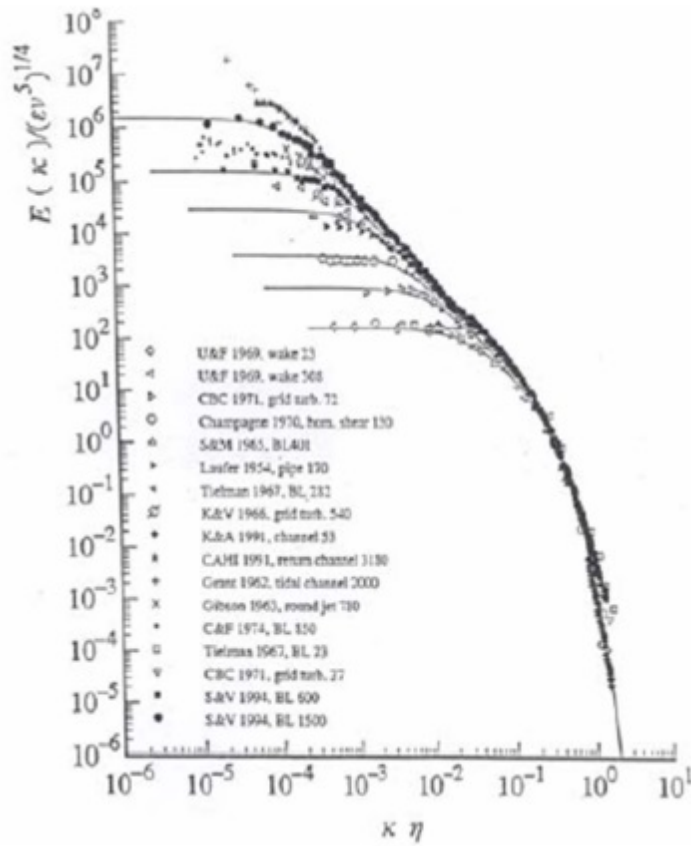
Figure 11.7: Experimental confirmation of the Kolmogorov law. The compensated energy spectrum for different flows [14].
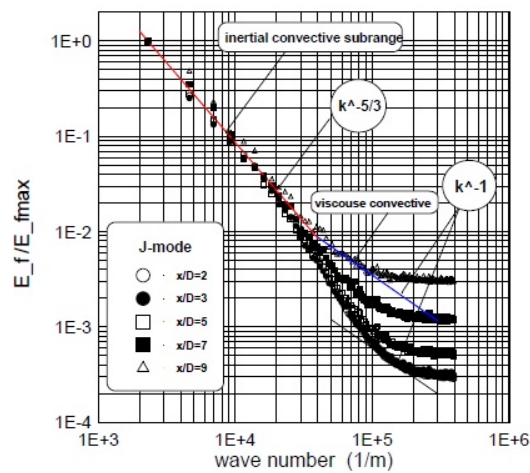
Figure 11.8: Experimental confirmation of the Kolmogorov law for the concentration fluctuations in the jet mixer. Measurements of the LTT Rostock [47].

11.5   Classification of methods for calculation of turbulent flows.

The energy spectrum Fig. 11.6 is used to classify three main methods of turbulent flows modelling (Fig. 11.9). The most general strategy is the Direct Numerical Simulation (DNS). Within the DNS the whole spectrum of turbulent structures is modelled starting from the biggest vortices of the energy containing range till the smallest dissipative Kolmogorov vortices. The Large Eddy Simulation (LES) models the energy containing vortices and a fraction of vortices corresponding to the inertial subrange. The effect of remaining vortices is considered using different approximation models. Since small vortices are universal, the models are also supposed to be universal. The Reynolds averaged Navier Stokes (RANS) models are dealing with the large vortices corresponding to the energy containing range. The effect of other vortices is taken by different semi- empiric models which are not universal.

11.6   Limitation of K-41. Kolmogorov theory K-62

The strongest and simultaneously the most questionable assumption of the Kolmogorov-41 is: Dissipation rate is an universal constant for each turbulent flow. Already in 1942, during a scientific seminar the Nobel price laureate
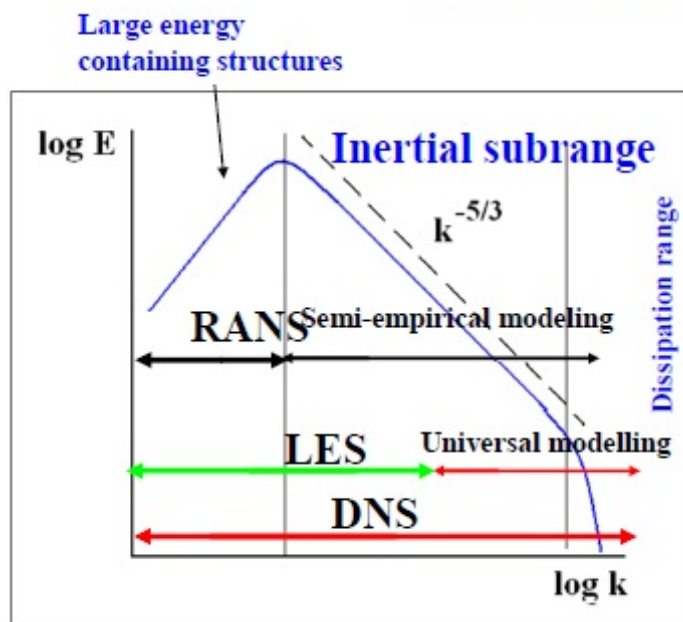
Figure 11.9: Three main methods of turbulent flows modelling.
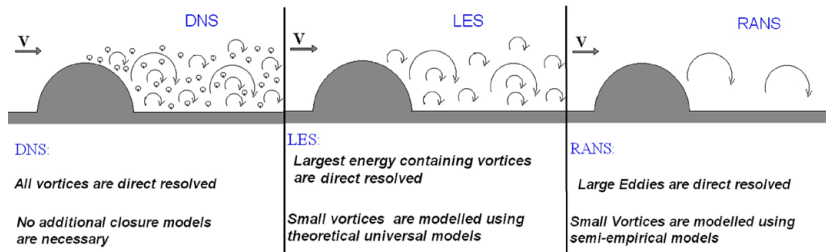
Figure 11.10: Vortex structures resolved by different models.

Landau noted, that the dissipation rate is a stochastic function, it is not constant. We consider the consequences of the neglect of this fact.

According to the Kolmogorov - Obukhov law the structure function of the q-th order

$$S_q(l) = \langle (u_{2l} - u_{1l})^q \rangle \tag{11.11}$$

has the following asymptotic behaviour at small l

$$S_q(l) \sim (\varepsilon l)^q \sim (l)^{\xi q} \tag{11.12}$$

Fig. 11.11 shows that the predictions of Kolmogorov and Obukhov deviate from measurement data. The reason of the discrepancy is the physical phenomenon called the intermittency. The intermittency is caused by the presence of laminar spots in every turbulent flows even at very high Reynolds numbers.
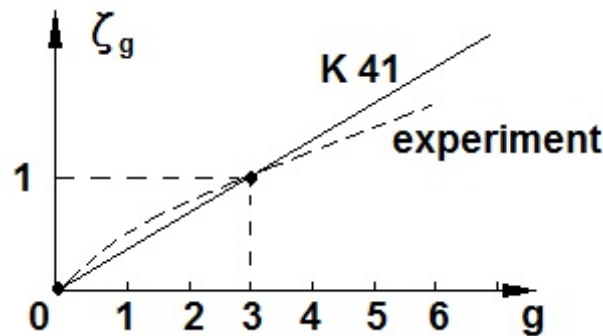
Figure 11.11: Power of the structure function. Experiments versus prediction of Kolmogorov and Obukhov [48].

After the deviation between the K-41 and measurement was documented, Kolmogorov tried to improve his theory. New Kolmogorov theory called as K-62 was published in 1962.
New theory is based on two following assumptions:

- Assumption 1:

$$S_q(l) = < \delta v_l^q > \sim < \varepsilon_l^{q/3} > l^{q/3},$$
$$\zeta_q = \frac{q}{3} + \tau_{q/3} \qquad < \varepsilon_l^q > \sim l^{\tau_q} \tag{11.13}$$

- Assumption 2:

$$P(\varepsilon_l) = ce^{\frac{(\ln \varepsilon - a)^2}{2\sigma_l 2}} \qquad a = \ln \bar{\varepsilon} \qquad \sigma_l^2 = A + \mu \ln(L/l)$$
$$\tau_q = \frac{\mu}{2} q(1 - q) \qquad \varsigma_q = \frac{q}{3} + \frac{\mu}{18} q(3 - q) \qquad < \varepsilon_l^2 > \sim l^{-\mu} \tag{11.14}$$

Unfortunately, various experiments showed later that the second assumption is proved to be wrong.

11.6.1 Exercises

Exercise 1. Calculate the Reynolds averaged values of the time dependent signals

$$u(t) = \cos^2 t,$$

$$u(t) = \sin t,$$

$$u(t) = \begin{cases} 1 - t, & t \leq 1, \\ 0, & t > 1. \end{cases}$$

Solution:

$$\overline{u(t)} = \frac{1}{2},$$

$$\overline{u(t)} = 0,$$

$$\overline{u(t)} = 0.$$

Exercise 2. Find the Reynolds stresses for the isotropic turbulence.

$$\begin{pmatrix} 2 & r_{12} & r_{13} \\ r_{21} & r_{22} & r_{23} \\ r_{31} & r_{32} & r_{33} \end{pmatrix}$$

Solution:

$$\begin{pmatrix} 2 & 0 & 0 \\ 0 & 2 & 0 \\ 0 & 0 & 2 \end{pmatrix}$$

Exercise 3. Calculate the turbulent kinetic energy of the isotropic turbulence, if $r_{33} = 1$
Solution:

$$k = 3/2$$

Exercise 4. Relation between longitudinal autocorrelation function

$$f(r) = \frac{\overline{u_l(x)u_l(x+r)}}{\overline{u_l^2(x)}}$$

and energy density $E(k)$ is given by formula [13]

$$f(r) = \frac{2}{u_l^2} \int_0^\infty E(k)k^{-2}r^{-2}(\frac{\sin kr}{kr} - \cos kr)dk \qquad (11.15)$$

Energy density of the isotropic decaying turbulence is described as $E(k) = k^4 Exp[-k^2]$. Calculate

- longitudinal autocorrelation function f,

- integral length and

- Taylor microscale

for the isotropic decaying turbulence.

Solution:

$$f(r) = \frac{2}{u_l^2} \int\limits_0^\infty E(k)k^{-2}r^{-2}(\frac{\sin kr}{kr} - \cos kr)dk = \qquad (11.16)$$

$$= \frac{2}{u_l^2} \int\limits_0^\infty Exp[-k^2]k^2r^{-2}(\frac{\sin kr}{kr} - \cos kr)dk = \frac{1}{4}\sqrt{\pi}Exp[-r^2/4]$$

$$L = \int\limits_0^\infty f(r)dr = \frac{\pi}{4}$$

$$\lambda = \frac{4}{\pi^{1/4}}$$

Exercise 5. Calculate the probability density function of the time dependent signal

time	0	1	2	3	4	5	6	7
signal	0	0.1	0.9	0.5	0.7	0.5	0.05	0.65

time	8	9	10	11	12	13	14
signal	0.2	0.78	0.43	0.98	0.67	0.92	0.55

using the increment 0.2.

Solution:

signal	0-0.2	0.2-0.4	0.4-0.6	0.6-0.8	0.8-1.0
p.d.f.	3/15	2/15	3/15	4/15	3/15

Exercise 6. The velocity u was measured at N points across the pipe: u_i^k, where $i = 1, N$ and $k = 1, K$ is the time step number. Write a program to calculate the autocorrelation function of u with respect to point $N/2$.

Solution:

$$u_i^{k,\prime} = u_i^k - \overline{u_i}$$

$$\overline{u_i} = \frac{1}{K}\sum_{k=1}^K u_i^k$$

$$R(i, N/2) = \frac{\sum\limits_{k=1}^K u_i^{k,\prime}u_{N/2}^{k,\prime}}{\sum\limits_{k=1}^K u_{N/2}^{k,\prime 2}}$$

Chapter 12

Reynolds Averaged Navier Stokes Equation (RANS)

According to the Reynolds averaging each fluctuating quantity is represented as the sum of the averaged value and its fluctuation:

$$u_x = \bar{u}_x + u'_x; \quad u_y = \bar{u}_y + u'_y; \quad u_z = \bar{u}_z + u'_z \tag{12.1}$$

where the averaged part is defined as:

$$\bar{u}_x = \frac{1}{T}\int_0^T u_x dt; \quad \bar{u}_y = \frac{1}{T}\int_0^T u_y dt; \quad \bar{u}_z = \frac{1}{T}\int_0^T u_z dt \tag{12.2}$$

The Reynolds averaging has the following properties:

- averaged fluctuation is zero:

$$\bar{f}' = 0 \tag{12.3}$$

- double averaged quantity is equal to once averaged one:

$$\bar{\bar{f}} = \bar{f} \tag{12.4}$$

- averaged sum is equal to the sum of averaged:

$$\overline{f + g} = \bar{f} + \bar{g} \tag{12.5}$$

- operators of averaging and differentiation commutate:

$$\overline{\frac{\partial f}{\partial t}} = \frac{\partial \bar{f}}{\partial t}, \quad \overline{\frac{\partial f}{\partial x}} = \frac{\partial \bar{f}}{\partial x} \tag{12.6}$$

- averaged product of two fluctuating quantities is not zero:

$$\overline{f'g'} \neq 0, \quad \overline{\bar{f}g} = \bar{f}\bar{g} \tag{12.7}$$

- averaged product of any averaged quantity and fluctuation is zero:

$$\overline{\bar{f}g'} = \bar{f}\bar{g}' = 0 \tag{12.8}$$

The starting point of the derivation of the RANS equation is the original Navier Stokes (NS) equation:

$$\frac{\partial u_i}{\partial t} + u_j \frac{\partial u_i}{\partial x_j} = F_i + \frac{1}{\rho} \frac{\partial \tau_{ji}}{\partial x_j} \tag{12.9}$$

Here we use the summation convention of Einstein:

$$u_j \frac{\partial u_i}{\partial x_j} = u_1 \frac{\partial u_i}{\partial x_1} + u_2 \frac{\partial u_i}{\partial x_2} + u_3 \frac{\partial u_i}{\partial x_3} \tag{12.10}$$

The NS equation is supplied with the continuity equation, which for the case of incompressible flow takes the form:

$$\frac{\partial u_i}{\partial x_i} = \frac{\partial u_1}{\partial x_1} + \frac{\partial u_2}{\partial x_2} + \frac{\partial u_3}{\partial x_3} = 0 \tag{12.11}$$

Using the continuity equation the convective term is written in the conservative form:

$$u_j \frac{\partial u_i}{\partial x_j} = u_j \frac{\partial u_i}{\partial x_j} + u_i \frac{\partial u_j}{\partial x_j} = \frac{\partial(u_i u_j)}{\partial x_j} \tag{12.12}$$

With (12.12) the NS equation reads

$$\frac{\partial u_i}{\partial t} + \frac{\partial(u_i u_j)}{\partial x_j} = F_i + \frac{1}{\rho} \frac{\partial \tau_{ji}}{\partial x_j} \tag{12.13}$$

This equation is valid for fluctuating quantities represented in Reynolds form (12.1)

$$\frac{\partial(\bar{u}_i + u_i')}{\partial t} + \frac{\partial(\bar{u}_i + u_i')(\bar{u}_j + u_j')}{\partial x_j} = \bar{F}_i + F' + \frac{1}{\rho}\frac{\partial(\bar{\tau}_{ji} + \tau_{ji}')}{\partial x_j} \qquad (12.14)$$

Both r.h.s. and l.h.s. are averaged:

$$\overline{\frac{\partial(\bar{u}_i + u_i')}{\partial t} + \frac{\partial(\bar{u}_i + u_i')(\bar{u}_j + u_j')}{\partial x_j}} = \overline{\bar{F}_i + F' + \frac{1}{\rho}\frac{\partial(\bar{\tau}_{ji} + \tau_{ji}')}{\partial x_j}} \qquad (12.15)$$

Utilization of Reynolds averaging properties results in:

$$\frac{\partial \bar{u}_i}{\partial t} + \frac{\partial(\bar{u}_i\bar{u}_j + \overline{u_i'u_j'})}{\partial x_j} = \bar{F}_i + \frac{1}{\rho}\frac{\partial \bar{\tau}_{ji}}{\partial x_j} \qquad (12.16)$$

Writing the term $\overline{u_i'u_j'}$ on the r.h.s we obtain the Reynolds averaged Navier Stokes equation (RANS). Its unsteady version is called as the unsteady Reynolds averaged NS equation (URANS):

$$\rho\frac{\partial \bar{u}_i}{\partial t} + \rho\frac{\partial \bar{u}_i\bar{u}_j}{\partial x_j} = \rho\bar{F}_i + \frac{\partial}{\partial x_j}(\bar{\tau}_{ji} - \varrho\overline{u_i'u_j'}) \qquad (12.17)$$

There are two important features of URANS in comparison with NS:

- The URANS is written for the averaged quantities, whereas the NS for instantaneous ones,

- The URANS has additional term on the r.h.s. $-\varrho\overline{u_i'u_j'}$ which is called the Reynolds stress R_{ij}.

Generally the Reynolds stress is the matrix with nine terms:

$$R_{ij} = \begin{vmatrix} -\rho\overline{u_x'u_x'} & -\rho\overline{u_x'u_y'} & -\rho\overline{u_x'u_z'} \\ -\rho\overline{u_x'u_y'} & -\rho\overline{u_y'u_y'} & -\rho\overline{u_y'u_z'} \\ -\rho\overline{u_x'u_z'} & -\rho\overline{u_y'u_z'} & -\rho\overline{u_z'u_z'} \end{vmatrix} \qquad (12.18)$$

Due to symmetry condtitions the number of unknown stresses is six. The term $-\varrho\overline{u_i'u_j'}$ is called the stress since it has the same appearance in NS equation as the laminar stress:

$$\tau_{ji} = \rho v\left(\frac{\partial u_i}{\partial x_j} + \frac{\partial u_j}{\partial x_i}\right) - p\delta_{ij} \qquad (12.19)$$

Laminar stress appears due to viscosity effects whereas the Reynolds stress is caused by flow fluctuations. Now the system of four fluid equations (three URANS+ continuity) has ten unknowns: three averaged velocity components $\bar{u}_i$, averaged pressure $\bar{p}$ and six Reynolds stresses. The system of fluid dynamics is not closed. Additional relations are necessary to express the Reynolds stresses through the velocities and pressure. This problem of determination of Reynolds stresses is called as the closure problem of the turbulence. A huge amounts of closure models was developed within the framework of URANS methodology. As said above the URANS methods models the biggest vortices of the flow. The resting scales, which are filtered by the Reynolds avergaing out, are big enough and not universal. This is the reason why the URANS models are not universal. Most of them are of semi empirical character. They are based on submodels with few constants selected for simple canonical flows. Non universality of closure models is the biggest weakness of URANS turbulence modelling.

The majority of URANS models used in engineering are based on the Boussinesq hypothesis which is the formal extension of the Newton hypothesis to turbulent flows. Boussinesq proposed to express the Reynolds stress through the strain rate tensor $S_{ij} = \frac{1}{2}\left(\frac{\partial \bar{u}_j}{\partial x_i} + \frac{\partial \bar{u}_i}{\partial x_j}\right)$ in the form of the Newton hypothesis with the only difference that instead of the kinematic viscosity ν the turbulent viscosity ν_t is used

$$-\rho\overline{u'_i u'_j} = \rho v_t \left(\frac{\partial \bar{u}_j}{\partial x_i} + \frac{\partial \bar{u}_i}{\partial x_j} \right) - \frac{2}{3}\rho\delta_{ij}k \qquad (12.20)$$

In the simplest form for flow along the plate with $\bar{u}_x(y)$ and $\bar{u}_y = \bar{u}_z = 0$ the formula (12.20) reads

$$-\rho\overline{u'_x u'_y} = \rho v_t \frac{d\bar{u}_x}{dy} \qquad (12.21)$$

The last term in (12.20) is introduced to keep the consistency. Indeed the sum of three diagonal terms of the Reynolds matrix is equal to the turbulent kinetic energy $k = \frac{1}{2}\overline{u'_i u'_i}$. Without this term the sum of r.h.s of (12.20) would result in the sum of the diagonal terms of the strain rate matrix $S_{11} + S_{22} + S_{33}$ which is zero due to the continuity equation. It would be wrong result because $k \neq 0$. The turbulent closures (12.20) are referred to as the isotropic because the coefficient v_t is equal for all matrix elements R_{ij}.

While the kinematic viscosity depends on the liquid, the turbulent kinematic viscosity depends on the turbulent state of the flow. According to estimation of Landau the ratio of the turbulent kinematic viscosity to the kinematic one is proportional to the ratio of the Reynolds number to that corresponding to the transition for this type of flow

$$v_t/v \sim Re/Re_{crit} \qquad (12.22)$$

The URANS closure models are subdivided into algebraic and differential ones. The most prominent model amount the algebraic models is the Prandtl model described above. The disadvantages of the algebraic models are:

- they are good only for the simplest flow,

- not suitable for 3D flows,

- not suitable for separation flows,

- turbulent viscosity depends on averaged values of velocities,

- do not consider the flow history.

These disadvantages can be overcome using differential models which are subdividided into one, two and multi equation models. One and two equation models are usually isotropic based on the Boussinesq approach (12.20). Among the one equation models the most modern and efficient is the model of Spalart Allmares (SA model) written for the modified kinematic turbulent viscosity v. The equation for v reads

$$\frac{\partial v}{\partial t} + \bar{u}_j \frac{\partial v}{\partial x_j} = C_{b1}\xi v - C_{w1}f_w\left(\frac{v}{d}\right)^2 + \frac{1}{\sigma}\frac{\partial}{\partial x_k}\left((v+v)\frac{\partial v}{\partial x_k}\right) + \frac{C_{b2}}{\sigma}\frac{dv}{dx_k}\frac{dv}{dx_k}$$
$$(12.23)$$

where

$$C_{b1} = 0,1355, \quad C_{b2} = 0,622, \quad C_{v1} = 7,1, \quad \sigma = 2/3,$$
$$C_{w1} = \frac{C_{b1}}{k^2} + \frac{1 + C_{b2}}{\sigma}, \quad C_{w2} = 0,3, \quad C_{w3} = 2,0, \quad k = 0,41 \tag{12.24}$$

$$f_{v1} = \frac{\chi^3}{\chi^3 + C_{v1}^3}, \quad f_{v2} = \frac{\chi}{1 + \chi f_{v1}}, \quad f_w = g\left[\frac{1 + C_{w3}^6}{g^6 + C_{w3}^6}\right]^{1/6},$$
$$\chi = \upsilon\nu, \quad g = r + C_{w2}(r^6 - r), \quad r = \frac{\upsilon}{\xi k^2 d^2} \tag{12.25}$$

$$\xi = S + \frac{\upsilon}{k^2 d^2} f_{v2}, \quad S = \sqrt{2\Omega_{ij}\Omega_{ij}}, \quad \Omega_{ij} = \frac{1}{2}\left(\frac{\partial \bar{u}_i}{\partial x_j} - \frac{\partial \bar{u}_j}{\partial x_i}\right) \tag{12.26}$$

Within the more advanced $k - \varepsilon$ model the turbulent kinetic energy and the dissipation rate are calculated from the transport equations:

$$\left.\begin{aligned}\frac{\partial k}{\partial t} + \bar{u}_j \frac{\partial k}{\partial x_j} &= \frac{\partial}{\partial x_j}\left(\left(\nu + \frac{\nu_t}{\sigma_k}\right)\frac{\partial k}{\partial x_j}\right) + \tau_{ij}\frac{\partial \bar{u}_i}{\partial x_j} - \varepsilon \\ \frac{\partial \varepsilon}{\partial t} + \bar{u}_j \frac{\partial \varepsilon}{\partial x_j} &= \frac{\partial}{\partial x_j}\left[\left(\nu + \frac{\nu_t}{\sigma_\varepsilon}\right)\frac{\partial \varepsilon}{\partial x_j}\right] + \frac{C_{\varepsilon 1}\varepsilon}{k}\tau_{ij}\frac{\partial \bar{u}_i}{\partial x_j} - \frac{C_{\varepsilon 2}\varepsilon^2}{k}\end{aligned}\right\} \tag{12.27}$$

If k and ε are known the turbulent viscosity ν_t can be found from the dimension analysis, applied to the dissipation rate

$$\varepsilon \approx k^{3/2}/L \tag{12.28}$$

turbulent kinematic viscosity

$$\nu_t = C_\mu \sqrt{k} L \tag{12.29}$$

Here $C_\mu = 0.09$ is the empirical constant. Substitution of (12.28) into (12.29) leads to the sought relation:

$$\nu_t = C_\mu \sqrt{k} L = C_\mu \frac{k^2}{\varepsilon} \tag{12.30}$$

If ν_t is known, the Reynolds stresses can be determined from the Boussinesq approach (12.20).

Chapter 13
Reynolds Stress Model (RSM)

13.1   Derivation of the RSM Equations

13.1.1   Step 1

The $k-th$ Navier-Stokes equation

$$\frac{\partial u_k}{\partial t} + \frac{\partial}{\partial x_j}(u_j u_k) = -\frac{1}{\rho}\frac{\partial p}{\partial x_k} + \frac{1}{\rho}\frac{\partial}{\partial x_j}\tau_{jk} \qquad (13.1)$$

is multiplied with the velocity component u_i

$$u_i\left(\frac{\partial u_k}{\partial t} + \frac{\partial}{\partial x_j}(u_j u_k)\right) = u_i\left(-\frac{1}{\rho}\frac{\partial p}{\partial x_k} + \frac{1}{\rho}\frac{\partial}{\partial x_j}\tau_{jk}\right) \qquad (13.2)$$

The $i-th$ equation is multiplied with $k-th$ velocity component:

$$u_k\left(\frac{\partial u_i}{\partial t} + \frac{\partial}{\partial x_j}(u_j u_i)\right) = u_k\left(-\frac{1}{\rho}\frac{\partial p}{\partial x_i} + \frac{1}{\rho}\frac{\partial}{\partial x_j}\tau_{jk}\right) \qquad (13.3)$$

Resulting equations (13.2) and (13.3) are then sumed:

$$\frac{\partial(\rho u_i u_k)}{\partial t} + \frac{\partial(\rho u_i u_k u_j)}{\partial x_j} = -u_i \frac{\partial p}{\partial x_k} - u_k \frac{\partial p}{\partial x_i} + u_i \frac{\partial \tau_{jk}}{\partial x_j} + u_k \frac{\partial \tau_{ji}}{\partial x_j} \quad (13.4)$$

Substitution of Reynolds decomposition

$$u_i = \bar{u}_i + u'_i, \quad p = \bar{p} + p', \quad \tau_{ji} = \bar{\tau}_{ji} + \tau'_{ji} \quad (13.5)$$

into the equation (13.4) results in

$$\frac{\partial}{\partial t}(\rho \bar{u}_i \bar{u}_k) + \frac{\partial}{\partial t}(\rho \overline{u'_i u'_k}) + \frac{\partial}{\partial x_j}\left(\rho \bar{u}_i \bar{u}_j \bar{u}_k + \rho \bar{u}_i \overline{u'_j u'_k} + \right.$$

$$\left. + \rho \bar{u}_j \overline{u'_i u'_k} + \rho \bar{u}_k \overline{u'_i u'_j} + \rho \overline{u'_i u'_j u'_k} \right) = -\bar{u}_i \frac{\partial \bar{p}}{\partial x_k} - \overline{u'_i \frac{\partial p'}{\partial x_k}} \quad (13.6)$$

$$- \bar{u}_k \frac{\partial \bar{p}}{\partial x_i} - \overline{u'_k \frac{\partial p'}{\partial x_i}} + \bar{u}_i \frac{\partial \overline{\tau_{jk}}}{\partial x_j} + \overline{u'_i \frac{\partial \tau'_{jk}}{\partial x_j}} + \bar{u}_k \frac{\partial \overline{\tau_{ji}}}{\partial x_j} + \overline{u'_k \frac{\partial \tau'_{ji}}{\partial x_j}}$$

13.1.2   Step 2

The $k-th$ Reynolds averaged Navier Stokes equation

$$\frac{\partial \rho \bar{u}_k}{\partial t} + \frac{\partial}{\partial x_j}(\rho \bar{u}_j \bar{u}_k) = -\frac{\partial \bar{p}}{\partial x_k} + \frac{\partial}{\partial x_j}(\bar{\tau}_{jk} - \rho \overline{u'_j u'_k}) \quad (13.7)$$

is multiplied with the $i-th$ component of averaged velocity

$$\bar{u}_i \left(\frac{\partial \rho \bar{u}_k}{\partial t} + \frac{\partial}{\partial x_j}(\rho \bar{u}_j \bar{u}_k) \right) = \bar{u}_i \left(-\frac{\partial \bar{p}}{\partial x_k} + \frac{\partial}{\partial x_j}(\bar{\tau}_{jk} - \rho \overline{u'_j u'_k}) \right) \quad (13.8)$$

Again the $i-th$ Reynolds averaged Navier Stokes equation is multiplied with the $k-th$ component of averaged velocity

$$\bar{u}_k \left(\frac{\partial \rho \bar{u}_i}{\partial t} + \frac{\partial}{\partial x_j}(\rho \bar{u}_j \bar{u}_i) \right) = \bar{u}_k \left(-\frac{\partial \bar{p}}{\partial x_i} + \frac{\partial}{\partial x_j}(\bar{\tau}_{jk} - \rho \overline{u'_j u'_i}) \right) \quad (13.9)$$

The sum of two last equations reads

$$\frac{\partial(\rho \bar{u}_i \bar{u}_k)}{\partial t} + \frac{\partial(\rho \bar{u}_i \bar{u}_k \bar{u}_j)}{\partial x_j} = -\bar{u}_i \frac{\partial \bar{p}}{\partial x_k} - \bar{u}_k \frac{\partial \bar{p}}{\partial x_i} + \bar{u}_i \frac{\partial(\bar{\tau}_{jk} - \rho \overline{u'_j u'_k})}{\partial x_j} + \bar{u}_k \frac{\partial(\bar{\tau}_{ji} - \rho \overline{u'_j u'_i})}{\partial x_j}$$

$$(13.10)$$

13.1.3 Step 3

Subtracting the last equation from (13.6) results in

$$
\frac{\partial}{\partial t}(\rho\overline{u'_i u'_k}) + \frac{\partial}{\partial x_j}(\rho\bar{u}_j\overline{u'_i u'_k}) + \frac{\partial}{\partial x_j}(\rho\overline{u'_i u'_j u'_k}) = -\overline{u'_i\frac{\partial p'}{\partial x_k}} - \overline{u'_k\frac{\partial p'}{\partial x_i}} +
$$
$$
+ \overline{u'_i\frac{\partial \tau'_{jk}}{\partial x_j}} + \overline{u'_k\frac{\partial \tau'_{ji}}{\partial x_j}} - \rho\overline{u'_j u'_k}\frac{\partial \bar{u}_i}{\partial x_j} - \rho\overline{u'_j u'_i}\frac{\partial \bar{u}_k}{\partial x_j}
$$

$$(13.11)$$

Using identities (please prove them)

$$
-\overline{u'_i\frac{\partial p'}{\partial x_k}} - \overline{u'_k\frac{\partial p'}{\partial x_i}} = \overline{p'\left(\frac{\partial u'_i}{\partial x_k} + \frac{\partial u'_k}{\partial x_i}\right)} - \left[\delta_{jk}\frac{\partial}{\partial x_j}(\overline{u'_i p'}) + \delta_{ij}\frac{\partial}{\partial x_j}(\overline{u'_k p'})\right]
$$

$$(13.12)$$

$$
\overline{u'_i\frac{\partial \tau'_{jk}}{\partial x_j}} + \overline{u'_k\frac{\partial \tau'_{ji}}{\partial x_j}} = \mu\left(\overline{u'_i\frac{\partial^2 u'_k}{\partial x_j^2}} + \overline{u'_k\frac{\partial^2 u'_i}{\partial x_j^2}}\right) = \mu\frac{\partial^2}{\partial x_j^2}\overline{u'_i u'_k} - 2\mu\overline{\frac{\partial u'_i}{\partial x_j}\frac{\partial u'_k}{\partial x_j}} \quad (13.13)
$$

we get the Reynolds stress model equation

$$
\frac{\partial}{\partial t}(\rho\overline{u'_i u'_k}) + \frac{\partial}{\partial x_j}(\rho\bar{u}_j\overline{u'_i u'_k}) + \frac{\partial}{\partial x_j}(\rho\overline{u'_i u'_j u'_k}) =
$$
$$
\overline{p'\left(\frac{\partial u'_i}{\partial x_k} + \frac{\partial u'_k}{\partial x_i}\right)} - \left[\delta_{jk}\frac{\partial}{\partial x_j}(\overline{u'_i p'}) + \delta_{ij}\frac{\partial}{\partial x_j}(\overline{u'_k p'})\right] +
$$
$$
+ \mu\frac{\partial^2}{\partial x_j^2}\overline{u'_i u'_k} - 2\mu\overline{\frac{\partial u'_i}{\partial x_j}\frac{\partial u'_k}{\partial x_j}}
$$
$$
- \rho\overline{u'_j u'_k}\frac{\partial \bar{u}_i}{\partial x_j} - \rho\overline{u'_j u'_i}\frac{\partial \bar{u}_k}{\partial x_j}
$$

which can be written in a compact form

$$
\frac{\partial}{\partial t}(\overline{u'_i u'_k}) + \bar{u}_j\frac{\partial}{\partial x_j}(\overline{u'_i u'_k}) = \frac{\partial}{\partial x_j}D_{ik} + R_{ik} + P_{ik} - \varepsilon_{ik} \tag{13.14}
$$

The physical meaning of terms on the r.h.s is as follows

$$
D_{ik} = \nu\frac{\partial(\overline{u'_i u'_k})}{\partial x_j} - \overline{u'_i u'_j u'_k} + \frac{1}{\rho}\overline{(\delta_{jk}u'_i + \delta_{ij}u'_k)p'} \quad \rightarrow \quad \textit{Diffusion} \quad (13.15)
$$

$$
R_{ik} = \frac{1}{\rho}\overline{\left(\frac{\partial u'_i}{\partial x_k} + \frac{\partial u'_k}{\partial x_i}\right)p'} \quad \rightarrow \text{Re } \textit{distribution (energy exchange)} \quad (13.16)
$$

$$
P_{ik} = -\overline{u'_j u'_k}\frac{\partial \bar{u}_i}{\partial x_j} - \overline{u'_j u'_i}\frac{\partial \bar{u}_k}{\partial x_j} \quad \rightarrow \textit{Generation} \quad (13.17)
$$

$$\varepsilon_{ik} = 2v\overline{\frac{\partial u_i'}{\partial x_j}\frac{\partial u_k'}{\partial x_j}} \quad \rightarrow Dissipation \qquad (13.18)$$

13.1.4   Analysis of terms

The diffusion of energy

$$D_{ik} = v\frac{\partial \overline{(u_i'u_k')}}{\partial x_j} - \overline{u_i'u_j'u_k'} + \frac{1}{\rho}\overline{(\delta_{jk}u_i' + \delta_{ij}u_k')p'} \qquad (13.19)$$

is due to

- molecular diffusion, described by the term:

$$v\frac{\partial \overline{(u_i'u_k')}}{\partial x_j} \qquad (13.20)$$

- turbulent diffusion, described by the term:

$$-\overline{u_i'u_j'u_k'} \qquad (13.21)$$

- turbulent diffusion caused by correlation between pressure and velocity fluctuations

$$\frac{1}{\rho}\overline{(\delta_{jk}u_i' + \delta_{ij}u_k')p'} \tag{13.22}$$

The two last terms are <u>unclosed</u>. Here we face with the famous problem noted first by Friedman and <u>Keller</u> (1924): Effort to derive the equations for the second order moments $\overline{u_i'u_k'}$ results in the necessity of determination of new unclosed terms including third order moments $\overline{u_i'u_j'u_k'}$. Using the method proposed by Friedman and Keller in 1924 it is possible to derive equations for moments of arbitrary order. However, the equation for the $m-th$ order will contain unclosed moments of the $m+1-th$ order. Impossibility of obtaining of a closed system of equations for a finite number of moments, known as the Friedman-Keller problem is a direct consequence of the nonlinearity of the Navier Stokes equations.

The also unclosed term

$$R_{ik} = \frac{1}{\rho}\overline{\left(\frac{\partial u_i'}{\partial x_k} + \frac{\partial u_k'}{\partial x_i}\right)p'} \tag{13.23}$$

describes the redistribution of the energy between different tensor components $\overline{u_i'u_k'}$ caused by correlation between the stresses and pressure fluctuations.

The term

$$P_{ik} = -\overline{u_j'u_k'}\frac{\partial \bar{u}_i}{\partial x_j} - \overline{u_j'u_i'}\frac{\partial \bar{u}_k}{\partial x_j} \tag{13.24}$$

is responsible for the energy generation, i.e. the transport of the energy transfer from averaged (mean) flow to oscillating flow (fluctuations). And, finally,

$$\varepsilon_{ik} = 2v\overline{\frac{\partial u_i'}{\partial x_j}\frac{\partial u_k'}{\partial x_j}} \tag{13.25}$$

is the dissipation. This unclosed term is responsible for the transformation of the turbulent kinetic energy into the inner energy of the flow.
RSM model based on equations (13.14) is used to determine the Reynolds stresses from the transport equations. It is not based on the Boussinesq approach and takes the anisotropy of stresses into account. This model is the best one among RANS models.

Chapter 14

Equations of the k - ε Model

14.1 Derivation of the k-Equation

According to definition

$$k = \overline{u'_k u'_k / 2} \tag{14.1}$$

Assuming $i = k$ in the Reynolds stress model equations (13.14)

$$\frac{\partial}{\partial t}\overline{(u'_i u'_k)} + \bar{u}_j \frac{\partial}{\partial x_j}\overline{(u'_i u'_k)} = \frac{\partial}{\partial x_j}D_{ik} + R_{ik} + P_{ik} - \varepsilon_{ik} \tag{14.2}$$

ans summing equations for k=1,2 and 3 we obtain the transport equations for the total kinetic energy k:

$$\frac{\partial k}{\partial t} + \bar{u}_j \frac{\partial k}{\partial x_j} = \frac{\partial}{\partial x_j}D_s + P - \varepsilon_S \tag{14.3}$$

where

$$D_S = \nu \frac{\partial k}{\partial x_j} + \frac{1}{\rho}\delta_{jk}\overline{u'_k p'} - \overline{u'_j k'}, \quad k' = u'_k u'_k / 2 \qquad \textit{Diffusion} \tag{14.4}$$

$$P = -\overline{u'_j u'_k}\frac{\partial \bar{u}_k}{\partial x_j} \qquad \textit{Generation} \tag{14.5}$$

$$\varepsilon_S = \nu \overline{\frac{\partial u'_k}{\partial x_j}\frac{\partial u'_k}{\partial x_j}} \qquad \textit{Dissipation (Pseudodissipation)} \tag{14.6}$$

The relation between the true and pseudodissipation is

$$\varepsilon = \frac{\nu}{2}\overline{\left(\frac{\partial u'_k}{\partial x_j} + \frac{\partial u'_j}{\partial x_k}\right)^2} \approx \varepsilon_S + \frac{\partial}{\partial x_j}\nu\frac{\partial}{\partial x_k}\overline{u'_j u'_k} \tag{14.7}$$

For large Reynolds numbers the true dissipation and the pseudodissipation are equal.

$$\varepsilon \approx \varepsilon_S \tag{14.8}$$

More precise analysis shows that

$$\varepsilon - \varepsilon_S \approx Re_t^{-1} \tag{14.9}$$

where

$$\text{Re}_t = \sqrt{k}L/\nu \tag{14.10}$$

Two unknown terms in the diffusion

$$D_S = \nu \frac{\partial k}{\partial x_j} + \frac{1}{\rho}\delta_{jk}\overline{u'_k p'} - \overline{u'_j k'} \tag{14.11}$$

are determined by the gradient assumption

$$\frac{1}{\rho}\delta_{jk}\overline{u'_k p'} - \overline{u'_j k'} = \frac{\nu_t}{\sigma_k}\frac{\partial k}{\partial x_j} \tag{14.12}$$

where σ_k is an empirical constant. Dissipation is determined by the energy containing motion using the formula of Prandtl- Kolmogorov

$$\varepsilon_s = C_D k^{3/2}/L \tag{14.13}$$

The Reynolds stresses are seeking in form proposed by Boussinesq:

$$-\rho\overline{u'_i u'_j} = \rho\nu_t\left(\frac{\partial \bar{u}_j}{\partial x_i} + \frac{\partial \bar{u}_i}{\partial x_j}\right) - \frac{2}{3}\rho\delta_{ij}k \tag{14.14}$$

Substitution of all these approximations into the equation (14.3) results in the k-Equation

$$\frac{\partial k}{\partial t} + \bar{u}_j \frac{\partial k}{\partial x_j} = \frac{\partial}{\partial x_j}\left[\left(\nu + \frac{\nu_t}{\sigma_k}\right)\frac{\partial k}{\partial x_j}\right] + \nu_t\left(\frac{\partial \bar{u}_j}{\partial x_i} + \frac{\partial \bar{u}_i}{\partial x_j}\right)\frac{\partial \bar{u}_j}{\partial x_i} - C_D \frac{k^{3/2}}{L} \quad (14.15)$$

14.2 Derivation of the ε-Equation

The Navier Stokes equation

$$\frac{\partial u_k}{\partial t} + u_j \frac{\partial u_k}{\partial x_j} = -\frac{1}{\rho}\frac{\partial p}{\partial x_k} + \frac{1}{\rho}\frac{\partial \tau_{jk}}{\partial x_j} \quad (14.16)$$

is differentiated and multiplied with the derivative $\frac{\partial u_i'}{\partial x_k}$

$$\frac{\partial}{\partial x_k}\left\{\frac{\partial u_i}{\partial t} + u_j \frac{\partial u_i}{\partial x_j} = -\frac{1}{\rho}\frac{\partial p}{\partial x_i} + \frac{1}{\rho}\frac{\partial \tau_{ji}}{\partial x_j}\right\}\frac{\partial u_i'}{\partial x_k} \quad (14.17)$$

and then it is averaged. The following identities are used in transformations:

$$\overline{\frac{\partial}{\partial x_k}\left(\frac{\partial u_i}{\partial t}\right)\frac{\partial u_i'}{\partial x_k}} = \overline{\frac{\partial}{\partial t}\left(\frac{\partial(\bar{u}_i + u_i')}{\partial x_k}\right)\frac{\partial u_i'}{\partial x_k}} = \overline{\frac{\partial}{\partial t}\left(\frac{\partial u_i'}{\partial x_k}\right)\frac{\partial u_i'}{\partial x_k}} =$$
$$= \frac{1}{2}\frac{\partial}{\partial t}\overline{\frac{\partial u_i'}{\partial x_k}\frac{\partial u_i'}{\partial x_k}} = \frac{1}{2\nu}\frac{\partial \varepsilon_s}{\partial t} \quad (14.18)$$

$$\overline{\frac{\partial}{\partial x_k}\left\{u_j\frac{\partial u_i}{\partial x_j}\right\}\frac{\partial u_i'}{\partial x_k}} = \overline{\frac{\partial}{\partial x_k}\left\{\bar{u}_j\frac{\partial \bar{u}_i}{\partial x_j}\right\}\frac{\partial u_i'}{\partial x_k}} + \overline{\frac{\partial}{\partial x_k}\left\{u_j'\frac{\partial \bar{u}_i}{\partial x_j}\right\}\frac{\partial u_i'}{\partial x_k}} +$$
$$+ \overline{\frac{\partial}{\partial x_k}\left\{\bar{u}_j\frac{\partial u_i'}{\partial x_j}\right\}\frac{\partial u_i'}{\partial x_k}} + \overline{\frac{\partial}{\partial x_k}\left\{u_j'\frac{\partial u_i'}{\partial x_j}\right\}\frac{\partial u_i'}{\partial x_k}} \quad (14.19)$$

$$\overline{\frac{\partial}{\partial x_k}\left\{\bar{u}_j\frac{\partial u_i'}{\partial x_j}\right\}\frac{\partial u_i'}{\partial x_k}} = \frac{\partial \bar{u}_j}{\partial x_k}\overline{\frac{\partial u_i'}{\partial x_j}\frac{\partial u_i'}{\partial x_k}} + \bar{u}_j\overline{\frac{\partial^2 u_i'}{\partial x_j \partial x_k}\frac{\partial u_i'}{\partial x_k}} =$$
$$= \frac{\partial \bar{u}_i}{\partial x_k}\overline{\frac{\partial u_i'}{\partial x_j}\frac{\partial u_i'}{\partial x_k}} + \frac{1}{2}\bar{u}_j\frac{\partial}{\partial x_j}\overline{\frac{\partial u_i'}{\partial x_k}\frac{\partial u_i'}{\partial x_k}} =$$
$$= \frac{\partial \bar{u}_i}{\partial x_k}\overline{\frac{\partial u_i'}{\partial x_j}\frac{\partial u_i'}{\partial x_k}} + \frac{1}{2\nu}\bar{u}_j\frac{\partial}{\partial x_j}\varepsilon_s \quad (14.20)$$

$$\overline{\frac{\partial}{\partial x_k}\left\{u'_j\frac{\partial u'_i}{\partial x_j}\right\}\frac{\partial u'_i}{\partial x_k}} = \overline{\frac{\partial u'_j}{\partial x_k}\frac{\partial u'_i}{\partial x_j}\frac{\partial u'_i}{\partial x_k}} + \overline{u'_j\frac{\partial^2 u'_i}{\partial x_j\partial x_k}\frac{\partial u'_i}{\partial x_k}} =$$

$$= \overline{\frac{\partial u'_j}{\partial x_k}\frac{\partial u'_i}{\partial x_j}\frac{\partial u'_i}{\partial x_k}} + \frac{1}{2}\frac{\partial}{\partial x_j}\overline{u'_j\cdot\frac{\partial u'_i}{\partial x_k}\frac{\partial u'_i}{\partial x_k}} = \qquad (14.21)$$

$$= \overline{\frac{\partial u'_j}{\partial x_k}\frac{\partial u'_i}{\partial x_j}\frac{\partial u'_i}{\partial x_k}} + \frac{1}{2\nu}\frac{\partial}{\partial x_j}\overline{u'_j\varepsilon_s}$$

$$\overline{\frac{\partial}{\partial x_k}\left\{u'_j\frac{\partial \bar{u}_i}{\partial x_j}\right\}\frac{\partial u'_i}{\partial x_k}} = \frac{\partial \bar{u}_i}{\partial x_j}\overline{\frac{\partial u'_j}{\partial x_k}\frac{\partial u'_i}{\partial x_k}} + \frac{\partial^2 \bar{u}_i}{\partial x_k\partial x_j}\overline{u'_j\frac{\partial u'_i}{\partial x_k}} -$$

$$-\frac{1}{\varrho}\overline{\frac{\partial p}{\partial x_i}\frac{\partial u'_i}{\partial x_k}} = -\frac{1}{\varrho}\overline{\frac{\partial p'}{\partial x_i}\frac{\partial u'_i}{\partial x_k}} \qquad (14.22)$$

$$\frac{1}{\varrho}\overline{\frac{\partial}{\partial x_k}\left(\frac{\partial}{\partial x_j}\left(\bar{\tau}_{ji}+\tau'_{ji}\right)\right)\frac{\partial u'_i}{\partial x_k}} = \frac{1}{\varrho}\overline{\frac{\partial}{\partial x_k}\left(\frac{\partial}{\partial x_j}\tau'_{ji}\right)\frac{\partial u'_i}{\partial x_k}} \qquad (14.23)$$

$$\frac{\partial}{\partial x_j}\tau'_{ji} = \frac{\partial}{\partial x_j}\left(\mu\left(\frac{\partial u'_i}{\partial x_j}+\frac{\partial u'_j}{\partial x_i}\right)\right) = \mu\frac{\partial^2 u'_i}{\partial x_j\partial x_j} \qquad (14.24)$$

$$\frac{1}{\varrho}\overline{\frac{\partial}{\partial x_k}\left(\frac{\partial}{\partial x_j}\tau'_{ji}\right)\frac{\partial u'_i}{\partial x_k}} = \nu\overline{\frac{\partial}{\partial x_k}\left(\frac{\partial^2 u'_i}{\partial x_j\partial x_j}\right)\frac{\partial u'_i}{\partial x_k}} = \nu\overline{\frac{\partial}{\partial x_j\partial x_j}\left(\frac{\partial u'_i}{\partial x_k}\right)\frac{\partial u'_i}{\partial x_k}} =$$

$$= \nu\frac{\partial}{\partial x_j}\left\{\frac{1}{2}\frac{\partial}{\partial x_j}\overline{\frac{\partial u'_i}{\partial x_k}\frac{\partial u'_i}{\partial x_k}}\right\} - \nu\overline{\frac{\partial^2 u'_i}{\partial x_j\partial x_k}\frac{\partial^2 u'_i}{\partial x_j\partial x_k}}$$

$$(14.25)$$

This gives:

$$\frac{\partial \varepsilon_s}{\partial t} + \bar{u}_j\frac{\partial \varepsilon_s}{\partial x_j} = \frac{\partial}{\partial x_j}D_\varepsilon + P_\varepsilon - \varepsilon_\varepsilon \qquad (14.26)$$

where

$$D_\varepsilon = \nu\frac{\partial \varepsilon_s}{\partial x_j} - \overline{u'_j\varepsilon'_s} - 2\frac{\nu}{\rho}\overline{\frac{\partial u'_i}{\partial x_k}\frac{\partial p'}{\partial x_i}} \qquad (14.27)$$

$$P_\varepsilon = -2\nu\overline{u'_j\frac{\partial u'_i}{\partial x_k}}\frac{\partial^2 \bar{u}_i}{\partial x_j\partial x_k} - 2\nu\left(\overline{\frac{\partial u'_i}{\partial x_k}\frac{\partial u'_j}{\partial x_k}}\frac{\partial \bar{u}_i}{\partial x_j} + \overline{\frac{\partial u'_i}{\partial x_j}\frac{\partial u'_i}{\partial x_k}}\frac{\partial \bar{u}_i}{\partial x_k}\right)$$

$$-2\nu\overline{\frac{\partial u'_i}{\partial x_j}\frac{\partial u'_j}{\partial x_k}\frac{\partial u'_i}{\partial x_k}} \qquad (14.28)$$

$$\varepsilon_\varepsilon = 2\nu^2\overline{\frac{\partial^2 u'_i}{\partial x_j\partial x_k}\frac{\partial^2 u'_i}{\partial x_j\partial x_k}}, \quad \varepsilon'_s = \nu\frac{\partial u'_i}{\partial x_k}\frac{\partial u'_i}{\partial x_k} \qquad (14.29)$$

The terms on the r.h.s. were approximated according to the following formula:

$$\frac{\partial}{\partial x_j} D_\varepsilon = \frac{\partial}{\partial x_j}\left[\left(v + \frac{v_T}{\sigma_\varepsilon}\right)\frac{\partial \varepsilon}{\partial x_j}\right]; P_\varepsilon = \frac{C_{\varepsilon 1}\varepsilon}{k}\tau_{ij}\frac{\partial \bar{u}_i}{\partial x_j}; \varepsilon_\varepsilon = \frac{C_{\varepsilon 2}\varepsilon^2}{k} \qquad (14.30)$$

Constants are taken from planar jet and mixing layer:

$$C_{\varepsilon 1} = 1.44, \quad C_{\varepsilon 2} = 1.92, \quad \sigma_k = 1, \quad \sigma_\varepsilon = 1.3 \qquad (14.31)$$

Hereby the full closed system of the $k - \varepsilon$ model reads:

$$\left.\begin{aligned}
\frac{\partial k}{\partial t} + \bar{u}_j \frac{\partial k}{\partial x_j} &= \frac{\partial}{\partial x_j}\left(\left(v + \frac{v_t}{\sigma_k}\right)\frac{\partial k}{\partial x_j}\right) + \tau_{ij}\frac{\partial \bar{u}_i}{\partial x_j} - \varepsilon \\
\frac{\partial \varepsilon}{\partial t} + \bar{u}_j \frac{\partial \varepsilon}{\partial x_j} &= \frac{\partial}{\partial x_j}\left[\left(v + \frac{v_t}{\sigma_\varepsilon}\right)\frac{\partial \varepsilon}{\partial x_j}\right] + \frac{C_{\varepsilon 1}\varepsilon}{k}\tau_{ij}\frac{\partial \bar{u}_i}{\partial x_j} - \frac{C_{\varepsilon 2}\varepsilon^2}{k}
\end{aligned}\right\} \qquad (14.32)$$

Under assumption that the generation of the turbulent energy equals to the its dissipation (the turbulence is in equilibrium, turbulent scales are in the inertial range) Kolmogorov and Prandtl derived the relation between the kinetic energy, the dissipation rate and the integral lengths L:

$$\varepsilon \approx \frac{k^{3/2}}{L} \qquad (14.33)$$

From the dimension analysis

$$v_t = C_\mu \sqrt{k} L \tag{14.34}$$

follows

$$v_t = C_\mu \sqrt{k} L = C_\mu \frac{k^2}{\varepsilon} \tag{14.35}$$

As soon as k and ε are known the turbulent kinematic viscosity v_t is computed from (14.35) and Reynolds stresses can be calculated from the Boussinesq hypothesis and then substituted into the Reynolds averaged Navier Stokes equations. The problem is mathematically closed.

The $k - \varepsilon$ model is the classical approach, which is very accurate at large Re numbers. At small Re number, for instance close to the wall, the approximations used in derivation of $k - \varepsilon$ model equations are not valid. To overcome this disadvantage various low Reynolds $k - \varepsilon$ models were proposed.

14.3 Method of wall functions

Basic relations of $k - \varepsilon$ model were derived under assumption that the local turbulent Reynolds number $Re_t = \sqrt{k} L/v$ is very high. This is not the case in the wall flow. Due to damping effect of the wall, the velocity pulsations and the turbulent kinetic energy are small. Application of the $k - \varepsilon$ model is not valid. An efficient solution of this problem was proposed by Spalding who developed the method of wall functions. The wall function is an analytical representation of the solution close to the wall which is matched with the numerical solution far from the wall. Below we derive basic relations of the wall function method following to the textbook [15].

It is assumed that the turbulence is in equilibrium, i.e. $P = \varepsilon$:

$$P = -\overline{u'_j u'_k} \frac{\partial \bar{u}_k}{\partial x_j} = \varepsilon$$

Let us consider two dimensional flow along a plate:

$$P = -\overline{u'_x u'_y} \frac{\partial \bar{u}_x}{\partial y} = v_t \left(\frac{\partial \bar{u}_x}{\partial y} \right)^2 = \varepsilon \tag{14.36}$$

The derivative $\left(\frac{\partial \bar{u}_x}{\partial y} \right)$ can be expressed from the mixing length model of Prandtl:

$$v_t = l^2 \left(\frac{\partial \bar{u}_x}{\partial y} \right) \Rightarrow \left(\frac{\partial u_x}{\partial y} \right) = v_t / l^2 \tag{14.37}$$

144

From analysis of dimension we obtain

$$\nu_t = c_\mu k^{1/2} L \qquad (14.38)$$

Using the Kolmogorov-Prandtl estimation $\varepsilon \sim k^{3/2}/L$ we get

$$\nu_t = \frac{c_\mu k^2}{\varepsilon} \qquad (14.39)$$

From (14.36) and (14.37) it follows

$$\nu_t = l^{4/3} \cdot \varepsilon^{1/3}$$

and

$$\varepsilon = c_\mu^{3/4} k^{3/2}/l$$

From (14.36) and (14.39) we have:

$$\frac{\partial \bar{u}_x}{\partial y} = \left(\frac{\varepsilon}{\nu_t}\right)^{1/2} = \left(\frac{\varepsilon^2}{c_\mu k^2}\right)^{1/2} = \frac{\varepsilon}{c_\mu^{1/2} k}$$

for wall stress:

$$\tau_w = \mu_t \frac{\partial \bar{u}_x}{\partial y} = \varrho \nu_t \frac{\varepsilon}{c_\mu^{1/2} k} =$$

$$= \varrho \frac{c_\mu k^2}{\varepsilon} \frac{\varepsilon}{c_\mu^{1/2} k} = \varrho c_\mu^{1/2} k$$

and kinetic energy:

$$k = \frac{\tau_w}{\varrho c_\mu^{1/2}}$$

Let y_p be the ordinate of the first grid node near the wall.
Using approximation of Prandtl for l we obtain the dissipation rate at y_p:

$$\varepsilon_p = c_\mu^{3/4} k_p^{3/2}/(\kappa y_p) \qquad (14.40)$$

and turbulent kinetic energy

$$k_p = \frac{\tau_w}{\varrho c_\mu^{1/2}}$$

τ_w can be found from the assumption that the first node is in the logarithmic range:

$$
\begin{aligned}
\frac{u_x}{u_\tau} &= \frac{1}{x}\ln E y^+ \\
u_\tau &= \frac{x\bar{u}_{xp}}{\ln E y_p^+} \\
\sqrt{\frac{\tau_w}{\varrho}}\cdot\sqrt{\frac{\tau_w}{\varrho}} &= \frac{x\bar{u}_{xp}}{\ln E y_p^+}\cdot k_p^{1/2}c_\mu^{1/4} \\
\tau_w &= \frac{\varrho x\bar{u}_{xp}k_p^{1/2}c_\mu^{1/4}}{\ln E y_p^+}
\end{aligned}
\tag{14.41}
$$

Values ε_p (14.40) and τ_w (14.41) are used within finite volume method when the $k-\varepsilon$ equations are written for the volumes adjacent to the wall. For instance the generation term is calculated as

$$
\int P\,dxdy = \int \tau_{ij}\frac{\partial\bar{u}}{\partial y}dxdy = \int \tau_w\frac{\partial\bar{u}}{\partial y}dxdy = \tau_w\Delta x u_{xp}
\tag{14.42}
$$

Chapter 15

Large Eddy Simulation (LES)

15.1 LES filtering

Within the LES all vortices are subdivided into large resolved vortices and fine modelled subgrid vortices. The border between vortices should lie within the inertial range. The separation of fine scale motions (small fine vortices) from large ones is done using the spatial filtering. Let φ be any stochastic function which is represented as the sum of filtered part and fluctuation:

$$\varphi = \tilde{\varphi} + \varphi'$$

where the filtered part is defined as

$$\tilde{\varphi}(\vec{x}, t) = \int_{-\infty}^{\infty} \int_{-\infty}^{\infty} \int_{-\infty}^{\infty} \varphi(\vec{x} - \vec{s}, t) F(\vec{s}) d\vec{s}$$

Here $F(\vec{s})$ is the filtering function, satisfying the condition

$$\int_{-\infty}^{\infty} \int_{-\infty}^{\infty} \int_{-\infty}^{\infty} F(\vec{s}) d\vec{s} = 1$$

Three different filtering functions shown in Fig. 1: ideal filter, Gauss filter and top hat filter. Ideal filter is applied in Fourier space. High frequencies are cut off. Low frequencies are simulated directly. The top hat filter is some kind of smoothing applied in physical space. The simplest case is smoothing over three neighboring points

$$\tilde{\varphi}_i = \frac{1}{b}(\varphi_{i-1} + a\varphi_i + \varphi_{i+1})$$

where $b = 2 + a$.

15.1.1 Properties of filtering

The spatial filtering and Reynolds averaging are both filtering operations. LES spatial filtering has properties which differ from these of Reynolds averaging. First, the spatialy averaged quantity is not zero. Double filtering is not equal once filtering:

$$\widetilde{\varphi'} \neq 0, \quad \tilde{\tilde{\varphi}} \neq \tilde{\varphi},$$

Both conditions are compatible because

$$\widetilde{\varphi'} = \widetilde{\varphi - \tilde{\varphi}} = \tilde{\varphi} - \tilde{\tilde{\varphi}} \neq 0$$

147
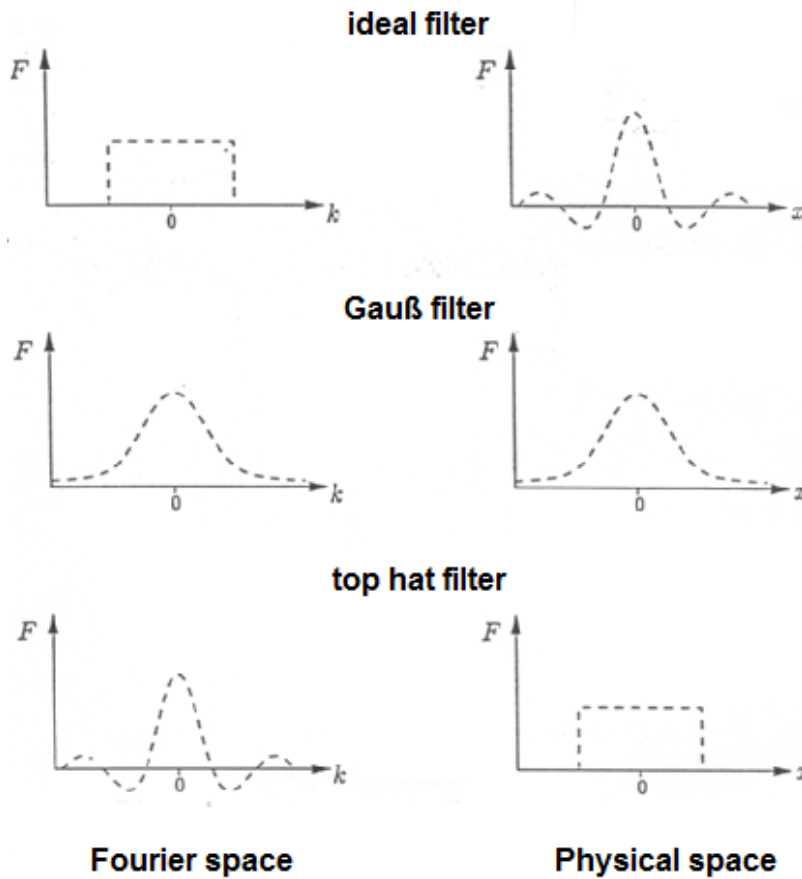
Figure 15.1: Different filtering functions used in LES.

Other important properties are similar to these of RANS averaging:

- Averaged sum of two quantities is equal to the sum of averaged quantities:

$$\widetilde{\varphi + g} = \tilde{\varphi} + \tilde{g}$$

- Filtering operator commutes with the differentiation operator, if filtering is homogeneous:

$$\widetilde{\frac{\partial \varphi}{\partial t}} = \frac{\partial \tilde{\varphi}}{\partial t} \qquad \widetilde{\frac{\partial \varphi}{\partial x_j}} = \frac{\partial \tilde{\varphi}}{\partial x_j}$$

A very important relation which is the consequence of these properties is

$$\widetilde{\varphi \phi} = \widetilde{\tilde{\varphi}\tilde{\phi}} + \widetilde{\tilde{\varphi}\phi'} + \widetilde{\tilde{\phi}\varphi'} + \widetilde{\varphi'\phi'}$$

In the case of Reynolds averaging only the first and the last terms remain. The properties of large and small scale motions are shown in the table 15.1.

Large scale motion	Small scale motion
Generated by mean flow	Generated by large scale structures
Depends on the flow geometry	Universal
Regular	Stochastic
Deterministic description	Stochastic description
Heterogeneous	Homogeneous
Anisotrop	Isotrop
Exists long time	Exists short time
Diffusive	Dissipative
Modelling is complicated	Easy to model

Table 15.1: Properties of large and small scale motions

A very important conclusion from this table is the fact that the small scale motion is universal. Therefore one can expect that the models describing the small scale motion in contrast to RANS models are also universal.

15.2   LES equations

The governing equations of LES are derived from the Navier Stokes equation

$$\frac{\partial}{\partial t}(\rho u_i) + \frac{\partial}{\partial x_j}(\rho u_i u_j) = \frac{\partial}{\partial x_j}\left[\rho v\left(\frac{\partial u_j}{\partial x_i} + \frac{\partial u_i}{\partial x_j}\right)\right] - \frac{\partial p}{\partial x_i} + \rho g_i \qquad (15.1)$$

Application of the filter operation to (15.1) results in

$$\overline{\frac{\partial}{\partial t}(\rho u_i) + \frac{\partial}{\partial x_j}(\rho u_i u_j)} = \overline{\frac{\partial}{\partial x_j}\left[\rho \nu \left(\frac{\partial u_j}{\partial x_i} + \frac{\partial u_i}{\partial x_j}\right)\right] - \frac{\partial p}{\partial x_i} + \rho g_i}$$

Averaged sum is equal to the sum of averaged terms:

$$\widetilde{\frac{\partial}{\partial t}(\rho u_i)} + \widetilde{\frac{\partial}{\partial x_j}(\rho u_i u_j)} = \widetilde{\frac{\partial}{\partial x_j}\left[\rho \nu \frac{\partial u_i}{\partial x_j}\right]} - \widetilde{\frac{\partial p}{\partial x_i}} + \widetilde{\rho g_i} \qquad (15.2)$$

Introducing the term

$$\tau_{ij}^{SGS} = \widetilde{u_i u_j} - \tilde{u}_i \tilde{u}_j$$

the equation (15.2) is rewritten in the final form

$$\frac{\partial}{\partial t}(\rho \tilde{u}_i) + \frac{\partial}{\partial x_j}(\rho \tilde{u}_i \tilde{u}_j) = \frac{\partial}{\partial x_j}\left[\rho \nu \frac{\partial \tilde{u}_i}{\partial x_j} - \rho \tau_{ij}^{SGS}\right] - \frac{\partial \tilde{p}}{\partial x_i} + \rho g_i$$

The term $\tau_{ij}^{SGS} = \widetilde{u_i u_j} - \tilde{u}_i \tilde{u}_j$ is the subgrid stress (SGS) which considers the effect of small fine vortices on large scale motion directly resolved on the grid.

15.3   Smagorinsky model

Note that the fine scale vortices are not resolved. They filtered out by the filtering operation. The effect of these vortices is taken by the term τ_{ij}^{SGS} into account. Since the small vortices are not modeled, the subgrid stress are calculated using phenomenological models. The most recent phenomenological model was proposed by Smagorinsky in 1963. The Smagorinsky model is just the extension of the Boussinesq approach

$$\tau_{ij} - \frac{1}{3}\tau_{kk}\delta_{ij} \approx -2\nu_t \bar{S}_{ij},$$

Smagorinsky introduced the subgrid viscosity ν_{SGS} instead of the turbulent kinematic viscosity

$$\tau_{ij}^{SGS} - \frac{1}{3}\tau_{kk}^{SGS}\delta_{ij} \approx -2\nu_{SGS}\tilde{S}_{ij},$$

Expression for the subgrid viscosity was obtained by Smagorinsky with the use of idea taken from the Prandtl mixing length theory. According to Prandtl, the turbulent kinematic viscosity is proportional to the mixing length squared and the velocity gradient close to the wall

$$\nu_t = l^2 |\frac{d\bar{u}_x}{dy}|$$

According to Smagorinsky, the subgrid viscosity is proportional to the magnitude of the strain rate tensor S_{ij} and to a certain length l_S squared

$$\nu_{SGS} = l_S^2 |\tilde{S}_{ij}|, \qquad |\tilde{S}_{ij}| = \sqrt{2\tilde{S}_{ij}\tilde{S}_{ij}}$$

Where

$$\tilde{S}_{ij} = \frac{1}{2}\left(\frac{\partial \tilde{u}_i}{\partial x_j} + \frac{\partial \tilde{u}_j}{\partial x_i}\right)$$

The length l_S is assumed to be proportional to the mesh size

$$l_S = C_S \Delta$$

where C_S is the constant of Smagorinsky.

The Smagorinsky constant was estimated first by Lilly. The main assumption of the Lilly analysis is the balance between generation

$$P_r = -\tau_{ij}\tilde{S}_{ij} = 2\nu_t\tilde{S}_{ij}\tilde{S}_{ij} = \nu_t|\tilde{S}_{ij}|^2$$

and dissipation of the turbulent kinetic energy

$$\varepsilon = \bar{P} = \overline{\nu_t|\tilde{S}_{ij}|^2} = l_S^2\overline{|\tilde{S}_{ij}|^3} \tag{15.3}$$

Lilly estimated the strain rate tensor magnitude for Kolmogorov spectrum

$$\overline{\tilde{S}^2} \approx 7C\varepsilon^{2/3}\Delta^{-4/3}$$

Substitution of the last formula into (15.3) results in:

$$l_S = \frac{\Delta}{(7C)^{3/4}}\left(\frac{\overline{\tilde{S}^2}^{3/2}}{\overline{\tilde{S}^3}}\right)^{1/2}$$

Assuming additionally that $\overline{\tilde{S}^2}^{3/2} \approx \overline{\tilde{S}^3}$, the length l_S and the Smagorinsky constant are expressed through the Kolmogorov constant $C = 1.5$:

$$C_S = \frac{l_S}{\Delta} = \frac{1}{(7C)^{3/4}} \approx 0.17$$

The Smagorinsky constant 0.17 is derived analytically with a few strong assumptions. The experience shows that numerical results agree with measurements much better if a reduced value of the Smagorinsky constant is used. Common values are 0.065 and 0.1.

Advantages and disdvantages of the Smagorinsky model are summarized in the table 19.1.

Advantages	Disadvantages
Simple	Laminar flow is not modelled
Low computational costs	Constant of Smagorinsky is constant in time and space
Stable	Actually, the constant is chosen arbitrarily depending on the problem under consideration
Good accuracy in ideal conditions	Sensible to grid
	Purely dissipativ
	Damping of pulsation is too strong

Table 15.2: Advantages and disadvantages of the Smagorinsky model

We finish this section with a very important comment:

- the LES models are consistent when the resolution increases, i.e. $\Delta \to 0$.

Indeed, if the resolution is increased, $\Delta \to 0$, the SGS stresses disappear. The LES equation is passed to the original Navier Stokes equations. The LES simulation becomes the DNS simulation if $\Delta \to 0$. On the contrary, the URANS simulation is not consistent when $\Delta \to 0$. The Reynolds stresses don't disappear if the resolution is increased $\Delta \to 0$. The turbulence is then twice resolved.
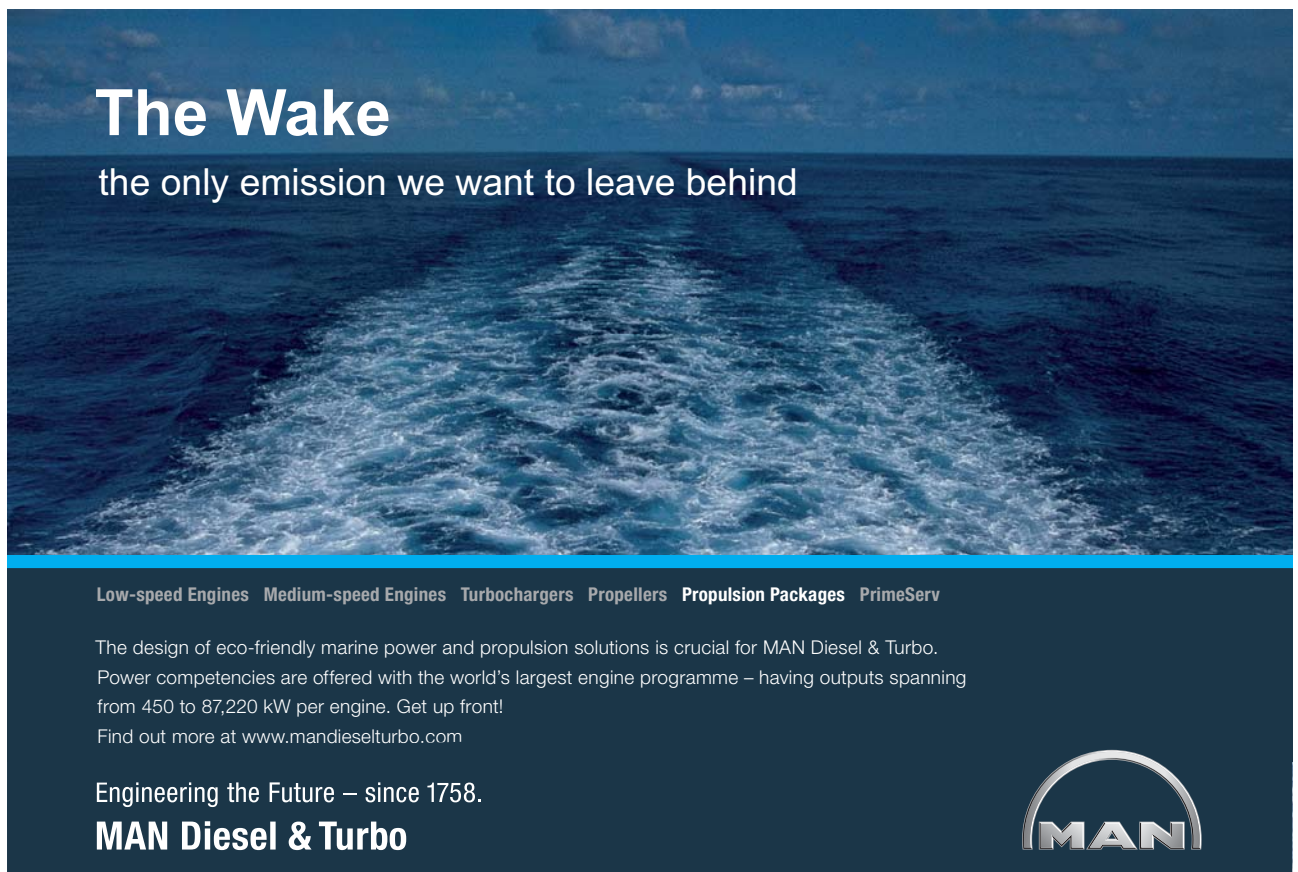
15.4 Model of Germano (Dynamic Smagorinsky Model)

The classical model of Smagorinsky with the parameter C_S being constant for the whole computational domain is proved to be very diffusive. Germano proposed to calculate the Smagorinsky constant C_S being variable both in space and in time, i.e. $C_S = C_S(\mathbf{x}, t)$. The constant is determined using the dynamic procedure which is then referred to as the Dynamic Smagorinsky Model (DSM).
According to the definition the subgrid stress is

$$\tau_{ij}^{SGS} = \widetilde{\tilde{u}_i \tilde{u}_j} - \tilde{u}_i \tilde{u}_j \tag{15.4}$$

Germano introduces the double filtering or the test filtering designated as $\widehat{u} = \hat{\tilde{u}}$. Here the tilde symbol means the first filtering with filter width Δ whereas the hat symbol stands for the second filtering with filter width $\sim 2\Delta$. The symbol means the resulting double filtering. Using the definition (15.4) we can write

$$T_{ij}^{test} = \widehat{u_i u_j} - \widehat{u}_i \widehat{u}_j = \widehat{\widetilde{u_i u_j}} - \hat{\tilde{u}}_i \hat{\tilde{u}}_j \tag{15.5}$$

Filtration of (15.4) results in

$$\hat{\tau}_{ij}^{SGS} = \widehat{\widetilde{u_i u_j}} - \widehat{\tilde{u}_i \tilde{u}_j} \tag{15.6}$$

Subtracting (15.6) from (15.5) yields

$$T_{ij}^{test} - \hat{\tau}_{ij}^{SGS} = \widehat{\tilde{u}_i \tilde{u}_j} - \hat{\tilde{u}}_i \hat{\tilde{u}}_j \tag{15.7}$$

We suppose that the double filter width is small. Therefore the Smagorinsky model is valid for both stresses τ_{ij}^{SGS} and T_{ij}^{test}:

$$
\begin{aligned}
\tau_{ij}^{SGS} - \frac{1}{3}\tau_{kk}^{SGS}\delta_{ij} &= -2\big(C_s^\Delta \Delta\big)^2 |\tilde{S}_{ij}|\big(\tilde{S}_{ij}\big) = 2C m_{ij}^{SGS}, \\
T_{ij}^{test} - \frac{1}{3}T_{kk}^{test}\delta_{ij} &= -2\big(C_s^\Delta \hat{\Delta}\big)^2 |\hat{\tilde{S}}_{ij}|\big(\hat{\tilde{S}}_{ij}\big) = 2C m_{ij}^{test},
\end{aligned}
\tag{15.8}
$$

The application of the double filter to τ_{ij}^{SGS} gives:

$$\hat{\tau}_{ij}^{SGS} - \frac{1}{3}\hat{\tau}_{kk}^{SGS}\delta_{ij} = 2C\hat{m}_{ij}^{SGS} \tag{15.9}$$

where $C = C_S^2$. Here we supposed that the filtered product of the constant C with m_{ij} is equal to the product of filtered m_{ij} with the same constant

$$\widehat{Cm} \approx C\hat{m}$$

We introduce the tensor L_{ij} which is equal to the difference between test filter and once filtered original SGS stress:

$$L_{ij} = T_{ij}^{test} - \hat{\tau}_{ij}^{SGS} = \widehat{\tilde{u}_i \tilde{u}_j} - \hat{\tilde{u}}_i \hat{\tilde{u}}_j \qquad (15.10)$$

Using this designation we get from (15.8) and (15.9)

$$2CM_{ij} = L_{ij} - \frac{1}{3}L_{kk}\delta_{ij} \qquad (15.11)$$

where

$$M_{ij} = m_{ij}^{test} - \hat{m}_{ij}^{SGS}$$

The system (15.11) is overdefined (six equations for one unknown coefficient C). To get an unique solution we multiply both the l.h.s. and r.h.s of (15.11) with the tensor S_{ij}. The final result for C is

$$C = \frac{L_{ij}\tilde{S}_{ij}}{2M_{ij}\tilde{S}_{ij}} \qquad (15.12)$$

Use of (15.14) is problematic since the denumerator $M_{ij}\tilde{S}_{ij}$ can become zero. To overcome this difficulty Lilly proposed to determine the constant from the condition of the minimum residual of the equation (15.11):

$$Q = \left(L_{ij} - \frac{1}{3}L_{kk}\delta_{ij} - 2CM_{ij} \right)^2 \quad \rightarrow \quad \min \qquad (15.13)$$

The minimum is attained at the point with zero derivative of the functional Q on the parameter C:

$$\frac{\partial Q}{\partial C} = -4M_{ij}\left(L_{ij} - \frac{1}{3}L_{kk}\delta_{ij} - 2CM_{ij} \right) = 0 \qquad (15.14)$$

It follows directly from (15.14):

$$C = \frac{M_{ij}L_{ij} - \frac{1}{3}L_{kk}\delta_{ij}M_{ij}}{2M_{ij}M_{ij}} = \frac{M_{ij}L_{ij}}{2M_{ij}M_{ij}} \qquad (15.15)$$

since $\delta_{ij}M_{ij} = 0$. The solution (15.15) corresponds to the minimum of Q(C) since the second derivative $\partial^2 Q/\partial C^2$ is positive at this point

$$\frac{\partial^2 Q}{\partial C^2} = 8M_{ij}M_{ij} > 0 \qquad (15.16)$$

Theoretically the constant C can become negative. The case $C < 0$ and ν_{SGS} can be considered as the energy backscattering. However, this leads to strong numerical instability. That is why the dynamic constant is limited from below:

$$C = \max\left\{ \frac{M_{ij}L_{ij}}{2M_{ij}M_{ij}}, 0 \right\} \geq 0 \qquad (15.17)$$

The subgrid kinematic viscosity is always positive

$$\nu_{SGS} = C\Delta^2 |\tilde{S}_{ij}| \geq 0$$

15.5 Scale similarity models
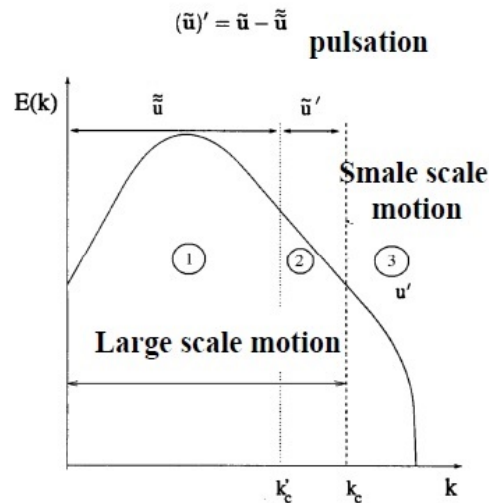
Figure 15.2: Illustrations for derivation of the scale similarity model.

Despite the fact that diffusion of the classic Smagorinsky model was substantially reduced by the dynamic choice of the Smagorinsky constant, the Dynamic Smagorinsky model remains very diffusive. This disadvantage was overcome within the similarity models. The main point of the similarity model is the assumption that the statistical properties of the once filtered field $\tilde{u}_i$ are identical to these of the double filtered field $\tilde{\tilde{u}}_i$. It is the case if the filter width is small. The difference between once and double filtered velocities is negligible, i.e. different scale motions are similar.

Let us consider $\tilde{u}_j$ as the original (unfiltered) field. $\tilde{\tilde{u}}_j$ is the filtered field and $\tilde{u}_j - \tilde{\tilde{u}}_j$ is the pulsation (see Fig. 15.2). Then from the definition of the subgrid stress one obtains

$$\tau_{ij}^{SGS} = \widetilde{\tilde{u}_i \tilde{u}_j} - \tilde{\tilde{u}}_i \tilde{\tilde{u}}_j \tag{15.18}$$

The formula (15.18) is the scale similarity model proposed by Bardina et al. [16]. As seen the SGS stress can be calculated directly from the resolved field $\tilde{u}_i$.

15.6 Mixed similarity models

The experience shows that diffusion produced by the scale similarity model (15.18) is too low. The numerical calculations are often unstable using this model. Taking the fact into account, that the diffusion of the Smagorinsky model is too high, it was decided to combine the Samgorinsky and scale similarity models to get the proper diffusion. The advantages and disadvantages of both models are summarized as follows

- Dynamic Smagorinsky Model (DSM): energy dissipation is overestimated (drawback), energy backscattering is not reproduced (drawback),

- Scale similarity model: energy backscattering is reproduced (advantage), energy dissipation is underestimated (drawback).

The idea combine models to strengthen the advantages and to overcome disadvantages of both models. The hybrid model called as the mixed similarity model is written as

$$\tau_{ij}^r = \left(\widetilde{\tilde{u}_i \tilde{u}_j} - \tilde{\tilde{u}}_i \tilde{\tilde{u}}_j \right) - 2\left(C_S^\Delta \Delta \right)^2 |\tilde{S}| \tilde{S}_{ij} \tag{15.19}$$

The mixed model can be derived in a more formal way. For that the velocity decomposition into filtered and pulsation parts:

$$\widetilde{u_i u_j} = \widetilde{(\tilde{u}_i + u_i')(\tilde{u}_j + u_j')} = \widetilde{\tilde{u}_i \tilde{u}_j} + \widetilde{u_i' \tilde{u}_j} + \widetilde{u_j' \tilde{u}_i} + \widetilde{u_i' u_j'} \tag{15.20}$$

is substituted into the SGS stress expression:

$$\tau_{ij}^{SGS} = \widetilde{u_i u_j} - \tilde{u}_i \tilde{u}_j \tag{15.21}$$

Finally we have Leonard's formulation of the mixed model:

$$\boxed{\tau_{ij}^{SGS} = L_{ij} + C_{ij} + R_{ij}} \tag{15.22}$$

where

$$
\begin{array}{ll}
L_{ij} = \widetilde{\tilde{u}_i \tilde{u}_j} - \tilde{u}_i \tilde{u}_j & \text{is the Leonard stress} \\
C_{ij} = \widetilde{\tilde{u}_i u'_j} + \widetilde{\tilde{u}_j u'_i} & \text{is the Cross stress} \\
R_{ij} = \widetilde{u'_i u'_j} & \text{is the Reynolds stress}
\end{array}
$$

The sum of the cross and Reynolds stresses is calculated via the Smagorinsky model with the dynamically determined constant C_S

$$\boxed{C_{ij} + R_{ij} = -2\left(C_S^{\Delta}\Delta\right)^2 |\tilde{S}| \tilde{S}_{ij}} \tag{15.23}$$

A substantial disadvantage of this formulation is the fact that the Leonard stress does not satisfy the Galilean invariance condition. The Galilean invariance is the independence of basic formula of mechanics on the speed of the reference system.

The classical definition of the SGS stresses possesses the Galilean invariance. Indeed, let V be the speed of the reference system. The velocity relative to the reference system is

$$\vec{W} = \vec{u} + \vec{V} \tag{15.24}$$

The SGS stress does not depend on the reference system speed:

$$
\begin{aligned}
\widetilde{W_i W_j} &- \tilde{W}_i \tilde{W}_j = \\
&= \widetilde{(\tilde{u}_i + V_i + u'_i)(\tilde{u}_j + V_j + u'_j)} - \widetilde{(\tilde{u}_i + V_i + u'_i)}\widetilde{(\tilde{u}_j + V_j + u'_j)} = \\
&= \widetilde{(\tilde{u}_i + u'_i)(\tilde{u}_j + u'_j)} - \widetilde{(\tilde{u}_i + u'_i)}\widetilde{(\tilde{u}_j + u'_j)} = \widetilde{u_i u_j} - \tilde{u}_i \tilde{u}_j
\end{aligned}
\tag{15.25}
$$

On the contrary, the Leonard stress is not Galilean invariant:

$$\widetilde{\tilde{W}_i \tilde{W}_j} - \tilde{W}_i \tilde{W}_j = \widetilde{\tilde{u}_i \tilde{u}_j} - \tilde{u}_i \tilde{u}_j - V_i \tilde{u}'_j - V_j \tilde{u}'_i \tag{15.26}$$

Germano proposed an alternative formulation

$$\boxed{\tau_{ij}^{SGS} = L_{ij}^0 + C_{ij}^0 + R_{ij}^0} \tag{15.27}$$

where all stresses are Galilean invariant:

$$\begin{aligned}
L_{ij}^0 &= \widetilde{\tilde{u}_i \tilde{u}_j} - \tilde{\tilde{u}}_i \tilde{\tilde{u}}_j & \text{is the Leonard stress} \\
C_{ij}^0 &= \widetilde{\tilde{u}_i u_j'} + \widetilde{u_i' \tilde{u}_j} - \tilde{\tilde{u}}_i \tilde{u}_j' - \tilde{u}_i' \tilde{\tilde{u}}_j & \text{is the Cross stress} \\
R_{ij}^0 &= \widetilde{u_i' u_j'} - \tilde{u}_i' \tilde{u}_j' & \text{is the Reynolds stress}
\end{aligned}$$

$$\boxed{C_{ij}^0 + R_{ij}^0 = -2\big(C_S^\Delta \Delta\big)^2 |\tilde{S}| \tilde{S}_{ij}} \tag{15.28}$$

Exercise: Prove the following facts:

- equivalence of subgrid stresses computed from formulations of Germano (15.27) and the original one proposed by Leonard (15.22),

- Galilean invariance of stresses in Germano's formulation (15.27).

15.7 A-posteriori and a-priori tests

Two tests are used to verify LES models. The comon way is the a-posteriori test. The LES simulation is performed and then the flow parameters obtained from the simulation are compared with these from measurement. Depending on comparison results the conclusion about quality of LES models is drawn. The disadvantage of such approach is that the LES results are affected by modelling errors, errors of approximation of differential operators and rounding errors. In a-posteriori test they can not be separated.

Direct test of quality of subgrid stresses is the a-priori test. First, the subgrid stress is calculated at each time instant from the definition

$$\tau_{ij}^{SGSdef} = \widetilde{\tilde{u}_i \tilde{u}_j} - \tilde{u}_i \tilde{u}_j \tag{15.29}$$

Then the subgrid stress is computed again at each time instant from any model, say Smagorinsky one

$$\tau_{ij}^{SGSmod} - \frac{1}{3}\tau_{kk}^{SGSmod}\delta_{ij} = -2(C_S\Delta)^2 |\tilde{S}_{ij}| \tilde{S}_{ij} \tag{15.30}$$

The subgrid stresses $\overline{\tau_{ij}^{SGSdef}}$ and $\overline{\tau_{ij}^{SGSmod}}$ averaged in time are compared each with other. If

$$\overline{\tau_{ij}^{SGSdef}} \approx \overline{\tau_{ij}^{SGSmod}}$$

the SGS model is accurate.

A big difficulty of a-priori tests is the determination of velocities $\tilde{u}_i$. For that it is necessary first to obtain the unfiltered velocities u_i with spatial and temporal resolutions compared with the Kolmogorov scales. At present this is a big challenge to measure three components of velocity in a volume with high spatial and temporal resolutions. The Particle Image Velocimetry (PIV) measurements are mostly planar measurements within a two dimensional window. Direct Numerical Simulation data are often used as the source for a-priori tests. Three components of velocity in a volume, obtained from DNS, are filtered and utilized for the test. However, it should be noted that DNS simulation is restricted by relatively low Reynolds numbers, whereas main laws of LES are valid for high Re numbers.
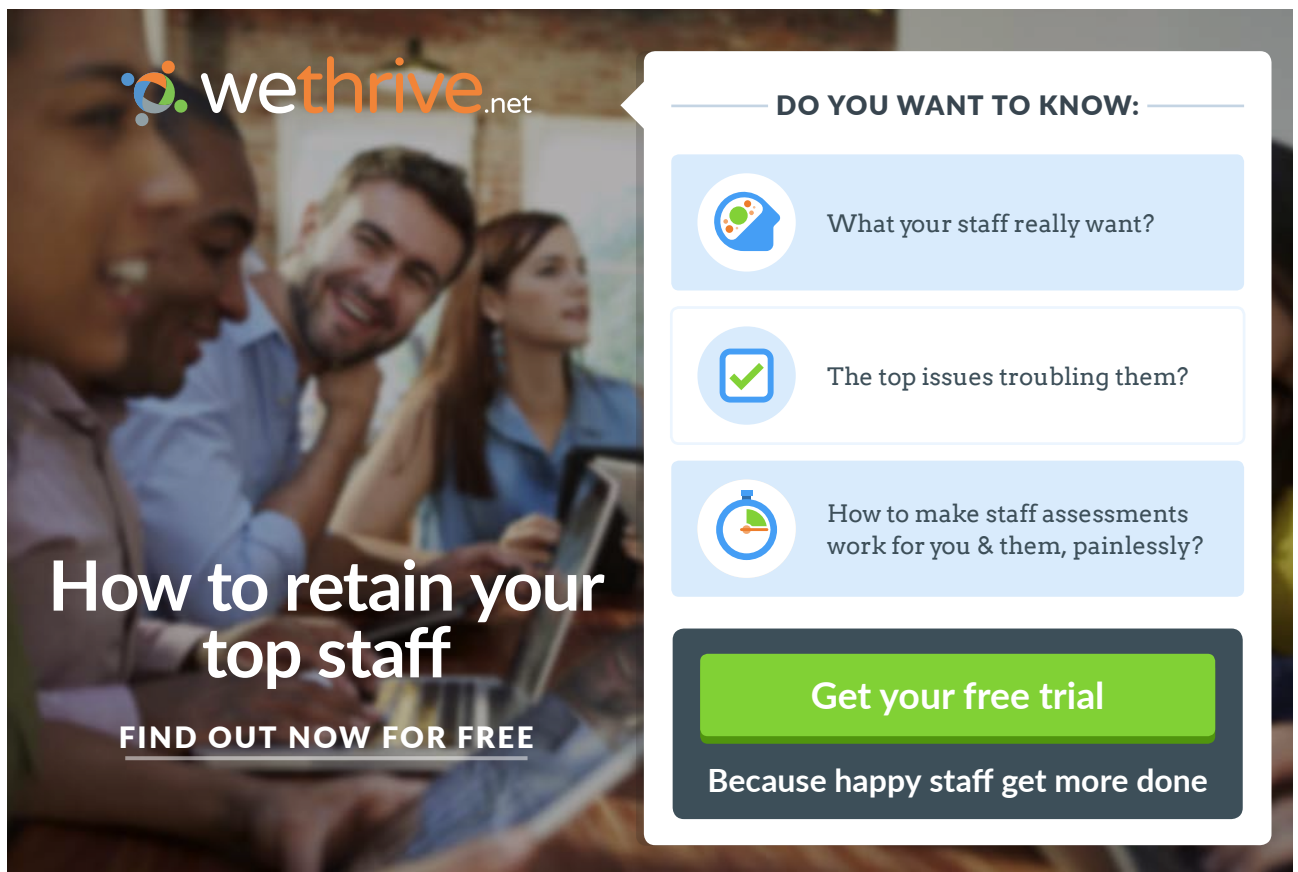
Chapter 16

Hybrid URANS-LES methods

16.1   Introduction

As discussed above, the most promising approach to resolve the flow un-steadiness is the Large Eddy Simulation (LES), which is already widely used for research purposes. Typical Reynolds numbers in engineering are very large even at model scales. The grid resolution necessary for a pure LES is so huge that it makes the direct application of LES impossible (see Sec. 16.4). A practical solution of this problem is the use of hybrid URANS-LES methods, where the near body flow region is treated using URANS and far flow regions are treated with LES.

According to Peng [17] the hybrid techniques can be subdivided into flow matching and turbulence matching methods. Within the flow matching methods the interface between URANS and LES is explicitly defined. LES filtered equations are solved in the LES region, whereas URANS equations are solved in the URANS domain. The flow parameters (velocities, kinetic energy) are matched at the interface between the URANS and the LES regions. Among the most important contributions to the development of flow matching methods we mention the works of (Davidson, Dalstroem [18]; Terracol [19]; Jakirlic et. al. [20]; Temmerman et. al. [21]) and others. A serious weakness of this approach is the development of robust procedures to set the URANS-LES interface for complicated flow geometries. Within the framework of the turbulence matching method an universal transport equation is solved in the whole computational domain. The stress terms in this equation are treated in different ways in LES and URANS domains. There are various procedures to distinguish between LES and URANS cells. The most popular hybrid method is Detached Eddy Simulation (DES) proposed by (Spalart et al.[22]). The original version of this method is based on the classic Smagorinsky LES model and the Spalart-Allmaras (SA) URANS approach. SA is used close to the wall, whereas LES in the rest part of the flow. The switching between the two techniques is smooth and occurs in a "gray" subdomain. There are two major improvements of DES, developed recently. The first one, DDES (Delayed DES), has been proposed to detect the boundary layers and to prolong the RANS mode, even if the wall-parallel grid spacing would normally activate the DES limiter (Spalart [23]). The second one, IDDES (Improved DDES), allows one to solve the problems with modelled-stress depletion and log-layer mismatch. For the details see the review (Spalart [23]). In spite of a wide application area DES has serious principle limitations thoroughly analyzed by (Menter, Egorov [24]). Other versions of the turbulence matching methods using different blending functions to switch the solution between LES and URANS modes were proposed by (Peng [17]; Davidson, Billson [25]; Abe, Miyata [26]) and others.

A very critical point of the turbulence matching methods is the transition from the time (or ensemble) averaged smooth URANS flow to the oscillating LES flow, see (Menter, Egorov, 2005). The oscillations have to appear within a short flow domain in a "gray zone" between LES and URANS. Experience shows that it is extremely difficult to provide a smooth transition of the turbulent kinetic energy passing from the URANS to LES domain. To overcome this problem (Schlueter et al. [27]) and (Benerafa et al. [28]) used an additional forcing term in the Navier Stokes equation artificially enhancing fluctuations in the gray zone. However, the problem of smooth solution transition from URANS to LES still remains as the main challenge for the turbulence matching methods.

16.2   Detached Eddy Simulation (DES)

The most popular hybrid method -detached eddy simulation- was proposed in 1997 by Spalart et al. [22]. The principle of DES is illustrated in Fig. 16.1. Close to the body the solution is calculated using the URANS mode. Far from the wall the LES equations are solved. The grey zone between URANS and LES is the mixed solution.

The classical version of the DES approach is based on the Spalart Almaras (SA) model formulated with respect to the modified turbulent viscosity $\tilde{\nu} = \nu_t/f_{\nu1}$. The transport equation for $\tilde{\nu}$ reads
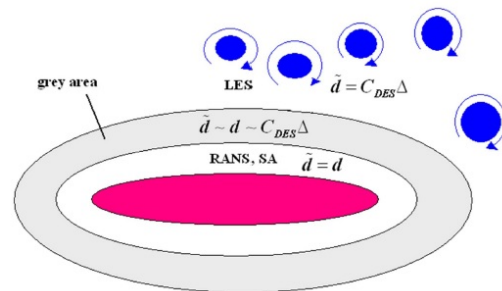
Figure 16.1: Zones of the Detached Eddy Simulation.

$$
\frac{\partial \tilde{\nu}}{\partial t} + \bar{v}_j \frac{\partial \tilde{\nu}}{\partial x_j} = \underbrace{C_{b1}\tilde{S}\tilde{\nu}}_{\text{Generation}} - \underbrace{C_{w1}f_w\left(\frac{\tilde{\nu}}{d}\right)^2}_{\text{Destruction}} +
$$
$$
+ \underbrace{\frac{1}{\sigma}\frac{\partial}{\partial x_k}\left((\nu + \tilde{\nu})\frac{\partial \tilde{\nu}}{\partial x_k}\right) + \frac{C_{b2}}{\sigma}\frac{\partial \tilde{\nu}}{\partial x_k}\frac{\partial \tilde{\nu}}{\partial x_k}}_{\text{Diffusion}}
$$

(16.1)

where

$$C_{b1} = 0.1355, \quad C_{b2} = 0.622, \quad C_{v1} = 7.1,$$

$$\sigma = 2/3, \quad C_{w1} = \frac{C_{b1}}{\kappa^2} + \frac{1 + C_{b2}}{\sigma},$$

$$C_{w2} = 0.3, \quad C_{w3} = 2.0, \quad \kappa = 0.41,$$

$$f_{v1} = \frac{\chi^3}{\chi^3 + C_{v1}^3}, \quad f_{v2} = 1 - \frac{\chi}{1 + \chi f_{v1}},$$

$$f_w = g\left[\frac{1 + C_{w3}^6}{g^6 + C_{w3}^6}\right]^{1/6}, \quad \chi = \tilde{\nu}/\nu,$$

$$g = r + C_{w2}(r^6 - r), \quad r = \frac{\tilde{\nu}}{\tilde{S}\kappa^2 d^2},$$

$$\tilde{S} = S + \frac{\tilde{\nu}}{\kappa^2 d^2} f_{v2}, \quad S = \sqrt{2\Omega_{ij}\Omega_{ij}},$$

$$\Omega_{ij} = \frac{1}{2}\left(\frac{\partial \bar{v}_i}{\partial x_j} - \frac{\partial \bar{v}_j}{\partial x_i}\right)$$
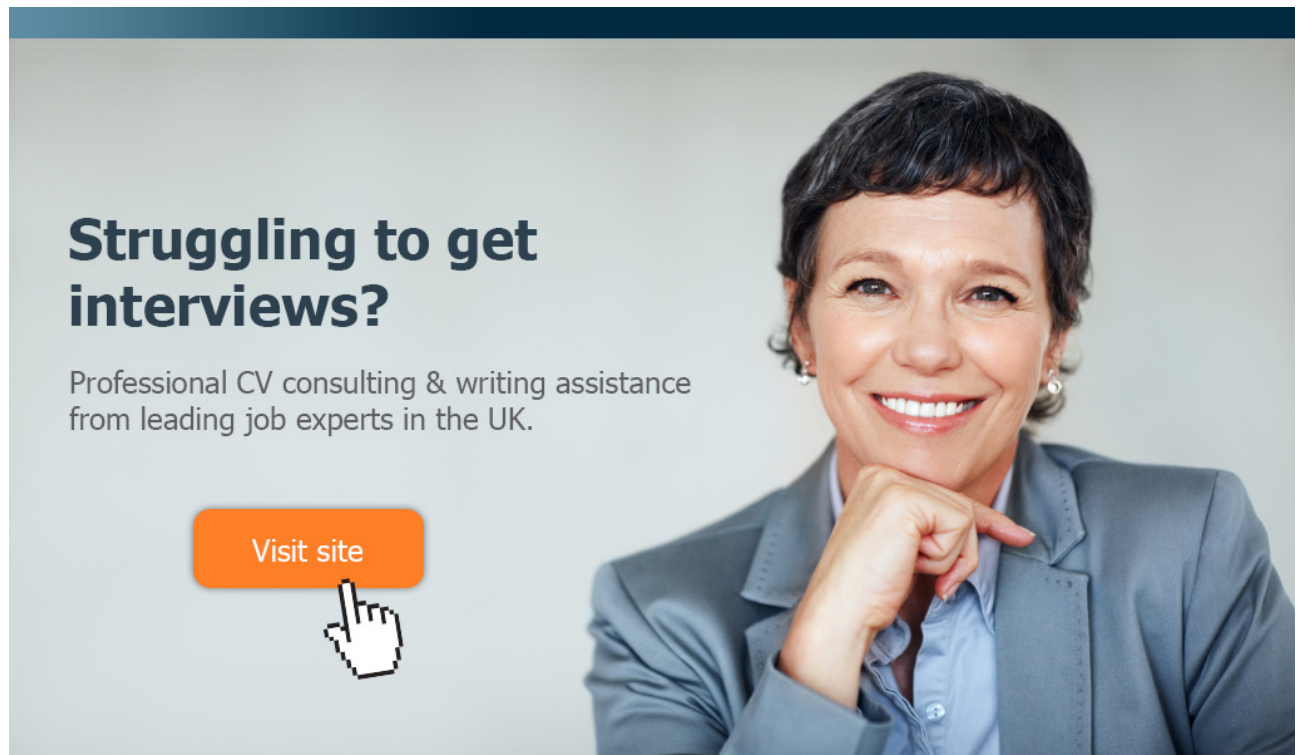
Here d is the distance from the wall. The physical sense of different terms is illustrated in (16.1). Far from the wall the generation and the distruction terms are approaching each to other and the turbulence attains the equilibrium state:

$$\underbrace{C_{b1}\tilde{S}\tilde{v}}_{\text{Generation}} - \underbrace{C_{w1}f_w\left(\frac{\tilde{v}}{d}\right)^2}_{\text{Destruction}} \sim 0$$

The kinematic viscosity is then calculated from the formula

$$\tilde{v} \sim \frac{C_{b1}}{C_{w1}}\tilde{S}d^2$$

which is similar to the Smagorinsky one:

$$v_t = l_S^2|\tilde{S}_{ij}|, \qquad |\tilde{S}_{ij}| = \sqrt{2\tilde{S}_{ij}\tilde{S}_{ij}}$$

$$l_S = C_S\Delta$$

DES inventors proposed to use the following expression for d:

$$d = \min\{d, C_{DES}\Delta\}, \qquad \Delta = \max\{\Delta x, \Delta y, \Delta z\}$$

where $C_{DES} \approx 1.3$ is the DES constant. Now the main idea of the DES becomes obvious:

• At small wall distance $d < C_{DES}\Delta$ the Spalart Almaras URANS model is active

• At large wall distance $d > C_{DES}\Delta$ the Spalart Almaras URANS model is smoothly passed into the Smagorinsky model.

Samples of DES applications are presented in Fig. 16.2 and 16.3.

Despite of the wide application Detached Eddy Simulation technique is not free of disadvantages. Menter [24] notes: The essential concern with DES is that it does not continuously change from RANS to LES under grid refinement. In order for LES structures to appear, the grid spacing and time step have to be refined beyond a case-dependent critical limit. In addition, a sufficiently large instability mechanism has to be present to allow the rapid formation of turbulent structures in regions where the DES limiter is activated. If one of the two, or both requirements are violated, the resulting model is undefined and the outcome is largely unpredictable.
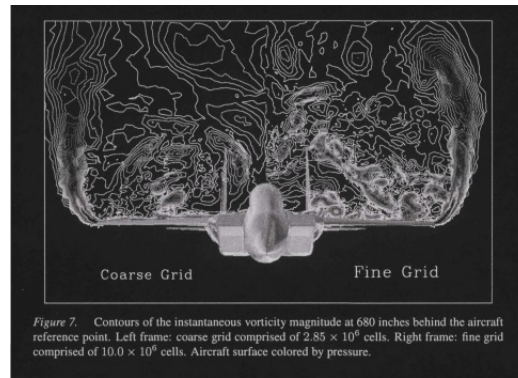
Figure 16.2: Flow around combat aircraft. (Squires K.D., Detached-eddy simulation: current status and perspectives)
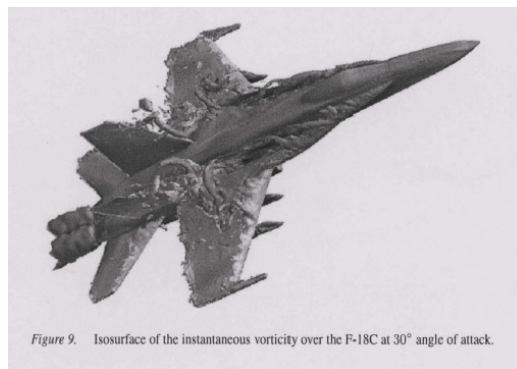
Figure 16.3: Flow around combat aircraft. (Squires K.D., Detached-eddy simulation: current status and perspectives)

16.3   Hybrid model based on integral length as parameter switching between LES and URANS

A simple hybrid model proposed in [29] is based on the observation that the basic transport equations have the same form in LES and RANS

$$\frac{\partial \overline{u}_i}{\partial t} + \frac{\partial (\overline{u}_i \overline{u}_j)}{\partial x_j} = -\frac{\partial \overline{p}^*}{\partial x_i} + \frac{\partial (\tau_{ij}^l + \tau_{ij}^t)}{\partial x_j}, \qquad (16.2)$$

but the interpretation of the overline differs. In LES it means filtering, but in RANS it stands for the Reynolds, or ensemble, averaging. Here we used the standard notation of p^* for the pseudo-pressure, and τ_{ij}^l and τ_{ij}^t for the
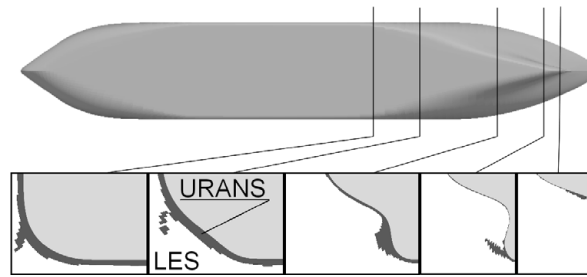
Figure 16.4: The division of the computational domain into the URANS (dark) and LES (light) regions at one time instant for hybrid calculation of tanker.

laminar and turbulent stresses respectively. Note that the turbulent stresses are calculated in different ways in LES and URANS regions.

The computational domain in our model is dynamically (i.e. at each time step) divided into the LES and URANS regions. A cell of the mesh belongs to one or the other region depending on the relation between the integral length scale L and the extended LES filter Δ according to the following rule:

$$\begin{aligned} &\text{if } L > \Delta \text{ then the cell is in the LES region,} \\ &\text{if } L < \Delta \text{ then the cell is in the URANS region.} \end{aligned} \qquad (16.3)$$

The integral length scale is calculated from the known formula of Kolmogorov and Prandtl with the correction factor 0.168 taken from [12]

$$L = C\frac{k^{3/2}}{\varepsilon}, \qquad (16.4)$$

where k is the turbulent kinetic energy and ε is the dissipation rate. The constant C is $C \sim 0.168$ close to the wall $y/\delta < 0.2$, $C \sim 0.35$ at $0.2 < y/\delta < 0.7$ and $C \sim 1.0$ in the outer area of the bounder layer $y/\delta > 0.7$, where δ is the boundary layer thickness. L varies from one time step to another, which results in varying decomposition of the computational domain into the LES and URANS regions. The extended LES filter is computed as

$$\Delta = \sqrt{d_{\max}^2 + \delta^2}, \qquad (16.5)$$

where $d_{\max}$ is the maximal length of the cell edges $d_{\max} = \max(d_x, d_y, d_z)$ and $\delta = $ (the cell volume)$^{1/3}$ is the common filter width used in LES. This choice ensures that very flat cells in the boundary layer (for which $\delta \approx 0$ but $d_{\max} > 0$) are treated correctly. Δ depends only on the mesh and it is precomputed only once before the main computation.

As a sample LES and URANS regions are shown in Fig. 16.4 for flow around a tanker. The URANS region is located close to the ship surface and plays the role of a dynamic wall function. In areas of bilge vortices formation, the boundary layer is shedding from the hull and penetrates into the outer flow part. Since the boundary layer is a fine scale flow the procedure (16.3) recognizes the bilge vortex formation zones as URANS ones. There is a technical issue concerning the cells which are far from the ship hull and where both k and ε are small, so large numerical errors are introduced into the integral length scale computed according to Eq. (16.4). To avoid an irregular distribution of URANS and LES zones, the general rule (16.3) of the domain decomposition is corrected in such a way that the LES region is switched to URANS one if k is getting less than some threshold. This procedure has no influence on the ship flow parameters since it is used far from the area of the primary interest.

We have performed several calculations with different combinations of LES and URANS models to find the most efficient one for the problem under consideration. Among the models we used in our computations are the linear and nonlinear k-ε, k-ω SST and $k\varepsilon v^2 f$ URANS models combined with the simple and dynamic Smagorinsky as well as with the dynamic mixed LES closure models. The experience shows that the most satisfactory results are obtained using the URANS approach based on the $k\varepsilon v^2 f$ turbulent model of [30] and LES approach based on the Smagorinsky dynamic model. The turbulent stresses τ_{ij}^t are calculated from the Boussinesq approximation using the concept of the turbulent viscosity. The only difference between LES and URANS is the definition of the kinematic viscosity. Within LES it is considered as the subgrid viscosity and calculated according to the dynamic model of Smagorinsky:

$$\nu_{\mathrm{SGS}} = c_D \delta^2 |S_{ij}|, \quad S_{ij} = \frac{1}{2}\left(\frac{\partial u_j}{\partial x_i} + \frac{\partial u_i}{\partial x_j}\right), \tag{16.6}$$

where S_{ij} is the strain velocity tensor and c_D is the dynamic constant. In the URANS region the viscosity is calculated from the turbulent model of [30]:

$$\nu_t = \min\left(0.09\frac{k^2}{\varepsilon}, 0.22 v^2 T_t\right), \tag{16.7}$$

where v^2 is the wall normal component of the stresses and T_t is the turbulent time $T_t = \max(k/\varepsilon, 6\sqrt{\nu/\varepsilon})$.

16.4 Estimations of the resolution necessary for a pure LES on the example of ship flow

In the CFD community one can observe tendency to use pure LES without paying any attention to resolution problems. Very often LES is running on typical RANS grids. In fact, such computations can give correct results if the flow structures to be captured are large enough and exist for a long time. In some cases modeling of such structures does not require detailed resolution of boundary layers and a thorough treatment of separation regions. As an example one can mention flows around bluff bodies with predefined separation lines like ship superstructures. Application of underresolved LES for well streamlined hulls should be considered with a great care. First of all, one should not forget that the basic LES subgrid models are derived under the assumption that at least the inertial turbulent subrange is resolved. Second, underresolution of wall region leads to a very inaccurate modeling of the boundary layer, prediction of the separation and overall ship resistance. It is clearly illustrated in the Table 16.1. The ship resistance obtained from underresolved LES using the wall function of (Werner, Wengle [31]) is less than half of the measured one and that obtained from RANS. Obviously, the application of modern turbulence LES models, more advanced than RANS models, does not improve but even makes the results much worse with the same space resolution. The change from RANS to LES should definitely be followed by the increase of the resolution which results in a drastic increase of the computational costs. These facts underline necessity of further development towards hybrid methodology. Although in (Alin et al. [32]) it has been shown that the accuracy of the resistance prediction using pure LES at a very moderate resolution with $y^+ \sim 30$ can be improved using special wall functions, the most universal way for the present, to our opinion, is application of hybrid methods. The impossibility of pure LES is illustrated below for flow around the KVLCC2 tanker.

The precise determination of the necessary LES resolution is quite difficult. Estimations presented below are based on the idea that about 80% of the turbulent kinetic energy should be directly resolved and the rest is modeled in a properly resolved LES simulation. Implementation of this idea implies the knowledge of the Kolmogorov η and the integral length L scales which are used to draw the typical spectra of the full developed turbulence $E(k)$. The wave number k^* separating the resolved and modeled turbulence is found from the condition

$$\frac{\int_{k^*}^{\infty} E(k)dk}{\int_0^{\infty} E(k)dk} \approx 0.2. \qquad (16.8)$$
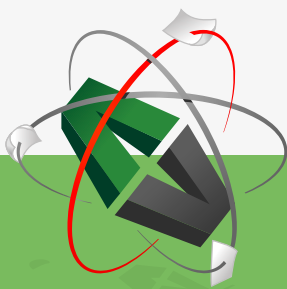
The maximum possible cell size is then $\Delta_{\max} = 2\pi/k^*$. The scales L and η are found from the known expression $\eta = (\nu^3/\varepsilon)^{1/4}$ and Eq. (16.4), where the kinetic energy k and the dissipation rate ε are taken from RANS simulations using k-ε linear model. The ratio $\lambda = \Delta_{\max}/\eta$ is then used as the scale parameter for grid generation. Both lengths vary in space which makes the grid generation procedure very complicated. To roughly estimate the size of the grid we assume that λ is constant. We performed different calculations determining λ at the two following points: i) the point where L/η is maximal in the ship boundary layer and ii) the point in the propeller disk where the vorticity $\vec{\omega}$ is maximal (region of the concentrated vortex structure). The latter is dictated by the wish to resolve the most intensive vortex flow structures which have the strongest influence on the propeller operation. Since LES application is required in the ship stern area only this part of the computational volume has been meshed. It covers the boundary layer of the stern region starting from the end of the parallel midship section. The thickness of the meshed region has been constant and equal to the maximum boundary layer thickness at the stern δ_{BL}. The grid for a pure LES is generated using the following algorithm. The minimum Kolmogorov length $\eta_{\min}$ is determined in the near wall region. The cell sizes in x and z directions along the wall are calculated by multiplication of $\eta_{\min}$ with the scale parameter λ. These sizes remain constant for all cells row in y direction which is normal to the ship surface (see Fig. 16.5). The cells have at least two equal sizes which is desirable from the point of view of LES accuracy. The choice of the size in y direction is dictated by proper resolution of the boundary layer. Close to the wall this size is chosen from the condition $\Delta_w = \min(y_w, \eta_{\min})$. Since y_w is chosen as the ordinate where $y^+ = 1$ the first nodes lay deeply in the viscous sublayer. The size in y direction at the upper border of the boundary layer is equal to $\Delta_\infty = \lambda \eta_\delta$, where η_δ is the Kolmogorov scale at $y = \delta_{BL}$. A simple grading is used in y direction between Δ_w and Δ_∞.

Results of the estimations are as follows: the required grid size ranges from ~ 5 M to ~ 25 M for Re $= 2.8 \times 10^6$, and from ~ 7 M to ~ 60 M for Re $= 5.8 \times 10^6$. The results vary depending on the value of λ in use, so they should be considered as very rough estimations. Together with similar estimations for the nonlinear k-ε model these results show that the LES
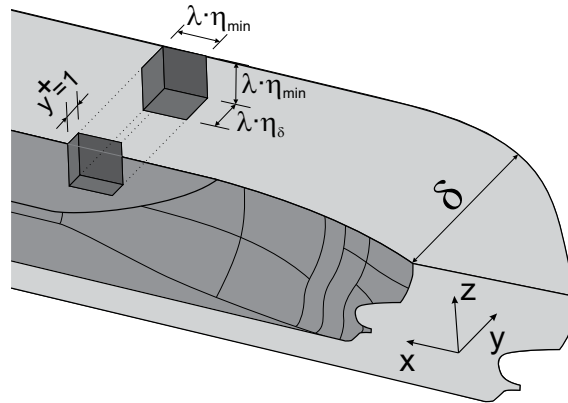
Figure 16.5: The cell parameters.

grid should have the order of tens of millions of nodes. Nowadays, the computations with hundred millions and even with a few billions of nodes are becoming available in the research community. However, a numerical study of engineering problems implies usually many computations which have to be performed within a reasonable time with moderate computational resources. In this sense, the results of the present subsection clearly demonstrate that the pure LES is impossible for ship applications so far. To verify that the resolution estimation procedure we used gives meaningful results, it has been applied for turbulent boundary layer (TBL) benchmark. We found from methodical calculations that the pure LES with 1M cells is quite accurate for prediction of the velocity distribution, TBL thickness, TBL displacement thickness and the wall shear stress. The estimation procedure presented above predicted the necessary resolution around 0.5M. Therefore, the estimations presented for a ship model are rather lower bound for the resolution required for a pure LES.

	C_R	C_P	C_F
KRISO Exp.	4.11×10^{-3}	15%	85%
RANS $k\varepsilon v^2 f$	4.00×10^{-3}	16%	84%
k-ω SST SAS	3.80×10^{-3}	18%	82%
Underresolved LES	1.70×10^{-3}	81%	19%
Hybrid RANS LES	4.07×10^{-3}	17%	83%

Table 16.1: Results of the resistance prediction using different methods. C_R is the resistance coefficient, C_P is the pressure resistance and C_F is the friction resistance

Part III

CFD applications to human thermodynamics

Lectures on computational fluid dynamics

Mathematical model of the ice protection
of a human body at high temperatures
of surrounding medium

Chapter 17

Mathematical model of the ice protection of a human body at high temperatures of surrounding medium

17.1   Designations

17.1.1   List of symbols

A area (m^2)
c_p specific heat capacity (J/(kgK))
F density of heat release(W/m^3)
h sector height (m)
K correlation factor of the rectal temperature
k the thermal conductivity (W/(mK))
M work done by person (W)
m body mass (kg)
P body height (cm)
Q internal energy (J)
$\dot{Q}$ heat flux (W)
R sector radius (m)
T temperature (deg)
x radial coordinate along the sector (m)
α central sector angle (deg)
Δ skin thickness (m)
λ thermal diffusivity (m^2/s)
ρ mass density (kg/m^3)
ϕ initial temperature (deg)

17.1.2   Subscripts

$core$ human body core
hum human body
i number of human body layer
j number of point on the human body
med surrounding medium
$melt$ melting ice
$outer$ outer boundary of clothes
$skin$ human body skin

Lectures on computational fluid dynamics

Mathematical model of the ice protection
of a human body at high temperatures
of surrounding medium

17.1.3 Superscripts

0 degree of Celsius

17.2 Introduction

The heat transfer inside the human body is an extremely complicated problem which is difficult to formulate properly. The body generates the heat within certain organs which is then transferred by the thermal diffusion through the body substance possessing very non uniform properties. However, the thermal diffusion being complicated is not the main difficulty of modeling. A large fraction of the heat generated by internal organs is transported to the body periphery by a complicated net of blood vessels. This process has still not been modeled with a desirable accuracy. While a full detailed model of the human thermodynamics is still remaining the problem of the future, the practical design of protection clothes demands the reliable models already now. Such models are necessary to reduce the time and costs consuming measurements and to avoid dangerous experiments with people under emergency conditions. The models can be only of a semi empiric character and must relay on measurements data to diminish the modelling errors.

Especially interesting is the case of human thermodynamics at high temperatures T of surrounding medium. At $T > 35^0$ the ability of human thermoregulation is very restricted [33]. The acceptable body temperature variation can be only one degree of Celsius. If the body temperature exceeds this threshold the protecting mechanisms regulating the excessive heat in the organism through the breathing, humidity diffusion of the skin, radiation and transpiration don't work [34], [35]. The most effective principle of the protection is the mechanism of the heat absorption through, for instance, the ice embedded into the clothes. This approach being environmentally friendly,
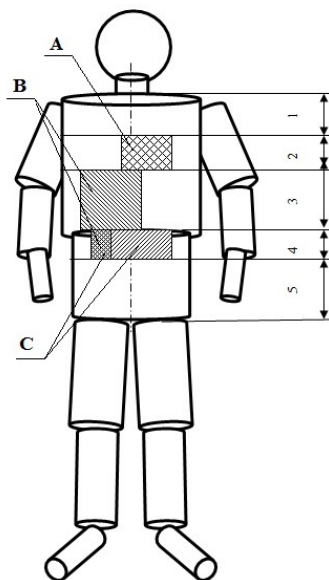

Figure 17.1: Sketch of the human body used in simulations. A- heart, B- liver, C - kidney.

173

Lectures on computational fluid dynamics

Mathematical model of the ice protection
of a human body at high temperatures
of surrounding medium

technologically easy and renewable can be used for protection clothes of res-
cue teams working under high temperatures up to 50^0 and more.

17.3 Human body and ice protection models

The human body model used for simulation is shown in Fig. (17.1). The
main sizes of the body which are important for the discussion of results are
presented in the table 17.1.

Commonly the human body is represented as a set of geometric elements ac-
cording to the original idea proposed by Stolwijk [36]. The body is assumed
to be slender with domination of the heat transfer in horizontal planes. On
the contrary to common models the horizontal cross section of the human
body is represented in our model as a nearly elliptical section with the dis-
placed center. The cross section of the body is subdivided into the five
layers [33]: skin, fat layer, muscles and two core layers (see Fig. (17.2)). The
core represents all human organs and blood vessels. The cross section of
the human body is then represented as a set of sectors subdivided along the
radius into five layers with constant thermal properties (see Fig. 17.2). The

Lectures on computational fluid dynamics

Mathematical model of the ice protection
of a human body at high temperatures
of surrounding medium

Table 17.1: Sizes of the body used in simulations

Element	Size in meter
1	0.127
2	0.127
3	0.234
4	0.090
5	0.215

radii of each sector R can be found from the table 17.2. The upper elliptical cylinder is from the neck to the waist, whereas the lower one from the waist to the thing (Fig. 17.1). The skin thickness Δ is approximately calculated as the radius R divided by 60.25 [33]. The sizes of different layers inside of the cross section are presented in the table 17.3. At the high temperatures the main part of the heat production occurs in certain organs. The knowledge about the heat distribution inside the body allows one to choose the most efficient design of the ice protection which typical construction is shown in Fig. 17.3. In the mathematical model the ice and the clothes layer are modelled by additional layers covering the human body (Fig. 17.2). The human body model was developed on the base of data taken from [36], [37], [38] and [39].

17.4 Mathematical model

It is assumed, that the heat exchange between the sectors is negligible at every cross section of the human body. Therefore both the vertical and circumferential heat transfer processes are not taken into account. The heat transfer along the radius x within each sector is described by the one dimensional heat conduction equation derived from the energy conservation consideration. The change of the internal energy in the sector element with coordinates x and $x + dx$ due to heat transport within the time dt is

$$dQ_1 = \left(k(x+dx)S(x+dx)\frac{\partial T}{\partial x} - k(x)S(x)\frac{\partial T}{\partial x} \right) dt \approx \frac{\partial}{\partial x}\left(k(x)S(x)\frac{\partial T}{\partial x} \right) dt$$
(17.1)

where $T(x,t)$ is the temperature, k is the thermal conductivity, $S(x) = \alpha x h$ is the sector arc length multiplied with its height h and α is the central angle

Lectures on computational fluid dynamics

Mathematical model of the ice protection
of a human body at high temperatures
of surrounding medium
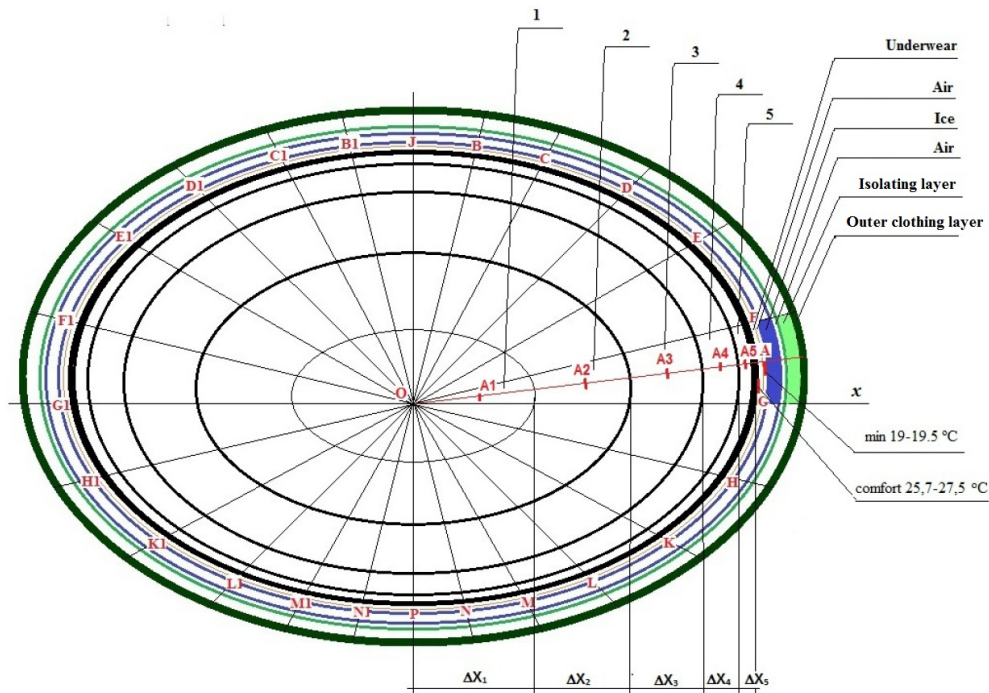
Figure 17.2: Horizontal cross section of the human body represented as an
ellipse with five layers: 1- inner core, 2- outer core, 3- muscles, 4- fat, 5- skin.
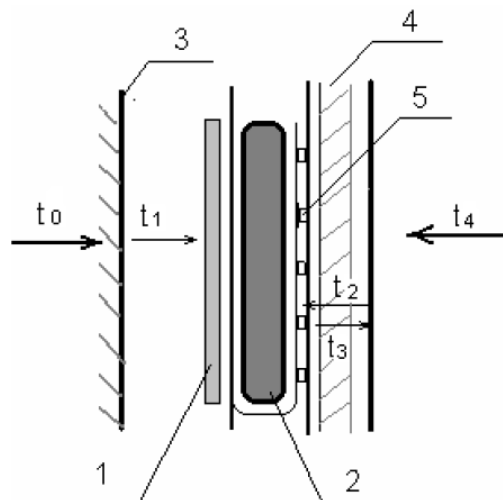
Figure 17.3: Ice protection construction. 1- polyurethane foam, 2- ice
briquette, 3- human body, 4-special overheating protection clothes, 5-
polyurethane net (air layer).

Lectures on computational fluid dynamics

Mathematical model of the ice protection
of a human body at high temperatures
of surrounding medium

Table 17.2: Radii of the elliptical cross sections used in simulations

radial line	upper elliptical cylinder, m	lower elliptical cylinder, m
OJ	0.118	0.109
OB, OB1	0.122	0.112
OC, OC1	0.137	0.121
OD, OD1	0.159	0.135
OE, OE1	0.181	0.156
OF, OF1	0.195	0.176
OG, OG1	0.200	0.190
OH, OH1	0.187	0.173
OK, OK1	0.163	0.145
OL, OL1	0.138	0.121
OM, OM1	0.120	0.106
ON, ON1	0.110	0.980
OP	0.106	0.940

Table 17.3: Radii of layers used in simulations in fraction of the skin thickness Δ

Lectures on computational fluid dynamics

Mathematical model of the ice protection
of a human body at high temperatures
of surrounding medium
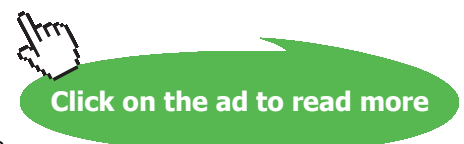
Elliptical cylinder	Element length, m	Area m^2	Layer	Radius
upper	0.476	0.489	Core	36.15Δ
			Muscle	53.70Δ
			Fat layer	59.25Δ
			Skin	60.25Δ
lower	0.317	0.293	Core	36.15Δ
			Muscle	53.70Δ
			Fat layer	59.25Δ
			Skin	60.25Δ

of the sector. Within the material we have additionally the heat release with the heat density F (heat per unit volume):

$$dQ_2 = SFdxdt \qquad (17.2)$$

Due to the heat transfer and heat release the internal energy of the material is changed by dQ_3

$$dQ_3 = c_p\rho S\frac{\partial T}{\partial t}dxdt \qquad (17.3)$$

where c_p is the specific heat capacity and ρ is the mass density of the material. By conservation of energy

$$dQ_1 + dQ_2 = dQ_3$$

or

$$S(x)\frac{\partial T}{\partial t} = \lambda\frac{\partial}{\partial x}\left(S(x)\frac{\partial T}{\partial x}\right) + S(x)f(x) \qquad (17.4)$$

where $\lambda(x) = k/(c_p\rho)$ is the thermal diffusivity and $f(x) = F(x)/(c_p\rho)$. The equation (17.4) is solved at the initial condition

$$T(x,0) = \varphi(x) \qquad (17.5)$$

and the boundary conditions formulated at the sector center

$$T(0,t) = T_{core} \qquad (17.6)$$

and at the outer boundary of the clothes

$$T(x_{outer},t) = T_{med} \qquad (17.7)$$

Lectures on computational fluid dynamics

Mathematical model of the ice protection
of a human body at high temperatures
of surrounding medium

The temperature of the surrounding medium was $T_{med} = 50^0$. It was assumed that the core center (at $x = 0$) temperature was constant in time $T_{core} = 36.7^0$.

The heat transfer process is subdivided into three steps. Within the first step the ice is warmed up to the melting temperature. The melting process is followed by the absorption of the heat coming from both the surrounding medium Q_{med}

$$\dot{Q}_{med} = \lambda_{med} \frac{\partial T}{\partial x} A_{med} \qquad (17.8)$$

and the human body Q_{hum} caused by metabolism

$$\dot{Q}_{hum} = \lambda_{skin} \frac{\partial T}{\partial x} A_{skin} \qquad (17.9)$$

where λ_{med} is the thermal diffusivity of the clothing layer adjacent to the ice layer, A_{med} is the surface between the ice layer and adjacent clothing layer in a sector under consideration, λ_{skin} is the thermal diffusivity of the human skin and A_{skin} is the skin surface in the sector. The second step is the ice layer melting. The phase transition in matter is described by the Stefan problem [40]. In this paper we used a simplified approach based on the heat balance conditions. It is assumed that the water and ice mixture is uniform with the constant temperature of zero degree of Celsius. The dynamics of the boundary between the water and ice is not considered. The heat fluxes (17.8) and (17.9) are constant in time. The second step is finished in time t^* once the ice is melted:

$$Q_{melt} = (\dot{Q}_{med} + \dot{Q}_{skin})t^* \qquad (17.10)$$

Here Q_{melt} is the heat necessary to melt the whole ice. After that, within the third step the water from the melted ice is warming up due to heat fluxes (17.8) and (17.9) continuing in time. The calculations within the third step are running as long as the comfort conditions are fulfilled.

The equation (17.4) is solved using the finite differential method on the uniform grid $\Delta x = const$ with the constant time step $\Delta t = const$. The numerical implementation utilizes the central differential scheme for space derivatives and Crank Nicolson implicit representation of the unsteady term. An inhouse code was developed for this purposes.

Lectures on computational fluid dynamics

Mathematical model of the ice protection
of a human body at high temperatures
of surrounding medium

17.5 Results

17.5.1 Design of the protection clothes

The calculations were performed for five elements of the human body shown in Fig.17.1. Thermodynamic properties of the body layers are given in the table 17.4. Usually, the ice protection construction consists of the ice layer separated from the surrounding medium by several layers. In the present work we used three layers: outer clothing layer with thickness of 0.001m, isolating layer of 0.009m and the air layer of 0.003m. All layers have the initial temperature $T_i^0 = 19^0$. The air gap between the ice and the underwear of the thickness 0.0025 m was 0.003 m thick. The human body was 180 cm in height with the mass of 80 kg. The full description of the input data can be found in [41]. It was assumed that the test person does the work at a rate of about $M = 420$ watts. Additional heat release due to this work was taken into account during numerical simulations in the heat production rate $f(x)$

(see Eq. (17.4)).

Lectures on computational fluid dynamics

Mathematical model of the ice protection
of a human body at high temperatures
of surrounding medium

Table 17.4: Thermodynamic coefficients of the body layers used in simulations

layer	heat capacity, KJ/K	thermal conductivity, W/(mK)	density kg m^{-3}	initial temperature, Deg. Celsius	heat production, W
core	39.97	0.4186	1050	36.89	76.24-80.00
muscles	74.68	0.3959	1050	36.28	8.30-9.00
fat	17.73	0.3348	850	34.53	3.57-4.00
skin	5.07	0.0807	1000	33.62	0.66-0.7

The numerical simulations are used to find the distribution of the ice thickness necessary to keep the body core (both inner an outer) temperature at less than $36.7^0 \pm 1^0$ within one hour at the temperature of surrounding medium of 50^0. The numerical results were utilized to design a special protection jacket for rescue team working under emergency conditions in the mining industry. Since the continuous distribution of the ice protection is difficult from the technology point of view and undesirable from ergonomics considerations the jacket protection was designed using the discrete distribution of the ice in form of briquettes embedded into the jacket (see Fig. 17.4). The further simulations have been performed to prove the ability of the new designed jacket to satisfy the protection requirements. Fig. 17.5 illustrates the temperature distribution around the human body in centers of the upper and the lower elliptical cylinders shown in Fig. 17.1. The discrepancy between the desirable temperature 36.7^0 corresponding to the continuous ice distribution and the actual temperature corresponding to the discrete ice distribution can be considered as acceptable. Therefore the jacket designed on the base of numerical simulations was manufactured and tested in further experimental investigations.

17.5.2   Experimental proof of numerical prediction

The numerical prediction and the jacket designed on basis of numerical simulations was proved in various tests. The first series of 48 measurements was carried out in a thermal chamber. The measurements were performed with healthy candidates at the age between 30 and 45 years, $P = 168 - 188$

Lectures on computational fluid dynamics

**Mathematical model of the ice protection
of a human body at high temperatures
of surrounding medium**
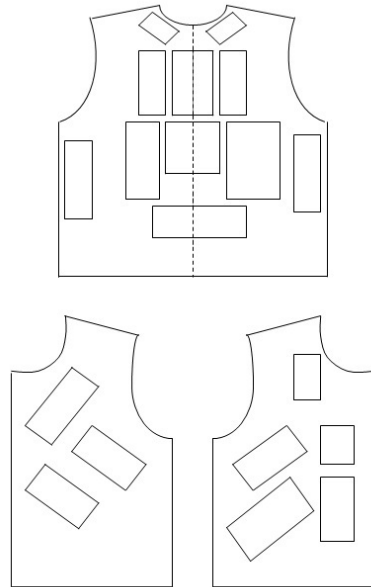
Figure 17.4: Overheating protection jacket designed on the base of simulations.
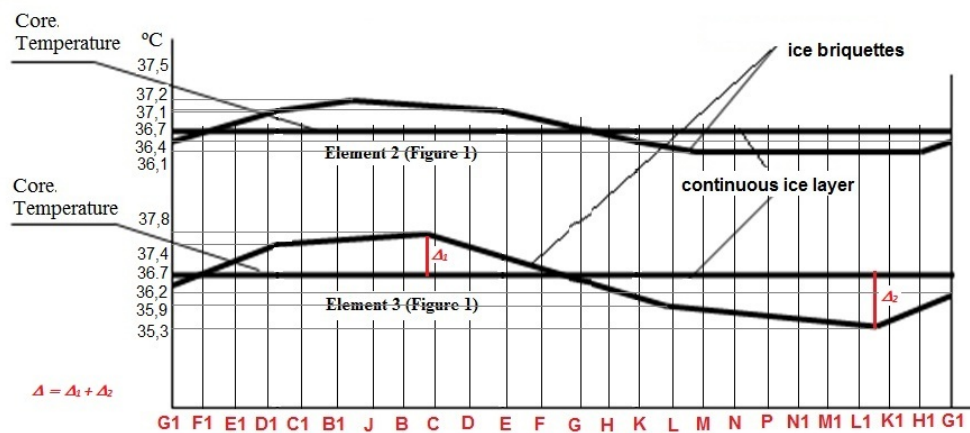
Figure 17.5: Temperature distributions around the body with continuous ice distribution and with ice briquettes. Results of numerical simulations after 60 minutes.

Lectures on computational fluid dynamics

Mathematical model of the ice protection
of a human body at high temperatures
of surrounding medium
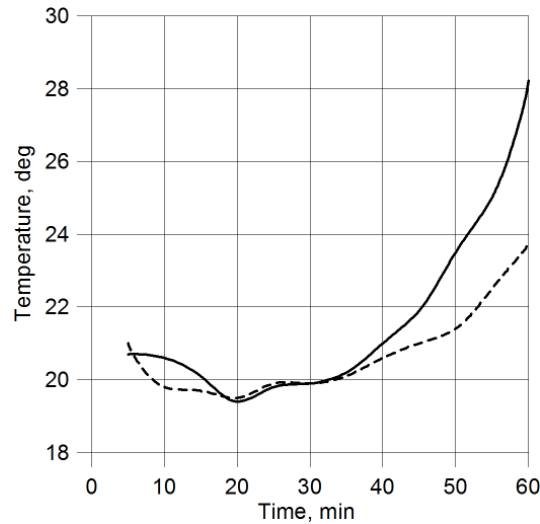
Figure 17.6: Development of the averaged temperature in the air gap between the underwear and the ice protection on the human chest. Comparison between the measurement (solid line) and the numerical simulations (dotted line).

Lectures on computational fluid dynamics

Mathematical model of the ice protection
of a human body at high temperatures
of surrounding medium

cm in height and normal weight m. The body surface A can be calculated from the empirical formula $A = 0.24m^{0.425}P^{0.4}$ [41]. The candidates weared the jackets (see Fig. 17.4)were doing the work at a rate of about $M = 420$ watts which corresponds to a hard work typical for the mining industry. The temperature of the surrounding medium was $T \approx 50^0$. The temperature has been measured in the air gap between the underwear and the ice at seven points around the chest (section 2 in Fig. 17.1). The temperature averaged over these points is presented in Fig. 17.6. The discrepancy between the measurement and the numerical simulations does not exceed 14 percent after 60 minutes of the real time. This agreement can be considered as quite satisfactory taking the simplicity of the used model and complexity of the problem into account.
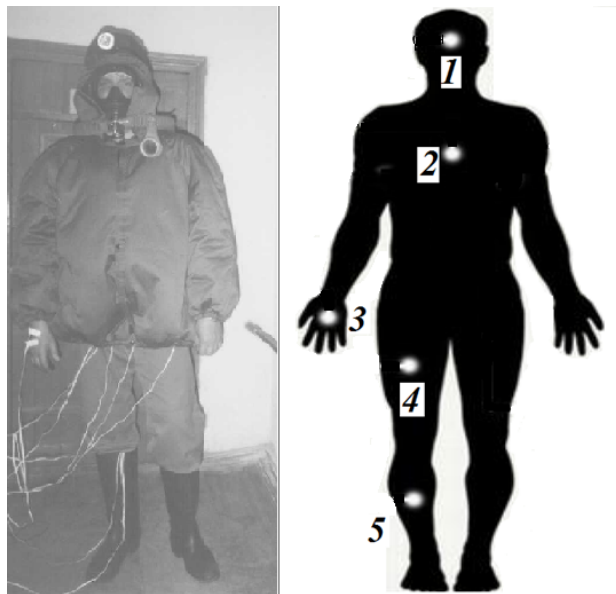

Figure 17.7: Test person weared overheating protection jacket (left) and distribution of the temperature sensors on the human body (right).

The task of this study is the determination of the temperature in the body core. It is a difficult problem since the direct measurement is impossible. The experience gathered in physiology [42] shows that the core temperature can reliably be determined if the temperature T_j at five characteristic points (forehead, chest, hand, thigh and shin) is known (see Fig.17.7). The sensors were mounted directly on the human skin with the rate of press not exceeding $0.2 - 0.25$ Pa. The accuracy of measurements is estimated as 0.1^0C. These temperatures are summed up with weighting coefficients w_j. Each temperature is nearly constant within a certain area A_j. The weighting coefficients are calculated as the ratio of A_j to the total body surface A, i.e. $w_j = A_j/S$. The averaged temperature is calculated then from the formula [41]

$$\overline{T} = 0.07T_1 + 0.5T_2 + 0.05T_3 + 0.18T_4 + 0.2T_5 \qquad (17.11)$$

Lectures on computational fluid dynamics

Mathematical model of the ice protection
of a human body at high temperatures
of surrounding medium

where T_j sensors readings according to the numeration shown in Fig. 17.7. The prediction accuracy can be sufficiently increased when the core temperature is calculated with account for the test person feeling and the rectal temperature T_{rectal} according to the formula [41]

$$T_{inner} = K T_{rectal} + (1 - K)\overline{T} \qquad (17.12)$$

The correlation factor K is taken from the table 17.5 [39]. Figure 17.8 shows the time history of the inner temperature T_{inner}. The most important conclusion drawn from this figure is that the inner temperature T_{inner} doesn't exceed the threshold 36^0 within 60 minutes. Thus, the aim of the design has been achieved.

Table 17.5: Coefficient K depending on the test person feelings and energy expenditure $E = M/A$ (W/m^2). A is the body surface (m^2) and M is the work (W)

feeling | E	70	88	113	145	178
cold	0.55	0.57	0.59	0.62	0.64
chilly	0.57	0.58	0.60	0.64	0.65
slightly chilly	0.59	0.60	0.63	0.65	0.67
comfort	0.62	0.64	0.65	0.67	0.69
slightly warm	0.70	0.70	0.70	0.70	0.70
warm	0.79	0.77	0.74	0.72	0.72
hot	0.86	0.82	0.79	0.76	0.73

The second series of measurements was carried out directly during the work in a cole mine at the temperature not higher than 60^0 without fire action. During one year of observations no equipment fault has been documented. The temperature of workers was kept at a prescribed level during at least $55 - 60$ minutes as predicted both in numerical simulations and thermal chamber tests.

17.6 Discussion

This chapter presents relatively simple and efficient model of the heat transfer within the human body at high temperatures of the surrounding medium. The human body cross section is represented as an ellipse with a few layers, modelling the internal organs. The heat generation by internal organs is taken into account. The ice protection and the clothes are modelled as additional layers covering the human body. Neglecting the heat transfer in vertical and circumferential directions the problem is reduced to the solution of the one dimensional heat conduction equation with variable heat diffusivity. The simulations were performed using the finite differential method. Results of simulation were used for calculation of the ice layer thickness necessary to prevent the body overheating and to keep the temperature of the

Lectures on computational fluid dynamics

Mathematical model of the ice protection
of a human body at high temperatures
of surrounding medium
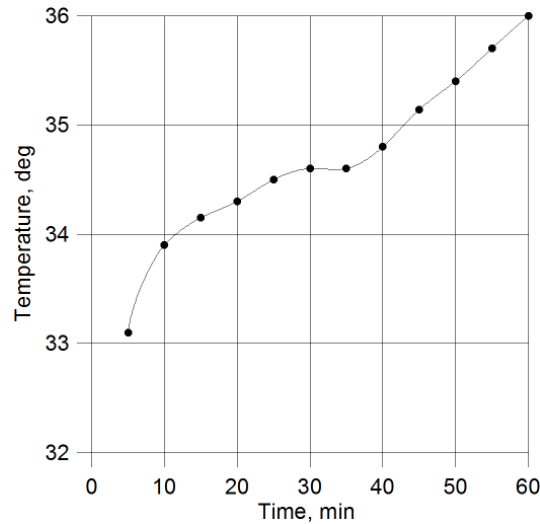
Figure 17.8: Inner human body temperature versus time.

body core at $36.7^0 \pm 1^0$ within one hour. The results of simulations were used for design of special overheating protection jacket. The labour tests of the jacket and trials at real conditions confirmed the prediction of the numerical simulations.

Chapter 18

CFD Design of cloth for protection of divers at low temperatures under current conditions

Study was performed for the model Tin Man presented in Fig. 18.1. Inner thermodynamics in the body was not modelled. The temperature of the human body was assumed to be constant and equal to 33^0 at the temperature of the surrounding medium of 10 degrees of Celsius. Thus, the Dirichlet boundary conditions were enforced for the temperature whereas the heat flux from the body was calculated. Heat exchange by shivering, breathing and radiation was neglected. The heat exchange between the body and surrounding medium is mostly determined by the convection due to wind. The incompressible flow was calculated using steady RANS (Reynolds Averaged Navier- Stokes Equations) using the $k - \omega$ SST model. Temperature was considered as a passive scalar determined from the temperature transport equation. The framework OpenFOAM was utilized for the numerical solution of this problem.

First, CFD was validated for the case of the air flow. Distribution of the heat transfer coefficient along the Tin Man body is shown in Fig. 18.1, left. The minimal heat flux takes place in the separation area with reduced flow velocities, i.e. behind the body arms and head, as well as in the stagnation area in the front part of the body. Figure 18.1 illustrates the integral coefficient of the heat transfer h_c obtained by integration over the whole body surface. Results of authors marked by crosses are compared with experimental data of de Dear et al. (triangles) and different calculations. Shadowed grey area shows the scattering of data otbained using various approaches. Big
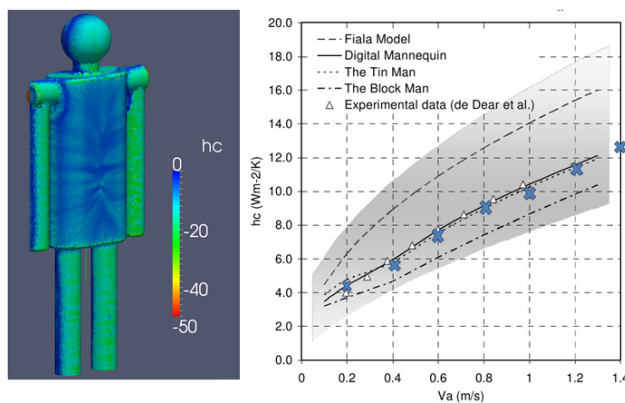
Figure 18.1: **Left:** Heat transfer coefficient at air speed of $1 m/s$. **Right:** Whole body convective heat transfer coefficient h_c from various published works. The figure is taken from [2]. Blue crosses show results of the present work.

scattering of data illustrates the complexity of the problem of the human body thermodynamics interaction with a surrounding medium. Our results agree satisfactory with measurements. Note that the calculations at small air speeds were performed assuming the laminar character of the flow.

Within the next step the Tin Man body was weared in a neoprene cloth with the thickness of $1.0 \; cm$ to reproduce the case of a diver working at low temperatures of 10^0 in a sea current with the speed of $1 \; m/s$. The Tin Man body temperature was uniformly distributed along the body and was 33 degrees of Celsius. The cloth was assumed to be waterproof and uniformly contaminated by oil products. This case is typical for ship repair works and rescue and technical operations in oil spill zones. Contamination in terms of gram per centimeter squared as well as the heat diffusivity coefficient of contaminated cloth are given in the table 18.1. The size of the computational domain was $12 \times 12 \times 6$ meters, whereas the size of the body was 1.65 meters. For discretization a mesh with 1.3 million of cells was used with y^+ values below 0.5 on the whole body. The results for heat flux depending on the contamination are presented in the last column of table 18.1 and in Fig. 18.2. As seen the heat flux is almost linear function of the contamination.

The Tin Man body is a primitive simplest geometry. From one side, it makes the solution of the inner thermodynamics problem much easier. From the other side, such simplified geometry is not suitable for aerodynamic calculations since it consists of sharp edges with numerous strong separations. Numerical solution becomes unstable leading to unsatisfactory convergence. Although the real human body is geometrically more complex, the flow around it can be calculated much easier than in the Tin Man case. Therefore, further investigations done by our group were performed for real human body geometry (Fig. 19.1) designed by the Hohenstein Institute [43] based on the detailed antropological study of different people categories.

Contamination g/cm^2	Heat diffusivity m^2/s	Heat flux $W/m^2 s$
0.0	$2.07 \cdot 10^{-6}$	1.89
0.5	$2.72 \cdot 10^{-6}$	2.41
2.5	$5.27 \cdot 10^{-6}$	4.46
4.5	$7.74 \cdot 10^{-6}$	6.33
6.5	$1.01 \cdot 10^{-5}$	8.08

Table 18.1: Heat flux from the diver depending on the cloth contamination
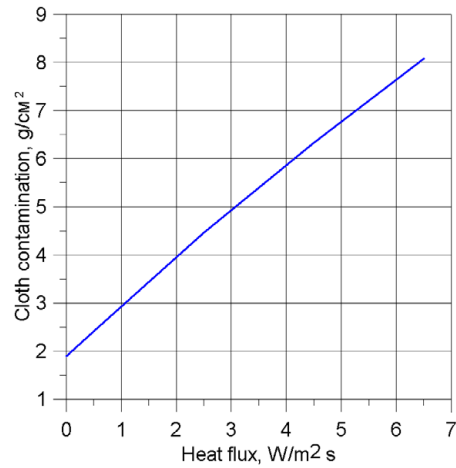
Figure 18.2: Heat flux from the
diver depending on the cloth con-
tamination

Lectures on computational fluid dynamics

CFD application for design of cloth for
protection from low temperatures under wind
conditions. Infl uence of the wind on the cloth
deformation and heat transfer from the body.

Chapter 19

CFD application for design of cloth for protection from low temperatures under wind conditions. Influence of the wind on the cloth deformation and heat transfer from the body.

Lebedeva and Brink [44] have shown the influence of wind on heat transfer due to cloth deformation caused by wind induced pressures. Experimental study was performed in open type wind tunnel with closed test section up to Reynolds number of $3.6 \cdot 10^5$ based on the air speed and diameter of cloth packages in form of cylinders. The aim of the present work is to get similar estimations for real human body form.

19.1   Wind tunnel measurements of pressure distribution

The experiment was conducted in the wind tunnel of the Chair of Ocean Engineering at the Rostock University. The wind tunnel of the Göttingen type has the test section of lengths of 2.8 m with the square cross section of 1.4×1.4 m^2. The model of the height of 700 mm was manufactured by
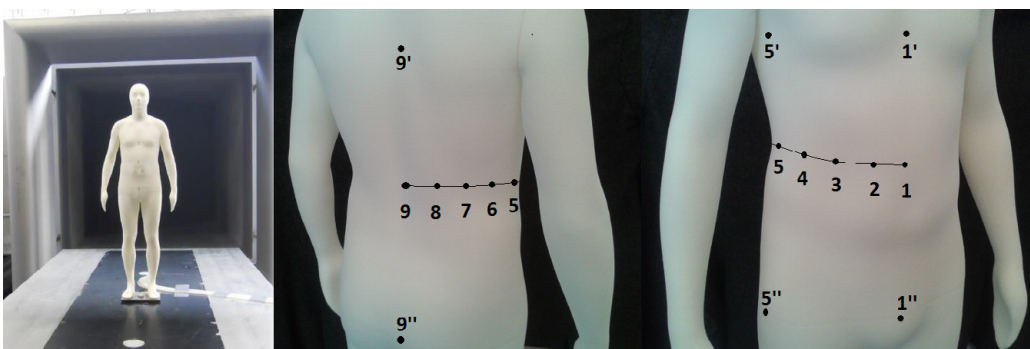
Figure 19.1: Human body model in wind tunnel of the Rostock university (left). Positions of measurement points (right).

Lectures on computational fluid dynamics

CFD application for design of cloth for protection from low temperatures under wind conditions. Infl uence of the wind on the cloth deformation and heat transfer from the body.

downsizing the real body with the scale factor of 0.39. Within the open test section the size of the air jet with uniform velocity distribution is estimated as one meter at least. Since it is one and half times as large as the model height, the influence of the jet boundaries on flow around the body can be considered as negligible. Two measurement series were performed. In the first one the pressure was measured at nine points distributed at three cross sections $z = 0.329, 0.418$ and 0.476 (see Fig. 19.1 and 19.3) using inclined manometers which are very accurate for low pressures measurements. Due to high inertia of inclined manometers the unsteady pressure oscillations are not captured. Position of measurement points is shown in Fig. 19.1 (points $1, 1', 1''$, $5, 5', 5''$ and $9, 9', 9''$). The measurements were performed with the air speed of $10 m/s$ at 14 degrees of Celsius. Reynolds number based on the maximum transversal body size is around $1.33 \cdot 10^5$. In the second series the measurements were performed at nine points $1, ..., 9$ shown in Fig. 19.3(right) only at $z = 0.418$ (waist). This more detailed investigation was carried out for two air speeds of 10 and 15 m/s.

19.2 Numerical simulations of pressure distribution and comparison with measurements

Numerical simulations were performed using the commercial software package STAR CCM+ for the air speed of 10 m/s. The boundary layer on the windward side is supposed to be in transitional state. Due to strong separation the flow on the leeward side of the model and in the wake can be considered as a turbulent one. The computational domain has the cross section of $2.1 \times 2.1 \ m^2$. A length of the domain is 2.1 m in front of the human body (0.7 m height) and 4.2 m behind it. The grid consists of $1.2 \cdot 10^6$ polyhedron cells with maximal y^+ value of 40. On the model sides the y^+ value is varied between 20 and 25. To exclude ambiguity connected to the flow character, simulations were performed both for pure turbulent and pure laminar flows with and without roughness.

19.3 Comparison of CFD results with measurements

Comparison with measurements for the first series is presented in Fig. 19.2. The results of measurements and simulations agree well in the front part of the body and in the separation area. Both simulations and measurements predict the increase of the pressure coefficient in the section $z = 0.476$ m at angle ≈ 90 degrees caused by the stagnation effect of the shoulder. On the side of the model in cross sections $z = 0.329$ and 0.418 the agreement is not satisfactory. To clarify this problem, the more detailed second measurement series was performed. All results obtained at $z = 0.418$ are presented in Fig. 19.3. The big difference takes place around the angle of approx. 90 degrees in the area of the separation (point 5 in Fig. 19.1). The experiment doesn't predict the strong under pressure region on the side of the model. The minimum experimental pressure coefficient is around -1 whereas the simulation predicts -2.2 both for laminar and turbulent cases. The difference between the laminar and turbulent solutions is negligible. This might be due to two facts. First, the cross section is elliptical (Fig. 19.2, left) and the averaged position of flow separation points is fixed at the widest axis and doesn't depend on the flow character. Second, strong unsteady flow oscillation makes the difference between laminar and turbulent pressure distributions negligible.

Lectures on computational fluid dynamics

CFD application for design of cloth for protection from low temperatures under wind conditions. Infl uence of the wind on the cloth deformation and heat transfer from the body.

The experimental results raised many questions. Without big error, the flow can be considered as quasi two dimensional in cross sections along the human body. Then C_{pmin} is minus three for the case of two dimensional cylinder flow. Due to three dimensional effects C_{pmin} can be smaller, but not three times smaller like in measurements. The numerical simulation reveals no separation up to angle of 90 degrees. Within the separation zone at angles larger than 120 degrees the numerical pressure coefficient is nearly constant. These facts are in a good agreement with classic knowledge about bluff bodies flows. In experiment, C_p slightly increases in the separation area at angles larger than 90 degrees. Also, a relatively big discrepancy
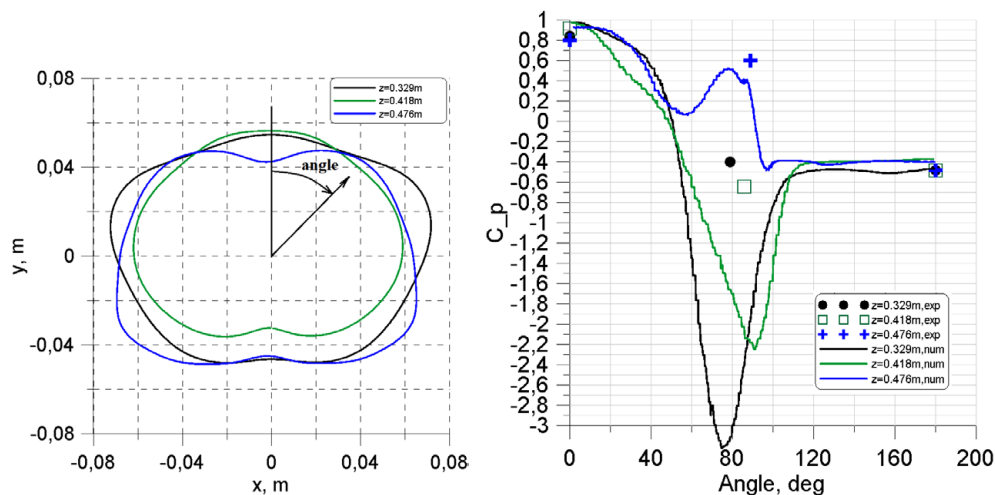
Figure 19.2: Contrours of torso (left) and pressure coefficient C_p distribution around the body at three different altitudes $z = 0.329, 0.418$ and 0.476m.

between C_p determined for 10 and 15 m/s seems to be very questionable, at least within the zone of weak Reynolds number influence, i.e. at angles less than 90 degrees. The flow at angles larger than 90 degrees is unsteady. The scattering of the data due to unsteady effects is shown both for simulations and measurement. Obviously, the unsteady pressure oscillations can not be reason for the disagreement between simulation and experiments. More detailed experimental study should be carried out in the future to clear this problem.

19.4 Change of thermal conductivity caused by wind induced pressures

Estimations of pressure influence on cloth thermal conductivity was performed experimentally in the Thermal laboratory of the Don State Technical University. The cloth of 30 mm thickness was manufactured from the Saviour with Flamestat Cotton (upper sheet), the insulation Thinsulate and Taffeta as a lining. The cloth is used in oil industry for work at very low temperatures under oil contamination conditions.

Lectures on computational fluid dynamics

CFD application for design of cloth for protection from low temperatures under wind conditions. Infl uence of the wind on the cloth deformation and heat transfer from the body.

It was assumed that the pressure acts only in normal direction and shear stresses are neglected. The cloth has such a structure that it can be pressed but not stretched. With the other words, the cloth has no deformation if the pressure difference $\Delta p = p - p_{atm}$ is negative. Bearing this in mind, the cloth deformation calculated using numerical pressure data can be considered
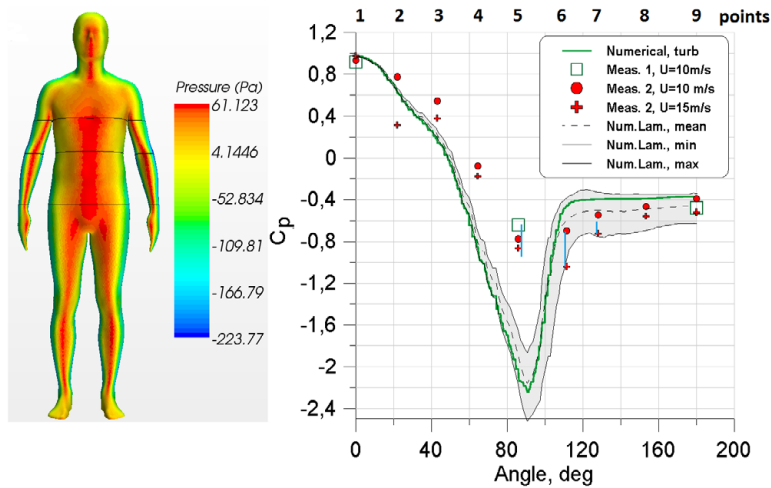
Figure 19.3: **Left:** Pressure distribution Δp on the body obtained using StarCCM+ commercial software. Contours of three cross sections at $z = 0.329, 0.418$ and 0.476 m are marked by black lines. **Right:** Pressure coefficient C_p distribution around the body at $z = 0.418$. Points position $1, .., 9$ is shown in Fig. 19.1. Grey zone is the area of unsteady pressure coefficient oscillations in the laminar solution. Vertical lines indicate the scattering of experimental data at points 5, 6 and 7.

as reliable one since the area of positive C_p is approximately the same in experiments and simulations. The cloth samples were subjected to pressure and then the thermal conductivity was measured using steady state method. Approximation of measurement points results in the following interpolation formula:

$$k = 0.22 + c_1 \Delta p + c_2 \Delta p^2 \qquad (19.1)$$

where k is the thermal conductivity coefficient in W/mK, $C_1 = 9.322 \cdot 10^{-4} \frac{W}{mKPa}$ and $C_2 = 9.775 \cdot 10^{-6} \frac{W}{mKPa^2}$. Fig. 19.4 shows distribution of the thermal conductivity around the body at three sections along the human body. As seen the conductivity can increase in the stagnation area at the chest up to four and half times for strong wind of 20 m/s. To estimate the integral wind influence f the thermal conductivity referred to that without wind was integrated over the body at five sections:

$$f(z) = \oint k(wind \neq 0)/k(wind = 0)r \ d\vartheta \qquad (19.2)$$

Lectures on computational fluid dynamics

CFD application for design of cloth for protection from low temperatures under wind conditions. Infl uence of the wind on the cloth deformation and heat transfer from the body.

where ϑ and r are zylindrical coordinates in a cross section. The results are summarized in the table 19.1. At strong wind of 20 m/s or 72 km/h the integral increase of thermal conductivity can be up to seventy percent in the chest cross section. At moderate wind of 10 m/s the maximum influence is less than ten percent.

Table 19.1: Thermal conductivity factor $f(z)$ integrated in circumferential direction

Body part	Wind 10 m/s	20 m/s
Chest ($z = 0.476$ m)	1.096	1.729
Waist ($z = 0.418$ m)	1.025	1.199
Hip ($z = 0.329$ m)	1.085	1.668
Upper leg ($z = 0.25$ m)	1.025	1.194
Lower leg ($z = 0.12$ m)	1.018	1.141
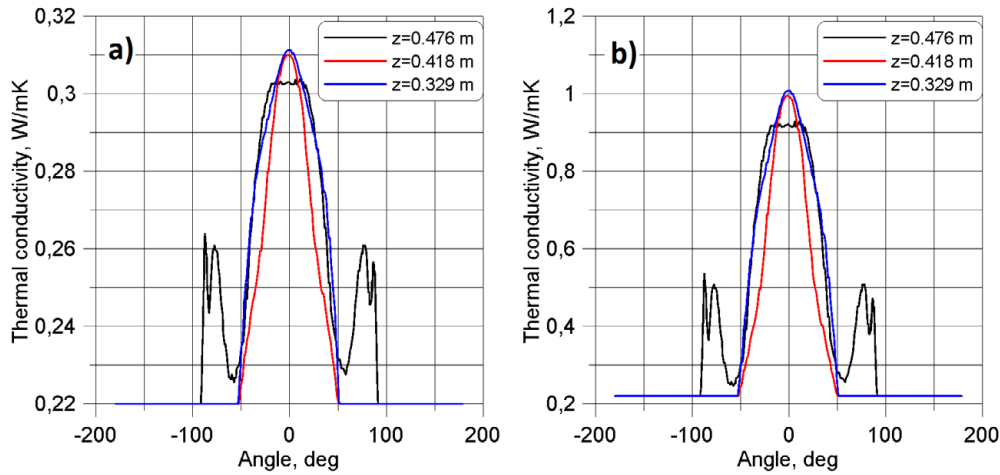
Figure 19.4: Change of thermal conductivity due to pressure induced by wind of 10 m/s (left) and 20 m/s (right). Thermal conductivity without wind is 0.22 W/mK.

Chapter 20

Simulation of human comfort conditions in car cabins

The comfort conditions of drivers and passengers is one of the most important research topics in car industry. In this chapter we present a fragment of the research conducted in this field at the chair of modelling and simulation of the University of Rostock. The calculations presented below were carried out by Stefan Knochenhauer. A compact car was chosen as the object of investigations. The cabin geometry is represented in Fig. 20.1. The inlet of the air stream coming from the ventilation channel is marked by green color whereas the air outlet by red one. The grid with 6.5 million of cells is shown in Fig. 20.2. The mathematical model is based on the URANS equation (12.17) and temperature transport equation (1.30). The turbulent character of the temperature transport is taken into account by introduction of the additional turbulent heat conduction. It means that instead of λ in the equation (1.30) we use the sum $\lambda + \lambda_t$, where λ_t is the turbulent heat conduction coefficient. λ_t is expressed through the turbulent kinematic viscosity ν_t and the turbulent Prandtl number Pr_t
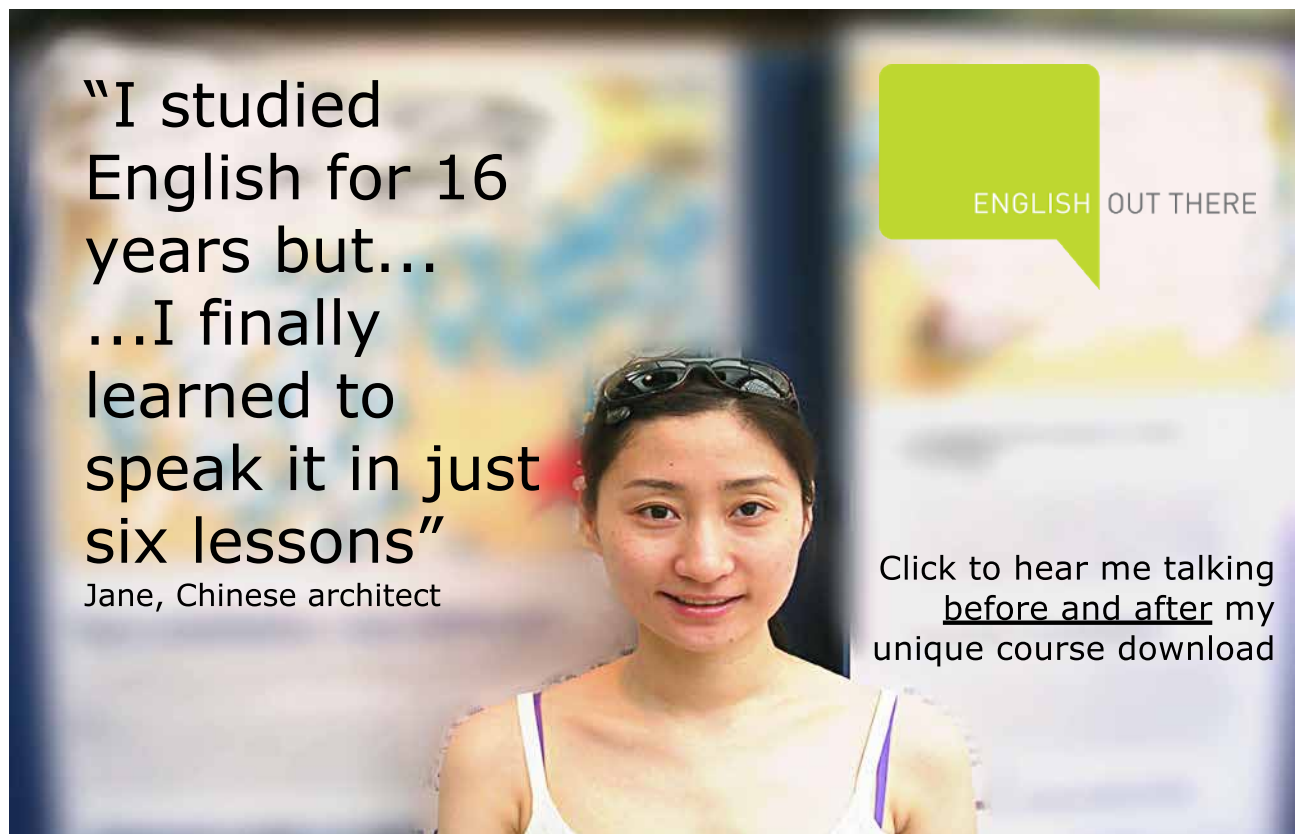
$$\frac{\lambda_t}{\rho c_p} = \frac{\nu_t}{Pr_t} \tag{20.1}$$

The turbulent kinematic viscosity is computed from the URANS closure models (see Chapters 12, 13 and 14) whereas the turbulent Prandtl number is assumed to be constant $Pr_t \approx 0.7$. The URANS closure model used in this work is the $k - \omega$ SST model [45]. Numerical simulations were performed using the finite volume method (see Chapter 6). Boundary conditions are given in the table 20.1.

A few selected results of calculations are illustrated in Fig. 20.3. The distributions of air velocity and temperature inside of the car cabin are strongly inhomogeneous. In regions of strong velocity the convective heat transfer dominates whereas in stagnation areas the heat exchange is mostly due to the heat conduction.
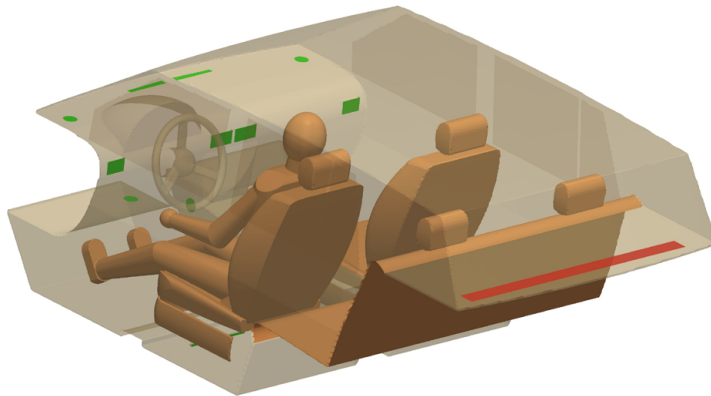
Figure 20.1: Sketch of the car cabin studied numerically.
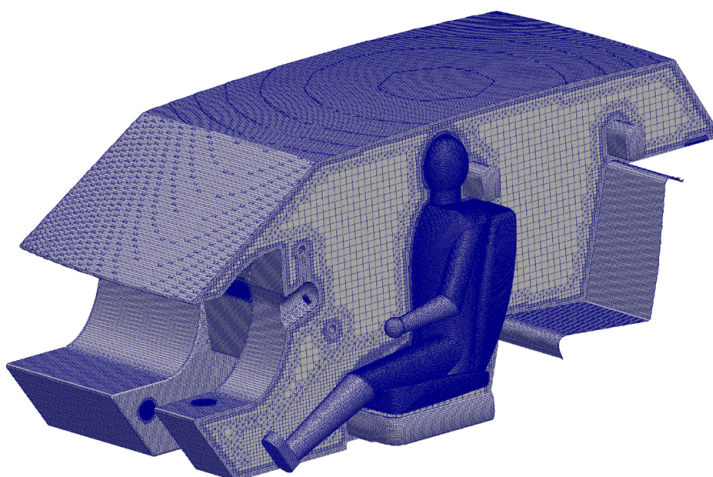
Figure 20.2: Grids with 6.5 million of cells generated with snappyHexMesh.

Surface	physical quantity	Condition
Inlet	Velocity	$\left(u_x \; u_y \; u_z\right)$
	Pressure	$grad \; \overline{p} = 0$
	Temperature	$T = konst.$
	turbulent kinetic energy	$k = konst.$
	specific turbulent dissipation rate	$\omega = konst.$
Outlet	Velocity	$grad \; \overline{U} = 0$
	Pressure	$\overline{p} = 0$
	Temperature	$grad \; T = 0$
	turbulent kinetic energy	$grad \; k = 0$
	specific turbulent dissipation rate	$grad \; \omega = 0$
Other surfaces	Velocity	$\overline{U} = 0$
	Pressure	$grad \; \overline{p} = 0$
	Temperature	$T = konst.$ or $grad \; T = 0$ or coupled boundary condition
	turbulent kinetic energy	modelled by wall function
	specific turbulent dissipation rate	modelled by wall function

Table 20.1: Boundary conditions

(a) Velocity field   (b) Temperature field
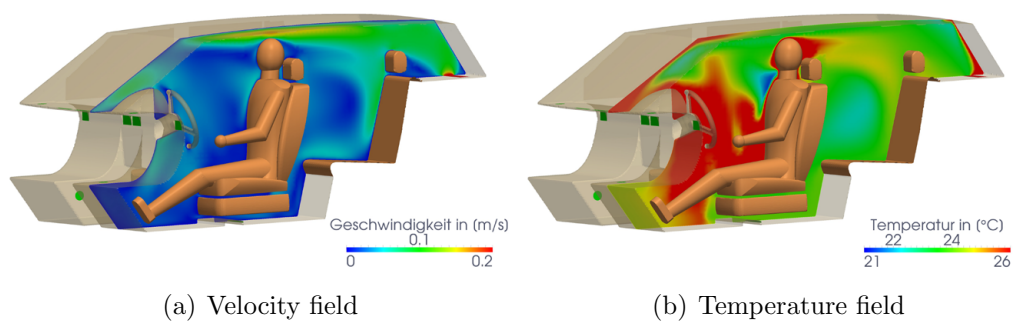
Figure 20.3: Results of numerical simulations.

Bibliography

[1] Tsinober A. An informal introduction to turbulence. *Kluwer Academic Publisher*, 2004.

[2] Novieto D. Zhang Y. and Yingchun J. Human envoronmental heat transfer simulation with cfd- the advances and challenges.*building simulation 2009*. pages 2162–2168. Eleventh International IBPSA Conference, Glasgow, Scotland, July 27–30, 2009 2009.

[3] Ferziger J. and Peric M. *Computational Methods for Fluid Dynamics.* Springer, 2002.

[4] Seibold B. A compact and fast matlab code solving the incompressible navier-stokes equations on rectangular domains. *Applied Mathematics, Massachusetts Institute of Technology, www-math.mit.edu/ seibold*, 2008.

[5] Dornseifer T. Griebel M. and Neunhoeffer T. Numerical simulation in fluid dynamics: A practical introduction. *Society for Industrial and Applied Mathematics, Philadelphia, PA, USA*, 1998.

[6] Phillips A.B. Turnock S.R. and Furlong M. Urans simulations of static drift and dynamic manouveres of the KVLCC2 tanker. pages F63–F68. Proceedings of the SIMMAN workshop, 2008.

[7] Liseikin V. *Grid Generation Methods.* Springer, 2010. 390p.

[8] Warsi Z.U.A Thompson I.F. and Mastin C.W. Numerical grid generation. *Foundations and applications*, 1997.

[9] Novikov E. Generalized dynamics of three-dimensional singularities (vortons). *Sov. JETP*, 84(3):975 – 981, 1984.

[10] Chorin A. The evolution of a turbulent vortex. *Comm. in Mathematical Physics*, 83:517 – 535, 1982.

[11] Chorin A. Constrained random walks and vortex filaments in turbulence theory. *Comm. in Mathematical Physics*, 132:519 – 536, 1990.

[12] Schlichting H. *Boundary layer theory.* Springer, 2000.

[13] Batchelor G. *The Theory of Homogeneous Turbulence.* Cambridge University Press, Cambridge, 1956.

[14] Pope S. *Turbulent flows.* Cambridge University Press, Cambridge, 2000.

[15] Below I.A. and Isaev S.A. *Modelling of turbulent flows.* Saint Petersburg, (2001).

[16] Ferziger H. Bardina J. and Reynolds W. Improved subgrid models for large eddy simulation. *AIAA Paper*, pages 80 – 1357, 1980.

[17] Peng S. Hybrid rans-les modeling based on zero- and one- equation models for turbulent flow simulation. pages 1159 – 1164. Proc. of 4th Int. Symp. Turb. and Shear Flow Phenomena, 2005.

[18] Davidson L. and Dalstroem S. Hybrid rans-les: An approach to make les applicable at high reynolds number. *Int. J. of Comp. Fluid Dynamics*, 19:415 – 427, 2005.

[19] Terracol M. Airframe noise prediction by mean of a zonal rans/les approach. pages 1165 – 1169. In: Proc. of 4th Int. Symp. Turb. and Shear Flow Phenomena, 2005.

[20] Kniesner B. Kadavelil G. Basara B. Jakirlic S., Saric S. and Chaouat B. Sgs modelling in les of wall-bounded flows using transport rans models: from a zonal to a seamless hybrid les/rans method. pages 1057 – 1062. Proc. of 6th Int. Symp. Turb. and Shear Flow Phenomena, 2007.

[21] Leschziner M. Temmerman L., Hadziabdec M. and Hanjalic K. A hybrid two-layer urans-les approach for large-eddy simulation at high reynolds numbers. *Int. J. of Heat and Fluid*, 26:173 – 190, 2005.

[22] Strelets M. Spalart P. R., Jou W. H. and Allmaras S. R. Comments on the feasibility of les for wings and on a hybrid rans/les approach. pages 137 – 148. Advances in LES/DNS: Proc. of the first AFOSR International Conf. on DNS/LES, 1997.

[23] Spalart P.R. Detached-eddy simulation. *Annu. Rev. Fluid Mech.*, 41:181 – 202, 2009.

[24] Menter F. and Egorov J. Turbulence models based on the length-scale equation. pages 941 – 946. Proc. of 4th Int. Symp. Turb. and Shear Flow Phenomena, 2005.

[25] Davidson L. and Billson M. Hybrid les-rans using synthesized turbulent fluctuations for forcing in the interface region. *Int. J. of Heat and Fluid*, 27:1028 – 1042, 2006.

[26] Abe K. and Miyata Y. An investigation of hybrid les/rans models for predicting flow fields with separation. pages 1153 – 1158. Proc. of 4th Int. Symp. Turb. and Shear Flow Phenomena, 2005.

[27] Pitsch H. Schlueter J. U. and Moin P. onsistent boundary conditions for integrated les/rans simulations: Les outflow conditions. volume 3121, pages 1 – 8. AIAA, 2002.

[28] Ducros F. Benerafa Y. and Sagaut P. Rans/les coupling using a forcing term approach. pages 1141 – 1146. 4th Int. Symp. Turb. and Shear Flow Phenomena, 2005.

[29] Kornev N., Taranov A., Shchukin E., and Kleinsorge L. Development of hybrid urans-les methods for flow simulations in the ship area. *Ocean Engineering*, 38(16):1831–1838, 20111.

[30] Durbin P. Near-wall turbulence closure modeling without damping functions. *J. Theor. Comput. Fluid Dyn*, 1991.

[31] Werner H. and Wengle H. Large-eddy simulation of turbulent flow over and around a cube in a plate channel. 8th Symposium on Turbulent Shear Flows, 1991.

[32] Fureby C. Huuva T. Alin N., Bensow R. and Svennberg U. Current capabilities of des and les for submarines at straight course. *J. Ship Research*, 54:184 –196, 2010.

[33] Guminer P.K. Thermoregulation studying in hygiene and work physiology. *Medgiz, Moscow*, page 147, 1962.

[34] Novieto D. Zhang Y. and Yingchun J. Human environmental heat transfer simulation with cfd the advances and challenges. pages 2162 – 2168. Eleventh International IBPSA Conference, Glasgow, Scotland, 2009.

[35] Cherunova I.V. New technologies of heat protection wear design, (in russian). *Technologies of textile industry*, pages 51 – 54, 2009.

[36] Palella B.I. Alfano1 F. R. and G. Riccio. Thermode 193: an enhanced stolwijk thermoregulation model of the human body. page 8. 7th International Thermal Manikin and Modelling Meeting, University of Coimbra, 2008.

[37] Smith T. Anatomie-atlas: Aufbau und Funktionsweise des menschlichen Körpers. *Dorling Kindersley, Deutschland*, page 448, 2011.

[38] Herman I.P. *Physics of a human body.* Springer, 860p., 2007.

[39] Zhavoronkov A. Grivina I. and Postnikov N. Pecularities of developments of imitation model "human-clothes-medium" (in russian) textile industry. 3:36 – 37, 1988.

[40] Alexiades V. and Solomon A.D. Mathematical modeling of melting and freezing processes: Basic concepts & applications. *Taylor & Francis*, 1992.

[41] Cherunova I. *Theoretical foundations of complex design of special clothes for protection at high temperatures conditions.* PhD thesis, South Russian University of Economics and Service, Shakhty, 2008.

[42] Vitte N.K. Thermal exchange and its hygienic value. *State medical publishing, Kiev*, page 145, 1956.

[43] www.hohenstein.de.

[44] Brink I. and Lebedeva E. Investigation of wind influence on packages of heat protecting cloth. *Textile Industry*, 3:34–36 (in Russian), 2005.

[45] Menter F.R. Zonal two equation k-ω turbulence models for aerodynamic flows. AIAA 93-2906, 24th Fluid Dynamics Conference, Orlando, Florida, 1993.

[46] Ginevsky A.S., Vlasov Ye.V., Karavosov R.K., 2004, Acoustic control of turbulent jets, Springer, 232 p.

[47] Kornev N., Zhdanov V. and Hassel E. (2008) Study of scalar macro- and microstructures in a confined jet, Int. Journal Heat and Fluid Flow, vol. 29/3, 665–674.

[48] Frick P., Turbulence, Models and Methods, Lecture course, Perm State University, Vol.~2, pp.~138, 1999.

Index